Contributions to Mineralogy and Petrology (2023) 178:51
https://doi.org/10.1007/s00410-023-02035-7

ORIGINAL PAPER

Ascent-driven differentiation: a mechanism to keep arc magmas metaluminous?

Felix Marxer[1,2] · **Peter Ulmer**[2] · **Othmar Müntener**[3]

Received: 10 February 2023 / Accepted: 13 July 2023 / Published online: 28 July 2023

Abstract

Arc magmatism is fundamental to the generation of new continental or island arc crust. However, the mechanisms that add to the chemical complexity of natural calc-alkaline magmas ranging from basaltic to rhyolitic compositions are debated. Differentiation mechanisms currently discussed include magma mixing, assimilation, crustal melting, or (fractional) crystallisation. In this contribution, the differentiation of arc magmas by decompression-driven crystallisation is investigated. We performed a set of equilibrium crystallisation experiments at variable crustal pressures (200–800 MPa) on a hydrous high-Al basalt (3.5 wt.% of H_2O in the starting material) with run temperatures varying from near-liquidus conditions (1110 °C) to 900 °C. Oxygen fugacity was buffered at moderately oxidising conditions close to the NNO equilibrium. Combining these novel experiments with previous polybaric fractional crystallisation experiments (Marxer et al., Contrib Mineral Petrol 177:3, 2022) we demonstrate the effects of pressure on the crystallisation behaviour of calc-alkaline magmas with respect to liquid and cumulate lines of descent, mineral chemistry, and phase proportions. Decompression shifts the olivine-clinopyroxene cotectic curve towards melt compositions with higher normative clinopyroxene and enlarges the stability field of plagioclase. This exerts a key control on the alumina saturation index of residual liquids. We argue that near-adiabatic (or near-isothermal) decompression accompanied by dissolution of clinopyroxene entrained during residual melt extraction in the lower crust keeps arc magmas metaluminous during crystallisation-driven differentiation thereby closely reproducing the compositional spread observed for natural arc rocks.

Keywords Arc magmatism · Arc magma differentiation · Ascent-driven differentiation · Crystal entrainment · Clinopyroxene dissolution · Isothermal decompression · ASI evolution · Equilibrium crystallisation · Magmatic phase equilibria · Calc-alkaline rocks

Introduction

Arc magmatism represents the dominant igneous activity at active convergent plate margins (i.e. subduction zones) and is, thus, strongly related to the generation of new continental and island arc crust. However, there is an ongoing debate how arc magmas acquire their specific compositional characteristics (e.g. low FeO/MgO, high H_2O, high SiO_2). A pertinent issue is the alumina saturation index (or ASI = Al_2O_3/($CaO + Na_2O + K_2O$), molar ratio) describing the "saturation level" of a rock in alumina. Rocks (or magmas) with an ASI < 1.0 are classified as metaluminous (= alumina undersaturated, clinopyroxene-normative), while an ASI exceeding 1.0 corresponds to peraluminous compositions (= alumina oversaturated, corundum-normative).

Generally, arc plutonic and volcanic rocks exhibit a smooth increase of ASI with progressive differentiation, with most intermediate compositions (SiO_2 of 55–65 wt.%) being metaluminous (e.g. Blatter et al. 2013; Turner and Langmuir 2015). However, experimental data on arc magma differentiation via equilibrium or fractional crystallisation show a distinctively higher variability, where high-pressure (700–1000 MPa) liquid lines of descent (e.g. Müntener et al.

Communicated by Dante Canil.

✉ Felix Marxer
f.marxer@mineralogie.uni-hannover.de

[1] Institute of Mineralogy, Leibniz University Hannover, Callinstraße 3, 30167 Hannover, Germany

[2] Institute of Geochemistry and Petrology, ETH Zürich, Clausiusstrasse 25, 8092 Zurich, Switzerland

[3] Institute of Earth Sciences (ISTE), University of Lausanne, Bâtiment Géopolis, 1015 Lausanne, Switzerland

2001; Blatter et al. 2013; Nandedkar et al. 2014; Melekhova et al. 2015; Ulmer et al. 2018) reveal a pronounced and rapid evolution towards peraluminous compositions while low-pressure (200–400 MPa) differentiation trends (e.g. Sisson and Grove 1993; Blatter et al. 2013) enter the peraluminous compositional field at more evolved compositions, similar to the natural rock record. Low-pressure crystallisation has therefore been favoured as the dominant arc magma differentiation mechanism (e.g. Sisson and Grove 1993; Blundy and Cashman 2008). These experimental constraints contrast with field observations of exposed paleo-oceanic island and continental arc crustal sections such as the Kohistan arc in Pakistan (Bard 1983; Jagoutz 2014), the Talkeetna arc in Alaska (Greene et al. 2006; Bucholz and Kelemen 2019), or the Famatinian arc in Argentina (Ducea et al. 2015; Walker et al. 2015; Rapela et al. 2018), where mafic to ultramafic cumulate rocks (the "residues" of crystallisation-driven magma differentiation) are predominantly observed in the lower crust and almost absent at upper-crustal levels. In addition, a significant amount of arc rocks exhibits geochemical evidence (e.g. REE patterns) for high-pressure, amphibole-dominated fractionation (e.g. Romick et al. 1992; Davidson et al. 2007; Larocque and Canil 2010). Consequently, field data rather favours the scenario of dominant high-pressure differentiation of arc magma in the lower crust followed by minor further compositional modification at shallow levels.

However, to solve this apparent discrepancy between natural observations and experimental data (sometimes described as "ASI paradox") several additional magmatic processes have been proposed, such as (1) mixing of magmas of contrasting compositions (e.g. basaltic and rhyolitic) (e.g. Sakuyama 1981; Hildreth and Moorbath 1988; Reubi and Blundy 2009; Blatter et al. 2013; Laumonier et al. 2014; Reubi and Müntener 2022), (2) mixing of magmas with differing water contents (e.g. "dry" and "wet" basalts) (Rezeau et al. 2021), or (3) polybaric differentiation (e.g. Melekhova et al. 2015; Lewis et al. 2021; Marxer et al. 2022). In scenario (1), mixing between mantle-derived basaltic liquids and more evolved silica-enriched melts (generated either by fractional crystallisation of the former or partial melting of pre-existing lower-crustal lithologies) leads to the formation of intermediate products of metaluminous composition. Mixing chords exhibit a smoother evolution in ASI vs SiO_2 than high-pressure crystallisation-driven liquid lines of descent (LLD), as shown in detail by Blatter et al. (2013). Nevertheless, the high viscosity contrast between basaltic and felsic melts makes magma mixing mechanically challenging and one would rather expect magma mingling instead; preventing the generation of a hybrid liquid of a homogeneous chemical composition (Sparks and Marshall 1986; Laumonier et al. 2014). Furthermore, a hybrid magma generated at lower crustal conditions would tend to evolve back on the high-pressure LLD resulting in the formation of additional cumulates and potentially significant cooling of the magma limiting the probability of melt extraction and upper crustal emplacement (Bowen 1928). During process (2), basalts of variable H_2O contents are believed to mix in the lower crust resulting in a "damp" hybrid melt (< 2 wt.% of H_2O). During subsequent cooling of such relatively low-H_2O magmas, early saturation of plagioclase inhibits a strong increase of ASI upon further differentiation (Melekhova et al. 2015; Rezeau et al. 2021). However, this hypothesis disagrees with recent studies suggesting that primitive arc basalts generally contain significant amounts of water (>> 2 wt.%) (e.g. Carmichael 2002; Goltz et al. 2020; Müntener et al. 2021; Urann et al. 2022) and geochemical evidence (e.g. REE proxies, lack of Eu-anomalies, high Sr/Y ratios) for the prominent role of amphibole and delayed plagioclase saturation in arc magmas (e.g. Macpherson et al. 2006; Davidson et al. 2007; Dessimoz et al. 2012). Furthermore, dry (or damp) crystallisation of basalts would result in arc tholeiitic differentiation trajectories (enrichment in FeO over MgO at almost constant SiO_2 (e.g. Villiger et al. 2004; Melekhova et al. 2015; Ulmer et al. 2018)), inconsistent with the compositional trends of natural arc rocks (e.g. Miyashiro 1974). Lastly, scenario (3) implies that crystallisation-driven differentiation of arc magmas occurs along a trans-crustal magmatic system where cumulate rocks are distributed over the entire crustal column (e.g. Lewis et al. 2021; Marxer et al. 2022). Progressive decompression during crystallisation affects phase equilibria, especially the olivine-clinopyroxene cotectic curve, but also plagioclase stability, inhibiting a distinct evolution towards peraluminous compositions of the residual liquids upon differentiation (e.g. Grove and Baker 1984; Grove et al. 1992; Sisson and Grove 1993). Polybaric fractionation has recently been investigated experimentally by Marxer et al. (2022). Their data revealed that fractionation along decompression-dominated magma ascent trajectories (20–25 °C/100 MPa) under oxidising conditions (NNO + 1 to NNO + 2) keeps residual liquids metaluminous upon differentiation. However, their experiments could not reproduce the entire compositional spread observed for natural arc rock compilations putting an upper limit on the effect of pure decompression-driven fractionation on arc magmatic LLDs. Therefore, Marxer et al. (2022) suggested the concept of imperfect fractionation, i.e. crystal cargo entrainment during residual melt extraction in the lower crust and subsequent dissolution of clinopyroxene upon magma ascent altering the composition of residual liquids considerably via shifting them to lower ASIs (i.e. more metaluminous compositions).

All processes described above play important roles in the evolution of arc magmas, but in this study, we explore the effect of decompression on arc magmatic phase equilibria and liquid lines of descent via conducting equilibrium crystallisation experiments at pressures ranging from 200

to 800 MPa on a high-alumina basalt. One major advantage of the dataset presented in this contribution over previous similar experimental studies (e.g. Blatter et al. 2013; Melekhova et al. 2015) is that the entire crustal column is covered in terms of pressures (200–800 MPa vs 400–900 or 400–1300 MPa), i.e. including the final emplacement and differentiation conditions of arc magmas in the upper crust. In contrast to the polybaric fractional crystallisation experiments of Marxer et al. (2022), where only a few P–T ascent trajectories were explored, the equilibrium crystallisation experiments presented herein allow to quantify and isolate the effect of pressure on phase equilibria in a closed magmatic system to refine the clinopyroxene dissolution hypothesis of Marxer et al. (2022). In addition, comparing our equilibrium crystallisation results with the polybaric fractional crystallisation runs of Marxer et al. (2022) enables an investigation of the impact of different crystallisation regimes (i.e. equilibrium vs fractional crystallisation) on arc magmatic liquid lines of descent in a polybaric differentiation scenario. Finally, combining our findings with previous experimental results on the crystallisation of hydrous basalts (Alonso-Perez 2006; Blatter et al. 2013; Nandedkar et al. 2014; Ulmer et al. 2018; Marxer et al. 2022) we formulate a modified crystallisation-driven arc magma differentiation model emphasising decompression-controlled processes.

Methods

Starting material and capsule preparation

Equilibrium crystallisation experiments were conducted on a high-alumina basalt with 3.5 wt.% H_2O corresponding to the initial starting material (rk54) used for the polybaric fractional crystallisation study by Marxer et al. (2022). This composition represents a derivative liquid from the fractional crystallisation experimental study of Ulmer et al. (2018) on a primary high-Mg basalt from the Adamello Batholith (Northern Italy) at 1.0 GPa and is reported in Table 1 and the Electronic Supplementary Material ESM1. This basalt has an arc-tholeiitic affinity with relatively low Na_2O and comparatively high K_2O contents, but its composition is within the range of average primitive arc magmas. The absence of Cr_2O_3 and slightly elevated Al_2O_3 and ASI are a direct consequence of initial high-pressure fractionation of olivine, Cr-bearing spinel, and minor clinopyroxene (Ulmer et al. 2018). The experimental starting material was prepared by mixing and homogenising pure-grade chemical compounds (oxides, hydroxides, silicates, and phosphates) in appropriate proportions. Two similar, but slightly different capsule setups, were employed. Most experiments were conducted with the same capsule design used by Marxer et al. (2022) representing a combination of the approaches of Kaegi et al. (2005) and Matjuschkin et al. (2015). The first inner capsule (outer diameter of 2.3 mm) was made from $Au_{90}Pd_{10}$ or Au_{100} and contained an aliquot of the starting material powder. For some low-temperature runs (FM107, FM108, and FM118), a layer of powdered zircon was added to the run charges as melt traps to promote the formation of residual melt pools large enough for EPMA analysis (Marxer and Ulmer 2019). However, infiltration of silicate liquid into the free pore space between single zircon grains was only of minor extent, and, consequently, this technique was discarded for later low-temperature experiments. The second inner capsule was made of Pt and filled with a NNO buffer assemblage (70% Ni and 30% $Ni(OH)_2$). These two inner capsules were placed in an outer capsule (outer diameter of 4.0 mm) together with the starting material powder acting as spacer material. Sporadically, buffer capsule failed resulting in uncertainties on the effective fO_2 levels in the experimental charges due to a decrease of water activity in the fluid coexisting with the fO_2 buffer assemblage. Therefore, the 400 MPa experiments were conducted with the capsule design of Matjuschkin et al. (2015), where powdered alumina and deionised water are loaded as spacer in the outer capsule. After preparation, sealed capsules were weighted and then either submerged in acetone or exposed to a temperature of 110 °C for several hours to check that they are intact.

Run procedure

Equilibrium crystallisation experiments at 600 and 800 MPa were conducted in a 14-mm bore end-loaded Boyd and England-type piston cylinder apparatus at ETH Zürich. NaCl-Pyrex-graphite-MgO assemblies were employed, and a

Table 1 Composition of the starting material rk54 (in wt.%). Oxide compounds were renormalised to an anhydrous base

Starting material	SiO_2	TiO_2	Al_2O_3	Fe_2O_3	FeO	MnO	MgO	CaO	Na_2O	K_2O	P_2O_5	H_2O	Fe^{3+}/Fe_{tot} [a]	xMg [b]	ASI [c]
rk54	47.89	0.86	18.45	1.81	8.59	0.25	8.04	11.13	1.85	0.98	0.16	3.50	0.159	0.585	0.758

[a]Ratio of ferric to total iron ($=Fe^{3+}/(Fe^{3+}+Fe^{2+})$) at NNO calculated for experimental run conditions using the algorithm of Kress and Carmichael (1991)

[b]$xMg = MgO/(MgO+FeO)$, molar ratio, all iron treated as Fe^{2+}

[c]Alumina Saturation Index ($ASI = Al_2O_3/(CaO+Na_2O+K_2O)$, molar ratio)

friction correction of 5% was applied (see Ulmer et al. (2018) for more details). Capsules were positioned in the assembly hotspot estimated with the numerical algorithm of Hernlund et al. (2006). Temperature was measured with a B-type thermocouple ($Pt_{94}Rh_6/Pt_{70}Rh_{30}$) with an estimated accuracy of ± 10 °C, and no correction for the pressure effect on the electromotive force (e.m.f.) was applied. Thermal modelling resulted that hotspot temperatures were 7–16 °C higher than thermocouple readings (Table 2). After loading, assemblies were pressurised at ambient temperature to approximately 400 MPa and subsequently heated with 40 °C/min to final run temperatures. Pressure was slowly increased when temperature exceeded 500 °C, but care was taken to reach final run pressures before heating was finished. During the experiments, oil pressure was controlled automatically at the target level allowing a maximum deviation of ± 40 MPa. Run durations varied from 20.5 to 96.5 h with increasing equilibration times with decreasing temperature. Experimental temperatures varied from 1110 to 900 °C with 30 °C steps. At high temperatures (> 1020 °C), few additional intermediate runs were performed with temperature intervals of 15 °C. Experiments were quenched by switching off the electric power supply resulting in cooling rates in the range of 100 °C/s.

Experiments at 400 MPa were run in a 22-mm bore non-end-loaded Johannes-type piston cylinder at ETH Zürich employing a modified NaCl-Pyrex-graphite-MgO low-pressure assembly calibrated by Marxer et al. (2022). Temperature was monitored with a B-type thermocouple ($Pt_{94}Rh_6/Pt_{70}Rh_{30}$) with an estimated accuracy of ± 10 °C and was varied between 1110 and 900 °C with 30 °C steps. Pressure was automatically controlled at target levels with an estimated uncertainty of ± 30 MPa. Run durations for the 400 MPa experiments ranged from 6.0 h at 1110 °C to 114.5 h at 900 °C. Cooling rates during quenching were slightly lower compared to the 14-mm assembly due to the higher thermal mass of the 22-mm assembly and varied between 50 and 100 °C/s. Experiments at higher temperatures were directly heated to final equilibration temperatures while run protocols for low-temperature experiments (900–1020 °C) were adapted due to distinct quench crystallisation, impeding the formation of residual melt pools large enough for reliable analysis. To promote the formation of larger crystals, we applied temperature cycling protocols (e.g. Mills and Glazner 2013; Erdmann and Koepke 2016), where temperature was cycled with ± 10 °C around the target equilibration temperature for half of the intended run duration. The employed heating and cooling rate during this cycling stage was 1 °C/min and plateau temperatures were hold for 20 min. This procedure was successful since experimental textures slightly coarsened and measurable melt pools formed down to the lowest temperature investigated.

To verify the attainment of 400 MPa employing the low-pressure piston cylinder calibration, two experiments (1050 and 960 °C) were repeated in internally heated pressure vessels (IHPV) at the Leibniz University Hannover. Identical double capsule designs and run protocols (i.e. heating rates and temperature cycling) were applied. Capsules were suspended using Pt wires in the furnace hot-spots of ca. 2 cm length (measured temperature gradient < 10 °C at run conditions). Temperatures were controlled and monitored using four S-type thermocouples ($Pt_{100}/Pt_{90}Rh_{10}$). Appropriate proportions of H_2 were added to the pressurising Ar gas to buffer intrinsic fO_2 conditions of the vessel during run performance close to NNO (Berndt et al. 2002). Experiments were quenched by fusing the Pt suspension wire with an applied power source inducing the capsules to fall out of the hotspot on a "cold" copper block resulting in quenching rates exceeding 100 °C/s at high temperatures.

Experiments at 200 MPa were conducted in externally heated Molybdenum-Hafnium-Carbide (MHC) pressure vessels at ETH Zürich. A gas mixture of Ar-CH_4 was used as pressurising medium, where methane acted as a reactant component buffering hydrogen fugacity, and, thus, oxygen fugacity (fO_2) in the experimental charges. Methane contents were selected such that imposed fO_2 conditions were close to the NNO buffer equilibrium (Marxer and Ulmer 2019). Vessels were loaded with required amounts of methane and, subsequently, pressurised with argon to approximately half of the desired run pressure. Upon heating, gas pressure increased simultaneously with temperature and was manually adjusted to final levels when target temperature was reached. Pressure was monitored using a pressure sensor with an accuracy of 0.5% and controlled at 200 MPa with a maximum deviation of ± 2 MPa. Temperature was monitored with a K-type thermocouple, positioned outside of the vessel that was previously calibrated against effective temperature inside the bomb. Estimated 2σ errors on temperature calibrations were below 10 °C. During the experiments, vessels were oriented with an inclination of 10° to ensure the formation of a stable temperature profile. Equilibration temperatures varied between 1110 and 930 °C with a step-size of 30 °C. Run duration ranged from 24 h at high temperatures to 122 h at 930 °C. Experiments were quenched by tilting the furnace by 90° into a vertical position allowing the capsules to fall to the cold end of the vessel, resulting in almost instantaneous isobaric quenches with cooling rates exceeding 100 °C/s.

Analytical techniques

After polishing, experimental charges were inspected with an optical microscope for capsule coherence and to detect any anomalous appearances. In addition, buffer capsules were checked for the presence of Ni and NiO to ensure that fO_2 buffering capability was maintained. The presence of a free fluid phase in the buffer capsules could not be verified

Table 2 Summary of experimental run conditions

Run	Temperature (°C)	Temperature Hotspot (°C)[c]	Duration (h)	Capsule material	Run products[e]	Phase proportions[f] (wt.%)	Melt Fraction[g] (vol.%)	Fe-loss[h] (rel.%)	$\sum R^{2}$ [i]	nom. H_2O[j] (wt.%)	Raman H_2O[l] (wt.%)	$logfO_2$[m] (ΔNNO)
800 MPa												
FM40	1110	1126	20.5	$Au_{90}Pd_{10}$[d]	melt, ol	99.2(5); 0.8(4)	99.4(5)	7.25	0.20	3.5	4.6(2)	− 1.09
FM85	1095	1108	47.0	$Au_{90}Pd_{10}$	melt, ol	97.9(3); 2.1(3)	98.3(3)	12.68	0.11	3.6		− 1.09
FM81	1080	1093	46.0	$Au_{90}Pd_{10}$	melt, cpx, ol	93.9(3); 3.8(4); 2.3(2)	95.2(3)	13.06	0.02	3.7		− 1.07
FM78	1065	1078	48.0	$Au_{90}Pd_{10}$[d]	melt, cpx, ol, sp	85.5(4); 11.6(4); 2.1(2); 0.8(1)	88.3(4)	2.95	0.01	4.1		− 0.99
FM90	1050	1059	42.0	$Au_{90}Pd_{10}$	melt, cpx, plag, ol, sp(t)	74.2(16); 12.7(11); 7.6(11); 5.5(6)	77.9(17)	16.55	0.12	4.7	5.4(1)	− 0.86
FM104	1020	1032	25.0	$Au_{90}Pd_{10}$	melt, cpx, plag, ol, sp(t)	59.3(3); 16.8(2); 15.6(2); 8.3(1)	64.5(4)	13.72	0.00	5.9		− 0.63
FM94	990	998	48.0	$Au_{90}Pd_{10}$	melt, amph, cpx, plag, opx(t)	50.8(6); 30.1(8); 12.3(5); 6.8(4)	56.5(7)	8.60	0.02	5.7	6.3(2)	− 0.67
FM96	960	969	72.5	Au_{100}	melt, amph, plag, cpx, opx(t)	38.6(4); 41.9(7); 11.5(3); 8.0(4)	44.6(5)	6.73	0.02	6.9		− 0.43
FM99	930	937	71.0	Au_{100}	melt, amph, plag, cpx, opx(t)	24.2(6); 56.7(13); 15.2(5); 4.0(8)	30.5(8)	5.22	0.04	9.8		− 0.07
FM107	900	908	81.5	Au_{100}	melt, amph, plag, cpx, opx(t), ap(t), zr[n]	18.0(5); 58.5(12); 20.2(5); 3.3(7)	23.4(7)	4.47	0.04	10.1[k]		0.00
600 MPa												
FM75	1080	1093	48.0	$Au_{90}Pd_{10}$[d]	melt, ol	98.9(3); 1.1(3)	99.2(3)	− 5.98	0.11	3.5		− 0.92
FM49	1065	1079	48.5	$Au_{90}Pd_{10}$[d]	melt, ol	97.3(4); 2.7(4)	97.9(4)	12.04	0.16	3.6		− 0.96
FM73	1050	1063	48.0	$Au_{90}Pd_{10}$[d]	melt, ol, plag, cpx	85.3(6); 6.3(2); 5.3(4); 3.2(4)	87.4(7)	− 2.27	0.01	4.1	4.0(2)	− 0.80
FM86	1035	1046	48.0	$Au_{90}Pd_{10}$	melt, plag, cpx, ol	77.2(9); 8.8(6); 7.1(5); 6.9(3)	80.4(9)	9.91	0.03	4.5		− 0.72
FM95	1020	1031	48.0	$Au_{90}Pd_{10}$	melt, plag, cpx, ol, sp	67.6(5); 12.3(3); 11.7(4); 6.3(2); 2.0(1)	72.3(6)	–	0.02	5.2	4.6(1)	− 0.56
FM87	990	1001	48.0	$Au_{90}Pd_{10}$	melt, plag, cpx, ol, amph	58.1(5); 17.0(7); 11.9(5); 9.7(5); 3.3(1.7)	63.3(5)	8.56	0.01	5.9		− 0.45
FM97	960	970	72.0	Au_{100}	melt, plag, amph, cpx, ol	39.1(5); 21.3(10); 21.2(24); 10.5(7); 7.9(8)	45.6(6)	7.17	0.02	7.9		− 0.16
FM100	930	937	71.0	Au_{100}	melt, amph, plag, opx, cpx	24.6(9); 43.3(26); 21.5(13); 5.3(15); 5.2(7)	30.4(11)	8.11	0.02	8.7[k]		0.00
FM108	900	907	96.5	Au_{100}	melt, amph, plag, opx, cpx, ap(t), zr[n]	14.7(12); 53.5(48); 25.2(21); 4.1(27); 2.5(12)	19.1(16)	4.26	0.05	8.9[k]		0.00
400 MPa												
FM137	1110	1124	6.0	$Au_{90}Pd_{10}$	melt, ol	99.2(4); 0.8(4)	99.4(4)	15.95	0.18	3.5	4.5(1)	− 0.72
FM133	1080	1092	22.5	$Au_{90}Pd_{10}$	melt, ol	96.8(1); 3.2(1)	97.5(1)	13.28	0.02	3.6		− 0.75
FM130	1050	1062	26.0	$Au_{90}Pd_{10}$	melt, cpx, plag, ol	79.1(4); 8.4(2); 6.6(3); 5.8(1)	82.4(5)	11.81	0.01	4.4	5.1(1)	− 0.57

Table 2 (continued)

Run	Temperature (°C)	Temperature Hotspot (°C)[c]	Duration (h)	Capsule material	Run products[e]	Phase proportions[f] (wt.%)	Melt Fraction[g] (vol.%)	Fe-loss[h] (rel.%)	$\sum R^{2}$ [i]	nom. H_2O[j] (wt.%)	Raman H_2O[l] (wt.%)	$logfO_2$[m] (ΔNNO)
FM201[a]	1050	1050	25.0	$Au_{90}Pd_{10}$	melt, plag, ol, cpx	76.0(5); 11.8(3); 8.5(2); 3.7(3)	79.2(6)	11.27	0.01	4.6		− 0.46
FM155	1020[b]	1032	29.0	$Au_{90}Pd_{10}$	melt, plag, cpx, ol	64.7(18); 14.5(13); 12.1(12); 8.7(7)	69.5(20)	14.56	0.15	5.4		− 0.36
FM158	990[b]	1002	48.5	Au_{100}	melt, plag, amph, cpx, ol	49.7(12); 16.2(20); 15.5(48); 11.6(13); 7.1(16)	55.8(14)	13.10	0.08	6.4		− 0.20
FM161	960[b]	971	72.0	Au_{100}	melt, amph, plag, cpx, ol	35.4(9); 31.8(42), 20.2(16); 6.7(12); 5.8(14)	41.6(10)	8.66	0.05	7.0[k]	8.3(5)	0.00
FM202[a]	960[b]	954	72.5	Au_{100}	melt, amph, plag, ol, cpx	33.5(3); 29.4(17), 23.4(6); 8.1(6); 5.5(5)	39.7(4)	3.22	0.01	7.2[k]		0.00
FM162	930[b]	940	97.5	Au_{100}	melt, amph, plag, opx, cpx	21.5(12); 45.4(34); 23.5(17); 6.8(18); 2.8(10)	26.4(15)	6.08	0.04	7.1[k]		0.00
FM159	900[b]	909	114.5	Au_{100}	melt, amph, plag, opx, ap	12.9(10); 52.1(33); 28.3(16); 6.4(22); 0.2(2)	16.6(13)	6.96	0.05	7.3[k]		0.00
200 MPa												
FM117	1110	–	24.0	$Au_{90}Pd_{10}$	melt, ol	98.3(2); 1.7(2)	98.7(2)	3.30	0.04	3.6		− 0.38
FM109	1080	–	24.0	$Au_{90}Pd_{10}$	melt, plag, ol	92.7(10); 3.8(7); 3.5(3)	93.7(10)	1.02	0.06	3.8	3.6(1)	− 0.31
FM110	1050	–	27.5	$Au_{90}Pd_{10}$	melt, plag, ol	78.6(12); 13.3(9); 8.1(4)	81.0(12)	4.07	0.10	4.5	3.9(0)	− 0.09
FM120	1020	–	49.0	$Au_{90}Pd_{10}$	melt, plag, cpx, ol, mt	39.1(3); 30.5(2); 14.8(2); 8.1(1); 7.6(1)	45.6(3)	–	0.01	5.0[k]		0.00
FM122	990	–	76.0	Au_{100}	melt, plag, cpx, ol, mt, opx(t)	29.8(6); 36.3(5); 17.0(5); 8.6(3); 8.3(1)	35.9(7)	–	0.05	5.0[k]		0.00
FM114	960	–	74.0	Au_{100}	melt, plag, cpx, ol, mt, opx(t), amph(t)	25.3(6); 39.6(6); 17.8(6); 9.4(3); 7.8(2)	31.0(8)	–	0.07	5.1[k]		0.00
FM118	930	–	122.0	Au_{100}	melt, plag, opx, amph, cpx, mt, ap(t), bt(t), zr[n]	10.6(13); 43.6(22); 14.5(24); 13.1(55); 11.8(18); 6.3(3)	13.7(16)	–	0.12	5.3[k]		0.00

Abbreviations for mineral phases: *ol* olivine, *cpx* clinopyroxene, *opx* orthopyroxene, *amph* amphibole, *plag* plagioclase, *sp* hercynitic spinel, *mt* magnetite, *bt* biotite, *ap* apatite, *zr* zircon

[a]IHPV repetition experiment

[b]Run where temperature cycling of ± 10 °C was applied for half of the run duration (see text for more details)

[c]For piston cylinder assemblies, hotspot temperatures were estimated employing the model of Hernlund et al. (2006)

[d]Run performed with Fe-presaturated capsule

[e]Identified stable phase assemblage. Phases which were only present in trace amounts are indicated with (t)

[f]Phase proportions (in wt.%) established by mass balance regression. Numbers in parentheses represent standard deviations (1σ) and read as follows: 99.2(5) equals 99.2 ± 0.5

[g]Melt fractions established by mass balance converted from wt.% to vol.% for rheological considerations. For more details on calculation procedure, see text

[h]Fe-loss calculated by mass balance regression and expressed relative to the FeO content of the starting material. For few runs, Fe-loss was not calculated due to the presence of an Fe-Ti-oxide phase

[i]$\sum R^2$ is the sum of the squared residuals from mass balance regression

Table 2 (continued)

[j]Nominal H_2O contents of residual liquids (in wt.%) calculated via mass balance
[k]Water-saturated runs, where H_2O contents were calculated with the Burnham model
[l]H_2O contents of residual liquids (in wt.%) measured via Raman spectroscopy
[m]Minimum fO_2 conditions (in ΔNNO) estimated via water activity based on nominal melt water contents
[n]Zircon was present owing to its usage as a melt trap

for all experiments during capsule piercing due to occasional buffer capsule failure caused by alloying of platinum with nickel and resulting embrittlement. However, the presence of a fluid phase in the outer capsules was identified for all runs. Overview BSE images of specimens and first qualitative compositional data of glasses and minerals were obtained with a JEOL JSM-6390 Scanning Electron Microscope equipped with a standardised Thermo Fisher NORAN NSS7 Energy Dispersive Spectroscopic system (SEM–EDS) at ETH Zürich with an acceleration voltage of 15 kV. Subsequently, major phases (glass, olivine, spinel, plagioclase, clinopyroxene, orthopyroxene, amphibole, biotite, and apatite) were analysed with either a JEOL JXA 8200 or a JEOL JXA 8230 Superprobe at ETH Zürich. The same set of oxide and silicate standards was utilised for both devices, and a comparison of analytical results revealed no major differences. An acceleration voltage of 15 kV was used, and sodium and potassium were always measured first to avoid extensive alkali migration. Counting times on peak and background were 10 to 15 s for Na and K, and 20 to 40 s for other elements. Hydrous glasses were analysed with a beam current of 7 nA and a beam diameter of 20 µm. In case melt pools were too small for these conditions, beam currents were reduced to 4 or 2 nA and spot sizes to 10 or 5 µm. Plagioclase, biotite, and apatite were analysed with a focussed beam and a current of 10 nA, while pyroxene, amphibole, olivine, and spinel were measured with a focussed beam and a current of 20 nA. Well-characterised reference materials and calibration standards were regularly measured as unknowns during analytical sessions to detect any instrumental drift and ensure the collection of high-quality data.

IHPV repetition experiments at 400 MPa were analysed with a JEOL JXA-iHP200F Field Emission EPMA at the Leibniz University Hannover using an acceleration voltage of 15 kV. For glasses, well-characterised standard glasses were used for calibration while mineral and oxide standards were utilised for the analysis of experimental mineral phases. During analytical sessions, secondary reference materials and calibrations standards were regularly measured as unknows to correct for instrumental drift as well as monitor accuracy and precision. Glasses were analysed with an acceleration voltage of 15 kV, a beam current of 10 nA and a diameter of 12 µm, while 15 nA and a focussed beam were used for mineral phases (olivine, clinopyroxene, plagioclase, and amphibole).

Melt water contents of selected runs were determined by Raman spectroscopy at KU Leuven using a Horiba LabRAM HR Evolution System. Samples were excited with a Nd:YAG laser with a wavelength of 532 nm, and a grating of 1800-groove/mm was applied. Analysis were performed with a 100x magnification objective corresponding to a laser spot size smaller than 1.5 µm. Measurements were done with a pinhole aperture of 50 µm over a spectral

window from 50 to 4000 cm^{-1}. Acquisition times varied between 50 to 200 s per frame with two accumulations. A spike filter was applied to remove any non-repetitive spikes. Laser energy was varied between 100 and 25% to avoid any damage of the sample influencing the signal quality. Raw spectra were processed following the approach of Le Losq et al. (2012). Water contents were quantified employing an in-house linear calibration (van Gerve and Namur 2023) based on various well-characterised water-bearing standard glasses where the area ratio between the high-wavenumber OH band (3000–4000 cm^{-1}) and the low-wavenumber silicate bands (15–1500 cm^{-1}) is related to the melt water content (in wt.%).

Results

An overview of experimental run conditions (including capsule materials, phase assemblages, phase proportions, estimated iron losses, calculated and selectively measured melt water contents, and estimated fO_2 conditions) is provided in Table 2 and in the Electronic Supplementary Material ESM2.

General remarks

Recovered experimental charges consisted of residual silicate melt quenched to a homogenous glass and a variety of mineral phases, namely: olivine (ol), clinopyroxene (cpx), orthopyroxene (opx), plagioclase (plag), hercynitic spinel (sp), amphibole (amph), magnetite (mt), biotite (bt), and apatite (ap). Vapour bubbles were observed in all recovered charges and can be explained by the presence of additional volatile compounds such as N_2 or CO_2. Nitrogen incorporation is related to the capsule preparation procedure and the entrainment of air, while CO_2 was most probably introduced via the reactive synthetic starting materials. Previous studies revealed that synthetic oxide mixtures tend to absorb significant proportions of CO_2 from air (Alonso-Perez et al. 2009; Marxer et al. 2022) and storage of starting material powders at 110 °C immediately before capsule loading is insufficient to prevent this uptake. For few low-temperature (and low-pressure) experiments, the formation of vapour bubbles is the result of the attainment of water-saturated conditions as revealed by mass balance calculations and modelling of H_2O saturation levels employing the Burnham model (Burnham and Davis 1974; Burnham 1994) (compare Table 2).

Water contents of experimental glasses were estimated via mass balance and reveal a progressive increase with decreasing temperature for each crystallisation series. This systematic enrichment in H_2O is further supported by similar evolution trends of water concentrations estimated via the by-difference method employing EPMA analytical totals (100 wt.% - EPMA total ≈ H_2O content) (e.g. Anderson 1973; Blundy and Cashman 2008; Hughes et al. 2019). However, water contents derived by the by-difference method are ~ 2 wt.% higher than the values obtained by mass balance, which is potentially related to a matrix effect during EPMA analysis and data correction when standardising on mineral phases (e.g. Hughes et al. 2019). Melt water contents established for selected runs via Raman spectroscopy generally match nominal water contents calculated via mass balance and verify a continuous increase of H_2O contents upon crystallisation (Table 2). Minor deviations for some runs can be explained by diffusion of hydrogen into noble metal capsules resulting (in combination with Fe-loss) in H_2O-gain of experimental charges. However, we infer that the impact of this additional water on phase equilibria and LLDs was of a minor extent, supported by the observed smooth and consistent differentiation trends.

Experiments were buffered close to the NNO equilibrium. Due to the water-undersaturated character of the experiments, fO_2 conditions during the runs were displaced by the factor of 2*log(aH_2O) (where aH_2O equals the activity of water in the experimental charge) from the ideal buffer equilibrium and only experiments that reached water-saturation ($aH_2O = 1$) experienced redox conditions corresponding to NNO. Thus, minimum levels of fO_2 were calculated based on estimated water activity in the experimental charges (Table 2). Water activities were approximated with the Burnham model (e.g. Burnham and Davis 1974; Burnham 1994) following the identical procedure as described in detail in Marxer et al. (2022) based on melt H_2O contents estimated via mass balance. A summary of employed calculation parameters is reported in the Electronic Supplementary Material ESM3. In Marxer et al. (2022), identical capsule setups and experimental facilities were used and independent fO_2 estimates via the solubility of Fe in AuPd (Barr and Grove 2010) confirmed the attainment of targeted redox conditions (NNO-1 to NNO). However, the early saturation of magnetite as well as reconstructed fO_2 via Fe–Mg exchange between olivine and melt (Blundy et al. 2020) indicate that the experiments at 200 MPa experienced slightly more oxidising redox conditions (~ NNO + 1, see ESM2 for more details) compared to runs at higher pressures. The fO_2 conditions of the high-pressure experiments (400–800 MPa) are with NNO-1 to NNO at the lower end of the range of natural arc magmas (e.g. Carmichael 1991; Cottrell et al. 2021) resulting in arc-tholeiitic differentiation trends, while the 200 MPa series evolves along a calc-alkaline trajectory. However, we infer that this mainly affects FeO and TiO_2 contents of experimental residual liquids due to delayed Fe-Ti-oxide crystallisation but not the general evolution of the other major element compounds and ASIs.

Iron-loss from run charges was estimated via mass balance (treating FeO as an additional phase) and expressed

relative to the initial iron content of the starting material (Table 2). Calculated Fe-losses are below 16.6% with a majority (ca. 70%) < 10%. Fe-loss is positively correlated with run temperature, and a change of capsule materials from $Au_{90}Pd_{10}$ to Au_{100} is accompanied by an overall decrease of iron-loss as the solubility of iron in AuPd alloys decreases with decreasing Pd content (Barr and Grove 2010). Fe-loss was not established for experimental charges saturated in Ti-poor-magnetite as mass balance calculation procedures cannot distinguish between iron alloying with the capsule metals and modal Fe-Ti-oxide. For these charges, oxide phase proportions were independently estimated via image processing employing ImageJ and BSE pictures of entire run charges, as follows: First, the capsule metal as well as all voids and cracks were manually removed from the images. In a next step, oxide proportions were estimated assuming that area fractions equal volume fractions. Finally, volume proportions were converted to mass fractions employing calculated densities of coexisting phases (compare *Phase equilibria and phase proportions* for details on density calculations). Fe-losses were then recalculated via mass balance employing oxide fractions obtained by image processing. However, resultant Fe-losses were negative (inferring iron-gain), which is unrealistic as capsule metals were nominally iron-free. We attribute this feature to the major drawback of the image processing approach that the underlying assumption of homogeneous distribution of Fe-Ti-oxides in experimental charges is likely incorrect. For example, magnetite tends to nucleate on capsule walls or to accumulate on volatile bubbles by floating (e.g. Knipping et al. 2019). Accounting for this uncertainty by assuming a relative error of 20% on Fe-Ti-oxide fractions established via image analysis resulted in maximum estimated Fe-loss close to zero. Therefore, instead of reporting negative iron losses, we decided to repeat mass balance calculations ignoring any potential alloying of iron with the capsule metal. For some high-temperature runs of the 800 and 600 MPa series, Fe-presaturated $Au_{90}Pd_{10}$ capsules were employed, resulting in weakly negative Fe-losses, i.e. Fe-gain (Table 2). Therefore, for later runs, we favoured the use of unconditioned capsules.

Appearance of run products

Experimental charges are characterised by the homogeneous distribution of residual melt pools and mineral phases. Only few runs exhibited weak gradients in phase abundances, which can be attributed to minor temperature gradients favouring the crystallisation of minerals in the low-temperature areas and elevated melt proportions in the proximity of the thermal hotspot. Calculations with the algorithm of Hernlund et al. (2006) showed that intercapsule temperature gradients were below 10 °C and, thus, had no significant influence on phase equilibria. Residual melts and mineral phases were analysed throughout entire capsule sections, and no systematic compositional variations were detected.

Due to the large range of explored pressure and temperature conditions and the employment of different experimental techniques, textures and general appearances of recovered run charges varied significantly (Fig. 1). Minor quench crystallisation was observed in some experiments performed in the end-loaded piston cylinder apparatus (800 and 600 MPa) and mainly consisted of feathery quench overgrowth on clinopyroxenes and amphiboles (Fig. 1a and c) or thin high-albite rims on plagioclase crystals. However, we took care to select large enough melt pools for EPMA analyses to avoid any quench crystallisation influence on obtained residual liquid compositions. In the experiments run in the non-end-loaded piston cylinder apparatus (400 MPa), quench crystallisation was distinctly more abundant (Fig. 1e) due to slower quenching rates. The formation of extensive biotite and amphibole quench crystals impeded reliable analysis of residual melt pools necessitating the modification of experimental run procedures and the implementation of temperature cycling protocols. Quench crystallisation was completely absent for the 200 MPa externally heated pressure vessel experiments and the 400 MPa internally heated pressure vessel (IHPV) runs because of the achievement of near-instantaneous quenches. Starting material relics indicative of incomplete reaction and disequilibrium represented by unreacted Al_2O_3 present in the cores of plagioclase crystal clusters were only identified in trace amounts in a few low-temperature runs (900–930 °C, FM99, FM100, FM107, FM108, and FM118).

Olivine crystals were of equant shape and varied in size between 5–30 µm (Fig. 1). In many experiments, rounded crystals were observed, which we attribute to olivine crystallisation kinetics, where olivine tends to start crystallising at the beginning of an experiment and is resorbed with ongoing run duration due to the formation of additional phases until the final equilibrium phase assemblage is reached. Similarly, olivine coexisting with magnetite (runs FM95, FM120, FM122, FM114, and FM118) exhibited a core-rim zonation with more iron-rich cores (i.e. higher in fayalite component) compared to rims. Analogous to the rounded shapes, this can be related to the crystallisation behaviour of olivine and magnetite in our experiments. Due to delayed magnetite saturation, early formed olivine cores are relatively iron-rich. Upon subsequent magnetite saturation, olivine compositions re-adjusted to changing iron contents of the coexisting liquid but could not completely re-equilibrate throughout the entire crystal grains resulting in the preservation of the observed weak chemical zonation.

Clinopyroxene crystals were predominantly small, equant shaped (< 10 µm) and partly exhibited bright metastable

low-alumina cores (Fig. 1a). Such cores were less abundant in experiments with longer run durations indicating that their formation is related to crystallisation kinetics or disequilibrium. Clustering of clinopyroxene crystals was observed in several experiments (Fig. 1f). Clinopyroxenes formed at 1050 °C and 400 MPa (runs FM130 and FM201) exhibited weak sector zonation, most prominent in alumina contents. This feature has already been described by previous experimental studies (e.g. Nandedkar et al. 2014; Ulmer et al. 2018; Marxer et al. 2022) and is related to pyroxene crystallisation kinetics. Plagioclase crystallised as small hypidiomorphic laths or prismatic grains (< 20 µm). Generally, crystals were larger in experiments close to the first appearance of plagioclase in the crystallisation sequence (10–30 µm, Fig. 1a and g), and formed distinctly smaller grains with increasing temperature difference to the plagioclase liquidus (< 5 µm, Fig. 1f and h). In the 200 MPa low-temperature runs, plagioclase was very small, and reliable analysis via EPMA was challenging. Amphibole crystals were idiomorphic and showed a similar trend of decreasing grains sizes with decreasing temperature (> 100 µm for high-T runs and around 10 µm at low temperatures, Fig. 1b, d, and f). In most experiments, amphibole was homogeneous and devoid of any zonation. However, amphibole synthesised in run FM158 (990 °C and 400 MPa) exhibited weak oscillatory zoning in Al, Fe, and Mg related to temperature cycling (Fig. 1e). Furthermore, in the 200 MPa experiments FM114 (960 °C) and FM118 (930 °C), amphibole exhibited a weak core-rim zonation with cores enriched in Fe and Ti, which can be related to the delayed saturation of magnetite in these experiments. Orthopyroxene morphologies were similar to amphibole, forming idiomorphic crystals with elongated needle-like or prismatic shapes. The length of orthopyroxene crystals decreased from 100–200 µm to about 10–20 µm at lower temperatures. Orthopyroxene crystallised in the 400 MPa runs at 930 and 900 °C exhibited oscillatory zoning in Al, Fe, and Mg, related to temperature cycling (Fig. 1f). In one experiment (FM94, 990 °C and 800 MPa), weak sector zonation could be identified based on BSE images. Hercynitic spinel formed small and idiomorphic crystals (< 5 µm, Fig. 1a). Idiomorphic magnetite was relatively large (10–30 µm, Fig. 1h). Biotite crystallised only in run FM118 (930 °C and 200 MPa) in the form of small anhedral to hypidiomorphic platelets with a maximum length of 20 µm, while apatite crystals were short-prismatic or acicular, but very small (< 5 µm).

Attainment of equilibrium

The following observations indicate that experimental equilibrium was attained for our runs: (1) Run textures do not reveal any indications of pronounced disequilibrium. Recovered charges exhibited homogeneous appearance, and relics from starting materials were basically absent or only present in trace amounts in a few low-temperature experiments. Minerals are euhedral, and quench crystallisation was either absent or minor (i.e. not affecting the reliable analysis of stable phases). (2) Residual melts and mineral phases were chemically homogeneous over entire capsule cross-sections, and no spatial compositional gradients were detected, except minor chemical zonation identified for amphibole and pyroxene crystals in some low-temperature experiments. (3) Melt and mineral compositions define smooth and consistent evolution trends with differentiation. (4) Distribution of major element pairs between stable minerals and residual melt (e.g. Fe–Mg for olivine, pyroxenes, and amphibole or Ca-Na for plagioclase) describe systematic variations with decreasing temperature (see Electronic Supplementary Material ESM4). (5) Calculated crystallisation temperatures for experimental amphiboles using the edenite-richterite thermometer of Holland and Blundy (1994) reproduce run conditions within reported model uncertainty (see ESM4).

Phase equilibria and phase proportions

Stable phase assemblages and phase relations are summarised in Fig. 2. Each hexagon represents an experiment, and the smaller coloured triangles illustrate stable mineral phases. Interpolated mineral saturation curves are indicated with coloured lines. Liquidus temperatures were not explicitly explored, but trace abundances of olivine in the 1110 °C runs indicate conditions close to the liquidus, which is estimated between 1110 and 1140 °C for all investigated pressures. Olivine represents the liquidus phase from 200 to 800 MPa, and clinopyroxene saturation temperature increases with increasing pressure, located between 1020 and 1050 °C at 200 MPa and 1080 and 1095 °C at 800 MPa. In contrast, plagioclase stability increases with decreasing pressure and saturates between 1050 and 1065 °C at 800 MPa and 1080 and 1110 °C at 200 MPa. Therefore, plagioclase and clinopyroxene saturation curves intersect between 400 and 600 MPa and 1050–1080 °C. Amphibole joins the solid phase assemblage at 990 °C between 400–800 MPa, and at slightly lower temperature (960 °C) at 200 MPa. Orthopyroxene saturation denotes a rather particular evolution in pressure and temperature space. At 800 and 200 MPa, crystallisation initiates above 990 °C, while being delayed to 930–960 °C at 400–600 MPa. Interestingly, at 800 MPa, amphibole and orthopyroxene crystallisation coincide, while at 200 MPa orthopyroxene appears 30 °C earlier than amphibole. From 400 to 800 MPa, orthopyroxene appearance coincides with the disappearance of olivine indicative of a peritectic relationship in the form of ol + liq = opx, which is further supported by sporadic relic olivine inclusions in orthopyroxene. At 200 MPa, olivine and orthopyroxene coexist at 960 and 990 °C requiring the

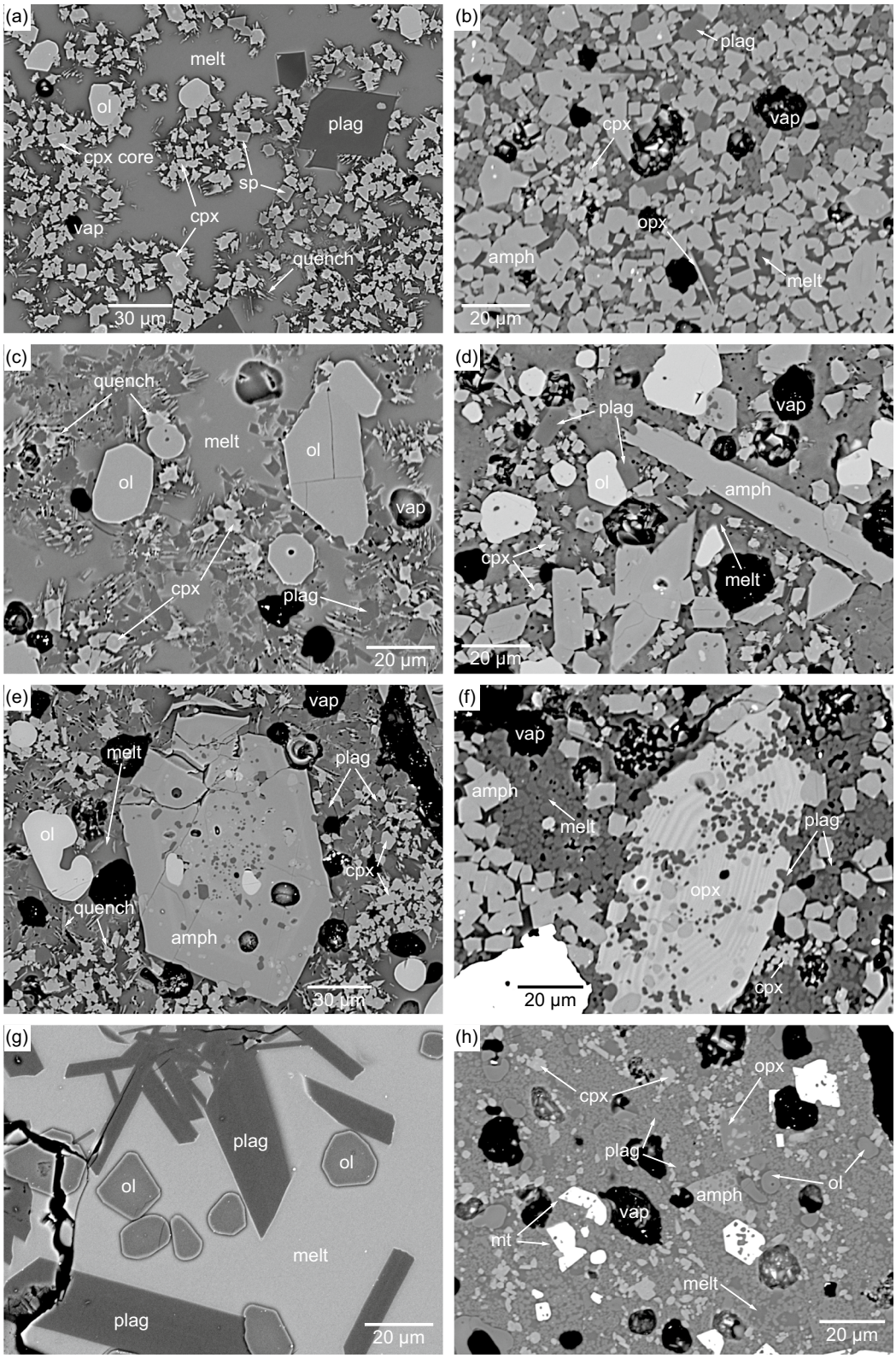

Fig. 1 Representative BSE pictures of experimental charges. Phase abbreviations are: olivine (ol), clinopyroxene (cpx), orthopyroxene (opx), plagioclase (plag), amphibole (amph), hercynitic spinel (sp), magnetite (mt), and vapour (vap). **a** FM90 (1050 °C and 800 MPa) with metastable low-alumina cores in cpx; **b** FM99 (930 °C and 800 MPa); **c** FM86 (1035 °C and 600 MPa); **d** FM97 (960 °C and 600 MPa); **e** FM158 (990 °C and 400 MPa) with oscillatory zoned amphibole; **f** FM162 (930 °C and 400 MPa) with oscillatory zoned orthopyroxene; **g** FM109 (1080 °C and 200 MPa); **h** FM114 (960 °C and 200 MPa)

delineation of an "ol-out" curve in the P–T diagram related to delayed amphibole saturation resulting in a short interval where olivine and orthopyroxene coexist along the ol-opx peritectic curve before complete consumption of olivine in the amphibole-forming reaction. Apatite saturation was observed between 900 and 930 °C at 400–800 MPa and occurs at slightly higher temperatures at 200 MPa (930–960 °C). Biotite saturation was identified at 930 °C and 200 MPa but was absent at higher pressures. Hercynitic spinel was only observed at 800 MPa from 1065 to 1020 °C, while, at 600 MPa, magnetite stabilised at 1020 °C but already disappeared at 990 °C. This disappearance of spinel phases in the range 1020 to 990 °C at 600 and 800 MPa can be related to the onset of amphibole crystallisation, pointing towards consumption of spinel phases in the amphibole-forming peritectic reaction at high pressures. At 400 MPa, oxide crystallisation was not observed over the entire temperature range investigated. At 200 MPa, magnetite saturated at relatively high temperatures (1020–1050 °C) and was stable to the lowest temperature explored (930 °C). This could be related to slightly higher fO_2 conditions in the externally heated pressure vessel runs (i.e. NNO to NNO + 1).

Phase proportions of experimental charges (and corresponding errors, in wt.%) were determined by mass balance employing compositions of stable phases (residual melt and minerals) and the starting material (Fig. 3, Table 2) and the linear regression tool implemented in Microsoft Excel. For calculations, all major and minor element compounds were considered. Crystallinity progressively increases with decreasing temperature for all four experimental series. At 800 MPa, olivine, clinopyroxene, and plagioclase proportions exhibit a nearly continuous increase until amphibole starts crystallising, resulting in the disappearance of olivine and a substantial reduction of clinopyroxene and plagioclase fractions. Upon further cooling, amphibole and plagioclase proportions increase accompanied by a decrease of clinopyroxene. At 600 and 400 MPa, phase proportions are very similar. For both series, plagioclase fractions show a continuous increase with decreasing temperature, whereas olivine and clinopyroxene proportions exhibit an increase at higher temperatures followed by a continuous decrease after amphibole saturation. The IHPV repetition experiment at 1050 °C exhibits slightly higher plagioclase and olivine fractions and diminished clinopyroxene proportions compared to the corresponding piston cylinder run. However, at 960 °C phase proportions are comparable between both experimental approaches. At 200 MPa, olivine and plagioclase exhibit a steady increase from 1110 to 1050 °C, followed by a distinct jump of modal plagioclase at 1020 °C coinciding with the saturation of clinopyroxene and magnetite corresponding to a shift from the ol-plag on the (ol-)plag-cpx-mt cotectic curve promoting extensive crystallisation. In addition, this abrupt change is related to the attainment of water-saturation (compare Table 2): as long as magmas are H_2O-undersaturated an increase of water contents due to the crystallisation of nominally anhydrous minerals has a destabilising effect on silicates and, therefore, delays progressive crystallisation, especially of plagioclase (e.g. Sisson and Grove 1993; Waters and Lange 2015). However, upon water-saturation this effect vanishes, resulting in extensive crystallisation. Between 1020–960 °C, proportions of olivine, clinopyroxene, and magnetite are constant, while plagioclase shows a minor increase. Finally, at 930 °C, pronounced crystallisation of amphibole and orthopyroxene results in the consumption of olivine and a significant decrease of clinopyroxene.

In summary, mineralogies at 400–800 MPa converge with decreasing temperature resulting in a cumulate assemblage

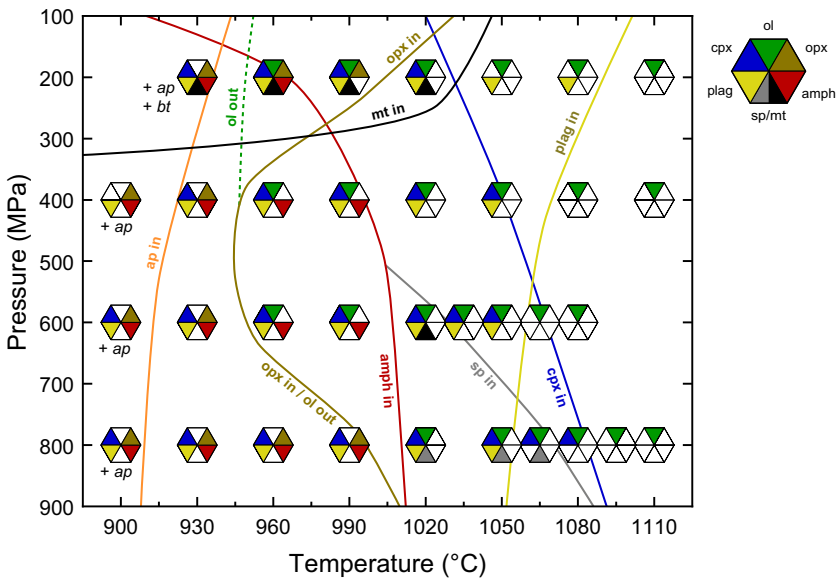

Fig. 2 Pressure–temperature phase diagram with phase assemblages and mineral saturation curves summarising the experimental results. Each hexagon represents a single experiment and small coloured triangles illustrate the presence (coloured) and absence (empty symbol) of stable mineral phases. For mineral abbreviations, see caption of Fig. 1, plus biotite (bt) and apatite (ap)

consisting of two-thirds amphibole and one-third plagioclase (with minor pyroxenes) corresponding to amphibole-(mela-)gabbros. In contrast, the mineral assemblage formed at 200 MPa is characterised by higher proportions of plagioclase and pyroxenes and reduced amounts of amphibole representing a magnetite-bearing amphibole-two pyroxene (leuco-)gabbro. The impact of pressure on phase equilibria is well documented by plagioclase and amphibole proportions. The amount of amphibole decreases with decreasing pressure, while plagioclase proportions increase at low pressure.

Residual melt fractions (in vol.%) reveal a continuous decrease with increasing SiO_2 and decreasing MgO contents (Fig. 4). For rheological considerations, weight proportions (wt.%) established by mass balance were transformed to volume fractions (vol.%). Required densities of silicate melts were calculated employing the Lange and Carmichael (1987) algorithm, whereas mineral densities were established assuming ideal mixing among mineral endmembers. Densities of mineral endmembers were calculated using a Birch-Murnaghan equation of state and an own compilation of thermodynamic parameters (e.g. molar volumes, thermal expansivity coefficients, bulk moduli) for each mineral endmember of interest (Electronic Supplementary Material ESM5). The 400–800 MPa series exhibit overlapping evolution trends of residual melt fractions with progressive differentiation while the 200 MPa trajectory deviates slightly from the former. This difference is most prominently shown by SiO_2 vs melt fraction, where the low-pressure trend exhibits higher silica contents for identical melt fractions. One explanation is the attainment of H_2O-saturated conditions at low-pressure triggering extensive crystallisation of plagioclase and Fe-Ti-oxides resulting in a pronounced enrichment of residual liquids in silica. The high-pressure trends cross the rigid percolation threshold (PRT, rheological transition

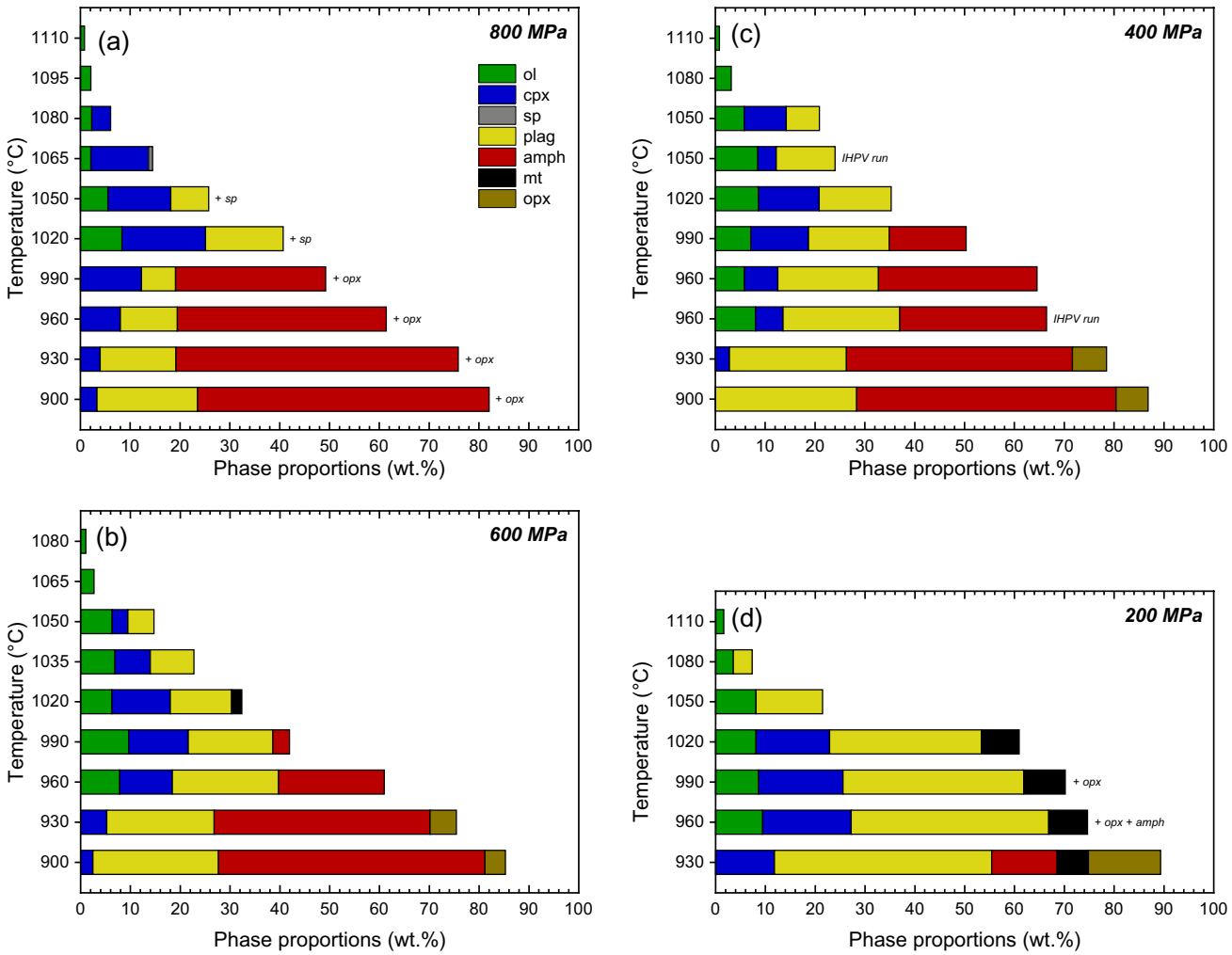

Fig. 3 Mineral phase proportions (in wt.%) of the four isobaric equilibrium crystallisation series calculated by mass balance calculations. Phases only present in trace amounts, that were not considered for mass balance calculations, are indicated in italic letters (compare Table 2). For phase abbreviations, see captions of Figs. 1 and 2

from a mobile magma to a rigid crystal mush at ~ 45 vol.% of residual melt, (Vigneresse et al. 1996)) at 55 wt.% of SiO_2 (resp. 3–3.5 wt.% MgO) and the 200 MPa trend at 59–60 wt.% SiO_2 (4 wt.% MgO). Likewise, all four experimental series become completely locked up due to the attainment of closed crystal packing (= particle locking threshold, PLT, ~ 25–28 vol.% of residual melt (Vigneresse et al. 1996)) at SiO_2 between 58 to 64 wt.% (1.5–2.2 wt.% MgO).

Phase compositions

Major and minor element compositions of residual liquids and coexisting minerals (in wt.%) are reported in Table 3 and in the Electronic Supplementary Material ESM6. Chemical trends of mineral phases (olivine, clinopyroxene, orthopyroxene, plagioclase, amphibole, and spinel) are presented and discussed in detail in the Electronic Supplementary Material ESM4.

Residual liquids

Compositional trends of residual liquids (in wt.%, recalculated on an anhydrous base) as a function of MgO contents and contoured for temperature are illustrated in Fig. 5. The black star illustrates the composition of the starting material (rk54). Liquid lines of descent (LLD) follow arc tholeiitic (400–800 MPa) or calc-alkaline (200 MPa) differentiation trends with increasing silica and alkali contents accompanied by continuously decreasing MgO and cover the compositional range from basaltic to dacitic.

SiO_2 contents exhibit a two stage increase with decreasing MgO from 48 wt.% to 64–66 wt.% (Fig. 5a). An initial interval at high MgO contents (6–8 wt.%) is characterised by a minor increase or even stagnation of SiO_2 followed by a second interval (< 6 wt.% MgO) exhibiting a pronounced enrichment with progressive differentiation. The pronounced silica increase coincides with the onset of amphibole and/or magnetite crystallisation enriching residual melts in SiO_2. LLDs at 400, 600, and 800 MPa are almost identical and demonstrate a smooth transition between the two stages related to the stabilisation of amphibole between 1020 and 990 °C. At 200 MPa, the sharp increase in silica contents from 50 to 59 wt.% between 4 and 6 wt.% MgO coincides with magnetite saturation and a strong decrease in residual melt fraction due to extensive crystallisation of clinopyroxene and plagioclase. TiO_2 concentrations demonstrate bell-shaped evolution trends for all four series (Fig. 5b). During an initial differentiation stage (4–8 wt.% MgO), titanium behaves incompatible and is enriched in the residual liquid. The subsequent decrease initiating between 4–5 wt.% MgO results from the saturation of a Ti-bearing mineral phase, i.e. amphibole at 400–800 MPa and magnetite at 200 MPa. Similar to titanium, Al_2O_3 contents exhibit bell-shaped evolution trends with an initial increase, followed by a plateau and a final decrease (Fig. 5c). These trends are closely related to plagioclase saturation and, thus, pressure. This controlling effect of pressure on alumina contents is illustrated by the experiments at 800 and 200 MPa, where a decrease of maximum Al_2O_3 contents can be identified with decreasing pressure. Furthermore, at 200 MPa, alumina contents already start decreasing between 7–8 wt.% MgO, in line with

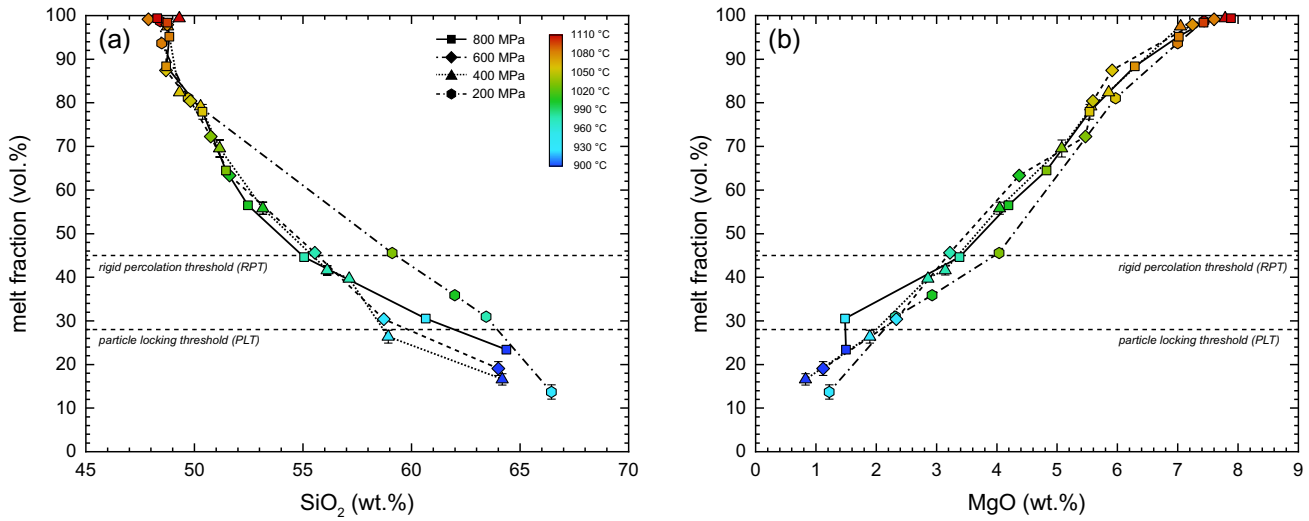

Fig. 4 Residual melt fractions in vol.% as a function of melt SiO_2 (**a**) and MgO (**b**) contents (in wt.%). In case error bars are not shown, their extent is smaller than the symbol size. Symbols are colour-coded with respect to run temperatures of corresponding experiments. For rheological interpretation, the *rigid percolation threshold* (RPT) and *particle locking threshold* (PLT) are illustrated with dashed lines. For more information on the conversion of melt fractions established via mass balance in wt.% to vol.%, see text

early plagioclase saturation. The 400 and 600 MPa LLDs behave slightly counterintuitive as the 400 MPa runs plot at higher Al_2O_3 than the 600 MPa ones. One explanation for this apparent mismatch are the competing effects of water activity and pressure on plagioclase stability. A decrease of pressure enhances plagioclase stability (e.g. Feig et al. 2010; Blatter et al. 2013), whereas the concomitant increase of water activity due to lower maximum water solubility counteracts this effect (e.g. Sisson and Grove 1993; Almeev et al. 2012; Marxer et al. 2022). However, Al_2O_3 contents of the IHPV repetition experiments (FM201 and FM202) exhibit slightly lower concentrations than their piston cylinder counterparts (0.6 and 0.9 wt.%) and overlap with the 600 MPa differentiation trend. Thus, we conclude that small variations in pressure do not crucially affect phase equilibria at mid-crustal depths (i.e. pressures of 400–600 MPa).

FeO contents of residual liquids (Fig. 5d) are characterised by an initial stagnation followed by a pronounced decrease at lower MgO contents. At high MgO, some FeO scattering can be related to small extents of Fe-loss at high temperatures. At 200 MPa, the rapid depletion of FeO between 4.0 and 5.5 wt.% MgO results from early magnetite saturation. For the 400, 600, and 800 MPa series, the decrease in FeO initiating between 3 and 4 wt.% MgO is related to the extensive crystallisation of iron-rich mafic phases (e.g. amphibole and orthopyroxene). At 200–600 MPa, CaO contents exhibit an initial plateau at around 11.0 wt.% from 5.5 to 8.0 wt.% MgO, followed by a continuous decrease (Fig. 5e). This plateau corresponds to short intervals of olivine-only crystallisation exerting a minimal effect on calcium contents of residual melts. Upon further cooling, clinopyroxene and anorthite-rich plagioclase join the solid phase assemblage resulting in a continuous decrease of calcium. The 800 MPa LLD exhibits a slightly earlier depletion of CaO initiating at 7.0 wt.% MgO due to the earlier saturation of clinopyroxene at high pressures. The more pronounced depletion in CaO at MgO contents below 5.5 wt.% for the 200 MPa experiments is caused by the extensive crystallisation of plagioclase and clinopyroxene at low pressures when water-saturated conditions were reached between 1050 and 1020 °C.

Na_2O concentrations of residual melts (Fig. 5f) exhibit increasing trends with decreasing temperature. The reported large uncertainties are the result of relatively small residual melt pools and their rare occurrence allowing only few reliable EPMA analyses per experiment. As a consequence, we cannot rule out that reported melt composition potentially suffered from some alkali migration or signal contamination during analysis (e.g. run FM99). Alternatively, the formation of albite-rich plagioclase quench crystals in the low-temperature piston cylinder runs could have resulted in Na-depletion in small residual melt pools. At 400–800 MPa, LLDs demonstrate only weak enrichments in sodium, controlled by co-crystallisation of sodium-bearing amphibole and plagioclase (see also Ulmer et al. 2018). In contrast, the 200 MPa experiments exhibit a distinct enrichment in sodium from 1050 to 990 °C, which is related to the crystallisation of An-rich plagioclase, delayed saturation of amphibole, and the strong increase of crystallinity due to the attainment of water-saturated conditions (Fig. 3). The levelling off below 3 wt.% MgO is most likely related to the onset of amphibole crystallisation and the stabilisation of a more albite-rich component in plagioclase suppressing further Na_2O enrichment. Interestingly, the IHPV experiment FM202 at 400 MPa exhibits a distinctly higher sodium content than its piston cylinder equivalent (2.8 vs 2.2 wt.%) which most probably represents an analytical artefact. Further details on differences between IHPV and piston cylinder 400 MPa experiments are discussed in the Electronic Supplementary Material ESM4. K_2O contents of residual liquids exhibit a continuous increase with decreasing MgO exemplifying the near-perfect incompatible behaviour of potassium in calc-alkaline systems in the absence of biotite or potassic feldspar (Fig. 5g). Similar to Na_2O, this enrichment is of a larger extent at 200 MPa owing to the more pronounced increase in crystallinity. Trace amounts of biotite crystallisation at 930 °C do not exert a significant influence on melt potassium contents. Phosphorous concentrations of residual melts reveal a near-perfect incompatible behaviour with ongoing differentiation until apatite saturation is reached between 1.5 to 2.5 wt.% MgO resulting in a sharp decrease of P_2O_5 (Fig. 5h).

Discussion

Effect of pressure on phase equilibria and peritectic mineral reactions

The presented experimental data illustrate that pressure exerts an important control on phase equilibria affecting the stability fields of olivine, clinopyroxene, plagioclase, and amphibole (Fig. 2). In agreement with previous experimental studies on similar starting material compositions (e.g. Sisson and Grove 1993; Kawamoto 1996; Hamada and Fujii 2008; Blatter et al. 2013; Melekhova et al. 2015; Ulmer et al. 2018), olivine was the liquidus phase at all investigated pressures. We observe a narrow stability field for spinel group minerals, where hercynitic spinel was stable in a few runs (1020–1065 °C) at 800 MPa, and extensive magnetite crystallisation was only observed at 200 MPa from 1020 to 930 °C. In contrast, several previous studies (Kawamoto 1996; Blatter et al. 2013; Melekhova et al. 2015) report spinel saturation close to the liquidus and significant crystallisation with ongoing cooling with a progressive shift of compositions from hercynitic spinel to magnetite. The limited

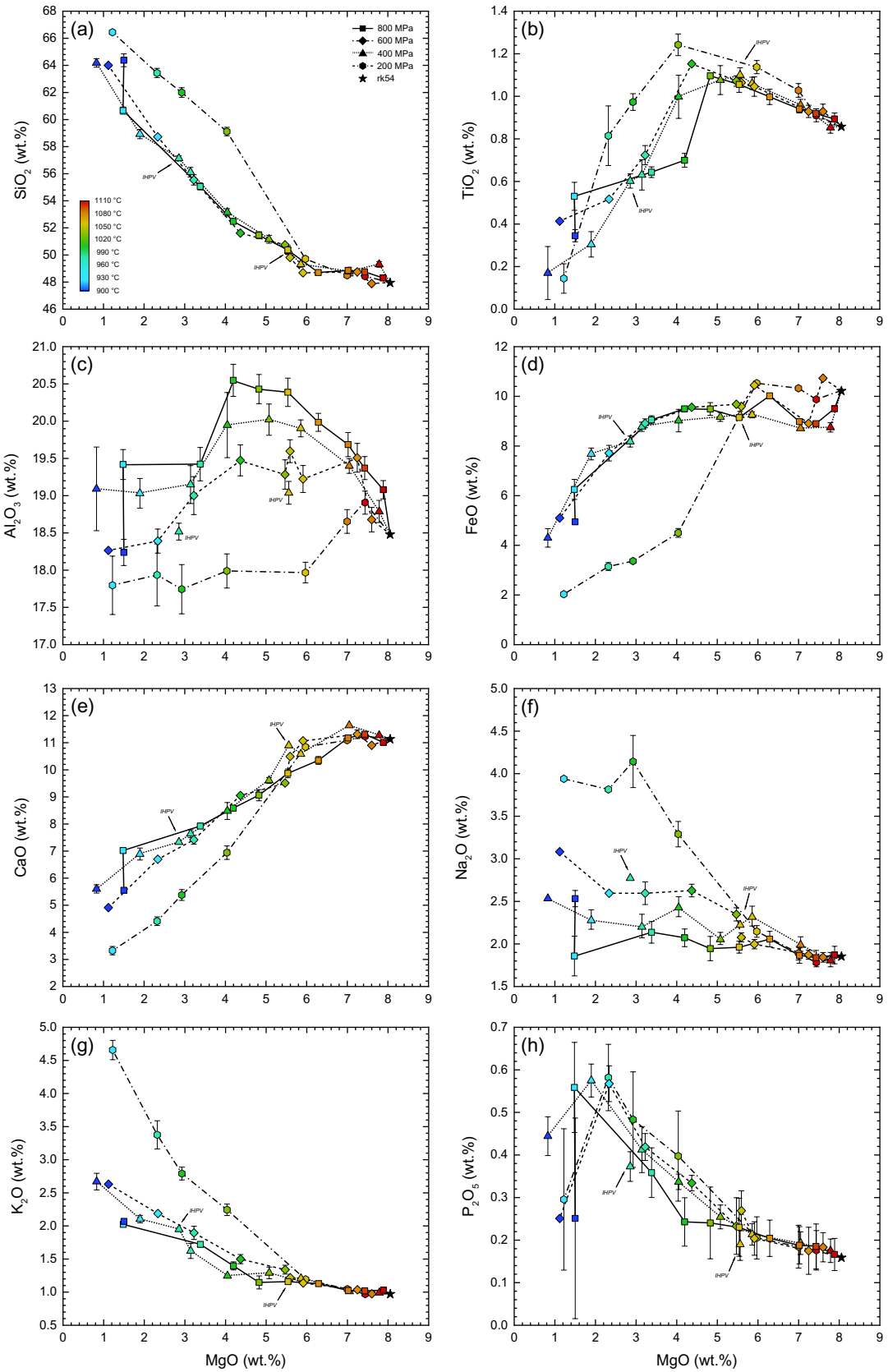
(a)
800 MPa
600 MPa
400 MPa
200 MPa
rk54
1110 °C
1080 °C
1050 °C
1020 °C
990 °C
960 °C
930 °C
900 °C
SiO2 (wt.%)
(b)
TiO2 (wt.%)
(c)
Al2O3 (wt.%)
(d)
FeO (wt.%)
(e)
CaO (wt.%)
(f)
Na2O (wt.%)
(g)
K2O (wt.%)
(h)
P2O5 (wt.%)
MgO (wt.%)
MgO (wt.%)
IHPV

◂ **Fig. 5** Major and minor oxide compositions of experimental liquids (in wt.%) recalculated on an anhydrous base as a function of MgO contents. In case error bars are not shown, their extent is smaller than the symbol size. The black star illustrates the initial starting material composition (rk54) and IHPV repetition runs at 400 MPa are explicitly labelled

occurrence and proportions of spinel in our experiments is related to (1) the absence of chromium in our synthetic starting material inhibiting the saturation of early-forming Cr-spinel and (2) the lower fO_2 of our runs (NNO-1 to NNO) compared to earlier studies (> NNO + 1).

At higher pressures (400–800 MPa), clinopyroxene joined olivine close to the liquidus consistent with previous studies. In contrast to our data, Sisson and Grove (1993), Melekhova et al. (2015), and Kawamoto (1996) observed the co-crystallisation of olivine + spinel + clinopyroxene + plagioclase directly at liquidus conditions. Here, plagioclase saturation was slightly delayed by ca. 30 °C to lower temperatures at high pressures (400–800 MPa) relative to the lower pressure series (200 MPa). This results in a crossover in plagioclase and clinopyroxene saturation curves emphasising the effect of pressure on the stability fields of these minerals. Our findings are consistent with previous studies describing a stabilisation of plagioclase at higher temperatures at low-pressure conditions (e.g. Sisson and Grove 1993; Kawamoto 1996; Hamada and Fujii 2008) compared to high-pressure series (e.g. Blatter et al. 2013; Melekhova et al. 2015). In the present study, orthopyroxene stabilises late in the crystallisation sequence. Interestingly, the orthopyroxene saturation curve exhibits a backbend towards lower temperatures at intermediate pressures (930 °C at 400 and 600 MPa, and 990 °C at 200 and 800 MPa) consistent with previous experimental studies (e.g. Blatter et al. 2013). Generally, orthopyroxene stability is strongly related to the activity of silica ($aSiO_2$) where increasing $aSiO_2$ favours the formation of orthopyroxene at the expense of olivine (e.g. Müntener et al. 2001). Consequently, the earlier saturation of orthopyroxene at 800 MPa can be explained with a decrease of aH_2O with increasing pressure causing $aSiO_2$ to increase. Likewise, the earlier appearance of orthopyroxene at 200 MPa could result from the coupled effects of water-saturation, high crystallisation rates, and enrichment of residual melts in SiO_2 (and $aSiO_2$), favouring the stabilisation of orthopyroxene. Alternatively, the backbend of orthopyroxene stability at intermediate pressures could also be related to a pressure-dependent change in the stoichiometry of the amphibole-forming peritectic reaction.

For amphibole, we observe an increase in thermal stability with increasing pressure (960 °C at 200 MPa to 990 °C at 800 MPa) in accordance with previous studies (e.g. Sisson and Grove 1993; Blatter et al. 2013). The onset of amphibole crystallisation represents a diverging peritectic point (Sisson and Grove 1993; Blatter et al. 2017; Ulmer et al. 2018) and the mineral assemblage involved in the peritectic reaction (and its stoichiometry) strongly depends on pressure. Based on experimental phase proportions, we reconstructed the qualitative stoichiometry of the amphibole forming reactions for all four investigated pressures. At 800 MPa, the onset of amphibole crystallisation can be described by the following reaction: liq + ol + cpx + plag + sp = amph ± opx. The role of orthopyroxene is difficult to assess as amphibole and orthopyroxene saturated simultaneously around 1000 °C. Orthopyroxene could also form via the peritectic reaction liq + ol = opx, but phase proportions suggest that orthopyroxene can only be involved on the product side of the amphibole-forming reaction. At intermediate pressures (400–600 MPa), the amphibole forming reaction is liq + ol + cpx ± sp = amph; i.e. plagioclase and orthopyroxene are not involved. At 200 MPa, amphibole formation does potentially not include olivine which is converted to orthopyroxene by the peritectic reaction liq + ol = opx. Consequently, the amphibole forming reaction is expressed as liq + cpx + mt = amph ± opx. At 400–800 MPa, phase proportions indicate that additional amphibole crystallisation beyond the diverging peritectic point involves residual liquid and mafic mineral phases (olivine, clinopyroxene, and orthopyroxene). In detail, at 800 MPa, amphibole progressively crystallises at the expense of clinopyroxene (liq + cpx = amph), while at 400–600 MPa olivine (and at lower temperatures orthopyroxene) is additionally involved (i.e. liq + cpx + ol/opx = amph). These reactions are in agreement with textural observations from natural rocks, e.g. in amphibole-bearing cumulates from the Bonanza arc in Canada (Larocque and Canil 2010) or the Chelan Complex in the Western U.S. (Dessimoz et al. 2012).

Liquid lines of descent (LLD): a comparison between isobaric equilibrium and polybaric fractional crystallisation

In Fig. 6, liquid lines of descent of the four isobaric equilibrium crystallisation series are compared with the polybaric fractional crystallisation experiments of Marxer et al. (2022) and a compilation of bulk rocks from the Cascades volcanoes (Western U.S.). Equilibrium crystallisation LLDs are illustrated with solid paths while polybaric fractional crystallisation trends from Marxer et al. (2022) are highlighted with dotted lines. In case, individual experimental series exhibited similar evolution trends they have been summarised and labelled accordingly. Marxer et al. (2022) performed a set of polybaric fractional crystallisation series along different magma ascent trajectories, where decompression-dominated P–T paths (simulating cooling rates of ca. 20–30 °C/100 MPa) are termed "hot", "RRO", and "interm"

Table 3 Averaged compositions of experimental phases determined by EPMA (in wt.%). Residual melts have been renormalised to an anhydrous base

Run	T (°C)	Phase[a]	#[b]	SiO_2	TiO_2	Al_2O_3	FeO	MnO	MgO	CaO	Na_2O	K_2O	P_2O_5	Total[c]	Endmembers[d]
800 MPa															
FM40	1110	Melt	*22*	48.3 (2)	0.89 (3)	19.1 (1)	9.50 (10)	0.27 (3)	7.89 (7)	11.0 (1)	1.87 (10)	1.03 (3)	0.17 (4)	93.5	
		Ol	*18*	39.8 (1)	0.05 (1)	0.08 (2)	16.5 (3)	0.34 (2)	44.0 (3)	0.24 (2)	0.005 (7)	0.01 (1)	0.01 (1)	101.0	Fo_{83}
FM85	1095	Melt	*12*	48.8 (2)	0.92 (2)	19.4 (2)	8.90 (12)	0.27 (3)	7.43 (8)	11.3 (1)	1.84 (9)	1.02 (5)	0.19 (5)	93.7	
		Ol	*17*	39.4 (2)	0.07 (1)	0.03 (2)	16.4 (2)	0.36 (2)	44.6 (3)	0.22 (1)	0.01 (2)	0.003 (5)	0.01 (1)	101.2	Fo_{83}
FM81	1080	Melt	*15*	48.9 (2)	0.94 (2)	19.7 (2)	8.98 (12)	0.26 (2)	7.02 (7)	11.2 (1)	1.86 (9)	1.03 (4)	0.19 (4)	93.9	
		Ol	*16*	39.5 (2)	0.07 (2)	0.04 (3)	17.0 (2)	0.37 (1)	44.1 (3)	0.26 (3)	0.01 (2)	0.01 (1)	0.01 (1)	101.4	Fo_{82}
		Cpx	*14*	50.0 (3)	0.55 (3)	6.96 (27)	5.55 (17)	0.22 (2)	15.4 (2)	21.0 (3)	0.24 (2)	0.02 (2)	0.02 (2)	100.0	$En_{46}Fs_9Wo_{45}$
FM78	1065	Melt	*11*	48.7 (1)	1.00 (4)	20.0 (1)	10.0 (1)	0.27 (3)	6.29 (9)	10.3 (1)	2.06 (9)	1.13 (3)	0.20 (4)	93.5	
		Ol	*17*	38.8 (2)	0.10 (2)	0.04 (3)	20.9 (1)	0.41 (2)	40.4 (1)	0.24 (2)	0.02 (2)	0.01 (1)	0.004 (9)	100.9	Fo_{77}
		Cpx	*15*	49.0 (5)	0.68 (4)	7.89 (53)	6.94 (46)	0.27 (3)	14.8 (2)	20.0 (4)	0.27 (2)	0.02 (1)	0.01 (1)	100.0	$En_{45}Fs_{12}Wo_{43}$
		Sp	*8*	0.17 (7)	0.25 (2)	61.9 (3)	18.1 (2)	0.19 (1)	17.0 (1)	0.16 (3)	0.02 (1)	0.01 (1)	0.02 (1)	97.8	
FM90	1050	Melt	*10*	50.4 (3)	1.06 (4)	20.4 (2)	9.14 (11)	0.28 (2)	5.54 (9)	9.87 (16)	1.96 (7)	1.16 (4)	0.23 (7)	93.5	
		Ol	*21*	40.0 (2)	0.08 (1)	0.04 (2)	20.3 (3)	0.43 (2)	41.1 (3)	0.25 (2)	0.01 (1)	0.01 (1)	0.01 (1)	101.2	Fo_{78}
		Cpx	*21*	48.7 (4)	0.75 (14)	8.40 (28)	6.44 (49)	0.25 (3)	14.7 (3)	20.8 (6)	0.25 (4)	0.03 (3)	0.01 (1)	100.4	$En_{44}Fs_{11}Wo_{45}$
		Plag	*23*	44.7 (3)	0.08 (1)	35.3 (3)	0.49 (7)	0.02 (2)	0.07 (2)	18.2 (2)	1.05 (11)	0.06 (1)	0.01 (2)	99.9	$An_{90}Ab_9Or_0$
		Sp	*8*	0.10 (3)	0.23 (2)	63.4 (4)	17.7 (3)	0.21 (1)	18.3 (3)	0.12 (2)	0.01 (2)	0.01 (1)	0.01 (1)	100.1	
FM104	1020	Melt	*4*	51.5 (3)	1.10 (1)	20.4 (2)	9.49 (26)	0.30 (5)	4.83 (38)	9.06 (21)	1.95 (14)	1.15 (10)	0.24 (8)	91.6	
		Ol	*23*	38.5 (3)	0.09 (2)	0.04 (3)	24.3 (4)	0.50 (2)	37.6 (3)	0.24 (2)	0.01 (1)	0.004 (5)	0.02 (2)	101.4	Fo_{73}
		Cpx	*20*	48.8 (5)	0.91 (9)	8.12 (68)	7.95 (34)	0.33 (10)	14.0 (3)	19.9 (4)	0.30 (4)	0.02 (1)	0.01 (1)	100.3	$En_{43}Fs_{14}Wo_{44}$
		Plag	*15*	46.0 (5)	0.10 (2)	34.4 (4)	0.57 (3)	0.02 (2)	0.09 (3)	17.4 (4)	1.34 (23)	0.08 (2)	0.02 (2)	100.0	$An_{87}Ab_{12}Or_0$
		Sp	*3*	0.82 (8)	0.32 (1)	60.3 (1)	19.8 (2)	0.22 (1)	15.6 (2)	0.24 (7)	0.07 (4)	0.03 (1)	0.01 (1)	97.5	
FM94	990	Melt	*7*	52.5 (1)	0.70 (3)	20.5 (2)	9.50 (10)	0.29 (6)	4.20 (11)	8.59 (10)	2.07 (10)	1.40 (6)	0.24 (6)	91.1	
		Cpx	*7*	49.3 (3)	0.53 (6)	6.67 (26)	9.71 (45)	0.40 (5)	14.2 (5)	18.9 (6)	0.24 (2)	0.02 (1)	0.01 (1)	100.0	$En_{43}Fs_{16}Wo_{41}$
		Plag	*21*	45.1 (6)	0.08 (2)	35.3 (4)	0.59 (5)	0.03 (2)	0.07 (3)	17.8 (5)	1.21 (25)	0.07 (2)	0.02 (2)	100.2	$An_{89}Ab_{11}Or_0$
		Amph	*21*	41.0 (2)	1.62 (22)	16.2 (4)	11.0 (4)	0.24 (2)	13.7 (2)	10.8 (2)	1.90 (5)	0.87 (5)	0.02 (2)	97.4	
		Opx	*21*	49.7 (5)	0.27 (2)	7.61 (71)	16.7 (3)	0.51 (3)	23.7 (4)	1.69 (28)	0.03 (2)	0.01 (1)	0.01 (1)	100.2	$En_{69}Fs_{27}Wo_4$
FM96	960	Melt	*4*	55.1 (3)	0.64 (3)	19.4 (2)	9.05 (16)	0.30 (5)	3.38 (5)	7.92 (10)	2.14 (13)	1.72 (2)	0.36 (6)	90.2	
		Cpx	*7*	49.6 (4)	0.46 (4)	5.62 (60)	10.9 (4)	0.42 (4)	13.7 (6)	19.1 (6)	0.24 (3)	0.03 (2)	0.02 (2)	100.0	$En_{41}Fs_{18}Wo_{41}$
		Plag	*16*	45.4 (5)	0.07 (2)	35.0 (5)	0.61 (6)	0.03 (2)	0.07 (1)	17.6 (5)	1.37 (27)	0.08 (2)	0.02 (2)	100.2	$An_{87}Ab_{12}Or_0$
		Amph	*24*	41.6 (6)	1.52 (17)	15.5 (5)	12.0 (6)	0.26 (2)	13.2 (4)	10.8 (3)	1.85 (7)	0.85 (5)	0.02 (2)	97.6	
		Opx	*12*	50.0 (5)	0.23 (2)	6.23 (79)	19.7 (3)	0.63 (03)	21.7 (4)	1.82 (25)	0.03 (3)	0.01 (2)	0.02 (2)	100.4	$En_{64}Fs_{32}Wo_4$
FM99	930	Melt	*2*	60.7 (3)	0.53 (7)	19.4 (2)	6.25 (40)	0.20 (4)	1.48 (2)	7.02 (1)	1.86 (23)	2.02 (3)	0.56 (11)	88.0	
		Cpx	*10*	50.3 (3)	0.41 (5)	4.91 (40)	11.9 (4)	0.54 (3)	13.0 (3)	18.7 (4)	0.23 (4)	0.04 (3)	0.03 (2)	100.1	$En_{39}Fs_{20}Wo_{41}$
		Plag	*14*	46.2 (5)	0.10 (2)	34.4 (4)	0.62 (4)	0.03 (2)	0.06 (3)	17.3 (5)	1.40 (18)	0.08 (2)	0.04 (3)	100.2	$An_{87}Ab_{13}Or_1$
		Amph	*19*	42.7 (4)	1.35 (17)	14.7 (5)	13.3 (2)	0.31 (2)	12.5 (2)	10.6 (3)	1.74 (7)	0.78 (4)	0.03 (2)	98.1	
		Opx	*13*	50.7 (3)	0.22 (2)	4.70 (42)	21.5 (5)	0.79 (4)	20.7 (44)	1.75 (28)	0.03 (3)	0.01 (1)	0.01 (1)	100.4	$En_{61}Fs_{35}Wo_4$

Table 3 (continued)

Run	T (°C)	Phase[a]	#[b]	SiO_2	TiO_2	Al_2O_3	FeO	MnO	MgO	CaO	Na_2O	K_2O	P_2O_5	Total[c]	Endmembers[d]
FM107	900	Melt	*2*	64.4 (5)	0.34 (3)	18.2 (2)	4.95 (7)	0.19 (3)	1.50 (4)	5.55 (11)	2.53 (10)	2.07 (5)	0.25 (24)	88.4	
		Cpx	*4*	50.9 (2)	0.31 (10)	3.51 (46)	11.3 (4)	1.09 (91)	12.9 (6)	19.8 (6)	0.26 (8)	0.03 (2)	0.03 (2)	100.1	$En_{39}Fs_{19}Wo_{43}$
		Plag	*16*	47.3 (11)	0.10 (2)	33.4 (7)	0.57 (9)	0.02 (1)	0.05 (2)	16.2 (8)	1.92 (39)	0.09 (4)	0.02 (2)	99.7	$An_{82}Ab_{18}Or_1$
		Amph	*31*	42.2 (5)	1.21 (16)	14.0 (6)	14.0 (4)	0.35 (4)	12.3 (3)	10.4 (4)	1.64 (9)	0.71 (5)	0.03 (2)	96.8	
		Opx	*12*	50.7 (3)	0.21 (2)	3.91 (73)	21.3 (8)	0.86 (7)	21.5 (6)	1.29 (24)	0.03 (2)	0.02 (2)	0.01(1)	100.0	$En_{63}Fs_{35}Wo_3$
		Ap	*1*	0.61	0.13	0.08	0.92	0.19	0.26	53.8	b.d.[e]	0.05	39.7	95.8	
600 MPa															
FM75	1080	Melt	*11*	47.9 (1)	0.93 (4)	18.7 (2)	10.7 (1)	0.27 (3)	7.60 (6)	10.9 (1)	1.84 (6)	0.98 (3)	0.18 (3)	93.2	
		Ol	*15*	39.6 (1)	0.09 (2)	0.03 (3)	17.1 (1)	0.35 (2)	43.4 (2)	0.23 (2)	0.01 (2)	0.01 (1)	0.02 (2)	100.8	Fo_{82}
FM49	1065	Melt	*6*	48.8 (1)	0.93 (3)	19.5 (2)	8.91 (16)	0.25 (1)	7.25 (6)	11.3 (2)	1.87 (5)	1.04 (4)	0.17 (6)	93.1	
		Ol	*20*	40.1 (1)	0.08 (1)	0.04 (3)	16.5 (3)	0.35 (2)	43.7 (3)	0.26 (2)	0.01 (2)	0.003 (5)	0.01 (1)	101.1	Fo_{82}
FM73	1050	Melt	*14*	48.7 (2)	1.05 (5)	19.2 (2)	10.4 (1)	0.28 (2)	5.91 (9)	11.1 (1)	2.00 (5)	1.14 (4)	0.20 (4)	93.7	
		Ol	*13*	39.0 (2)	0.09 (1)	0.05 (2)	20.6 (1)	0.43 (1)	40.5 (2)	0.28 (2)	0.02 (2)	0.01 (1)	0.01 (1)	101.0	Fo_{78}
		Cpx	*6*	49.3 (3)	0.73 (7)	6.58 (30)	6.67 (12)	0.22 (2)	14.4 (1)	21.6 (2)	0.22 (3)	0.02 (1)	0.002 (4)	99.8	$En_{43}Fs_{11}Wo_{46}$
		Plag	*17*	44.7 (3)	0.09 (2)	34.9 (2)	0.69 (7)	0.01 (1)	0.08 (2)	18.5 (2)	0.87 (11)	0.06 (2)	0.01 (1)	100.0	$An_{92}Ab_8Or_0$
FM86	1035	Melt	*5*	49.8 (3)	1.06 (2)	19.6 (2)	9.59 (9)	0.28 (2)	5.59 (4)	10.5 (1)	2.08 (5)	1.22 (4)	0.27 (5)	92.7	
		Ol	*25*	38.9 (1)	0.08 (1)	0.05 (2)	20.5 (2)	0.45 (1)	40.4 (2)	0.27 (2)	0.01 (1)	0.01 (1)	0.01 (1)	100.7	Fo_{78}
		Cpx	*18*	49.2 (3)	0.80 (8)	6.77 (34)	6.51 (36)	0.24 (3)	14.7 (3)	21.7 (5)	0.22 (3)	0.03 (1)	0.02 (2)	100.2	$En_{43}Fs_{11}Wo_{46}$
		Plag	*15*	44.8 (5)	0.09 (1)	35.2 (4)	0.60 (4)	0.01 (1)	0.08 (2)	18.3 (3)	1.02 (20)	0.07 (2)	0.02 (2)	100.2	$An_{90}Ab_9Or_0$
FM95	1020	Melt	*10*	50.7 (3)	1.07 (2)	19.3 (2)	9.68 (15)	0.31 (4)	5.47 (16)	9.51 (14)	2.35 (8)	1.34 (7)	0.23 (7)	93.1	
		Ol	*24*	38.9 (2)	0.08 (1)	0.04 (2)	20.7 (4)	0.50 (2)	40.7 (3)	0.28 (2)	0.02 (3)	0.01 (1)	0.01 (1)	101.2	Fo_{78}
		Cpx	*14*	48.8 (4)	0.82 (7)	6.87 (41)	7.35 (39)	0.26 (2)	14.2 (2)	21.2 (3)	0.26 (3)	0.02 (1)	0.01 (1)	99.8	$En_{42}Fs_{12}Wo_{45}$
		Plag	*21*	45.0 (6)	0.07 (2)	35.1 (3)	0.69 (9)	0.02 (2)	0.07 (2)	17.8 (4)	1.23 (21)	0.08 (2)	0.01 (2)	100.1	$An_{88}Ab_{11}Or_0$
		Sp	*5*	0.10 (2)	3.73 (7)	15.4 (3)	69.0 (3)	0.41 (2)	7.19 (18)	0.15 (4)	0.03 (4)	0.01 (1)	0.01 (1)	96.0	
FM87	990	Melt	*3*	51.6 (1)	1.15 (2)	19.5 (2)	9.56 (15)	0.32 (1)	4.37 (2)	9.05 (13)	2.63 (7)	1.50 (7)	0.33 (2)	91.6	
		Ol	*23*	38.0 (1)	0.09 (1)	0.04 (2)	25.6 (2)	0.58 (2)	36.5 (2)	0.27 (2)	0.01 (1)	0.005 (6)	0.02 (2)	101.2	Fo_{72}
		Cpx	*15*	48.3 (4)	1.08 (10)	7.13 (42)	8.15 (34)	0.28 (2)	13.5 (2)	21.3 (4)	0.28 (4)	0.03 (2)	0.01 (2)	100.1	$En_{41}Fs_{14}Wo_{46}$
		Plag	*16*	45.0 (6)	0.08 (2)	35.0 (4)	0.66 (5)	0.01 (1)	0.08 (3)	17.8 (5)	1.24 (28)	0.08 (3)	0.01 (2)	100.0	$An_{88}Ab_{11}Or_0$
		Amph	*28*	40.2 (2)	2.70 (12)	15.4 (2)	10.5 (2)	0.20 (2)	13.8 (2)	11.8 (1)	2.07 (5)	0.96 (3)	0.02 (1)	97.7	
FM97	960	Melt	*3*	55.5 (4)	0.72 (5)	19.0 (3)	8.91 (18)	0.27 (2)	3.22 (13)	7.42 (17)	2.60 (13)	1.90 (10)	0.42 (3)	90.9	
		Ol	*20*	37.1 (2)	0.09 (2)	0.03 (2)	31.4 (2)	0.75 (2)	32.2 (2)	0.26 (2)	0.02 (2)	0.01 (1)	0.02 (2)	101.9	Fo_{65}
		Cpx	*12*	49.6 (2)	0.64 (7)	5.37 (22)	9.69 (31)	0.39 (3)	13.9 (3)	20.0 (3)	0.24 (4)	0.04 (3)	0.01 (2)	99.9	$En_{41}Fs_{16}Wo_{43}$
		Plag	*9*	45.6 (6)	0.08 (3)	35.0 (3)	0.67 (7)	0.02 (2)	0.06 (2)	17.6 (3)	1.35 (23)	0.08 (2)	0.02 (2)	100.5	$An_{87}Ab_{12}Or_0$
		Amph	*19*	40.9 (6)	2.60 (48)	14.8 (4)	11.6 (5)	0.24 (2)	13.3 (2)	11.3 (2)	1.97 (8)	0.94 (6)	0.03 (2)	97.6	
FM100	930	Melt	*2*	58.7 (3)	0.52 (2)	18.4 (2)	7.71 (32)	0.28 (1)	2.33 (4)	6.70 (5)	2.60 (4)	2.19 (3)	0.57 (4)	91.9	
		Cpx	*9*	50.5 (4)	0.44 (9)	4.24 (58)	11.6 (7)	0.51 (9)	12.9 (3)	19.5 (9)	0.23 (4)	0.05 (2)	0.03 (2)	100.0	$En_{39}Fs_{20}Wo_{42}$

Table 3 (continued)

Run	T (°C)	Phase[a]	#[b]	SiO_2	TiO_2	Al_2O_3	FeO	MnO	MgO	CaO	Na_2O	K_2O	P_2O_5	Total[c]	Endmembers[d]
		Plag	*10*	46.5 (6)	0.10 (2)	34.3 (4)	0.68 (8)	0.02 (1)	0.06 (2)	17.0 (5)	1.54 (22)	0.08 (3)	0.02 (2)	100.3	$An_{85}Ab_{14}Or_1$
		Amph high Ti	*11*	41.9 (4)	2.38 (25)	14.5 (4)	12.2 (4)	0.29 (3)	13.1 (2)	11.0 (4)	1.92 (7)	0.83 (6)	0.02 (1)	98.1	
		Amph low Ti	*13*	42.4 (2)	1.26 (21)	14.1 (3)	13.6 (5)	0.31 (1)	12.9 (2)	10.7 (1)	1.84 (6)	0.80 (4)	0.03 (2)	98.0	
		Opx	*17*	51.0 (5)	0.21 (3)	4.19 (69)	21.6 (5)	0.76 (3)	20.9 (5)	2.01 (48)	0.03 (3)	0.01 (1)	0.02 (2)	100.7	$En_{61}Fs_{35}Wo_4$
FM108	900	Melt	*1*	64.0	0.41	18.3	5.10	0.23	1.12	4.91	3.08	2.63	0.25	90.8	
		Cpx	*8*	51.0 (4)	0.28 (7)	3.62 (29)	12.8 (9)	0.56 (9)	11.7 (10)	20.2 (8)	0.25 (4)	0.02 (1)	0.01 (1)	100.4	$En_{35}Fs_{22}Wo_{44}$
		Plag	*20*	47.1 (7)	0.09 (1)	33.6 (5)	0.65 (7)	0.02 (1)	0.05 (2)	16.3 (5)	2.02 (24)	0.13 (4)	0.02 (1)	100.0	$An_{81}Ab_{18}Or_1$
		Amph high Ti	*3*	42.8 (2)	2.21 (14)	12.9 (3)	13.4 (2)	0.36 (3)	12.6 (3)	10.6 (6)	1.78 (11)	0.65 (3)	0.03 (2)	97.2	
		Amph low Ti	*9*	42.8 (3)	0.96 (15)	13.2 (5)	14.4 (6)	0.34 (3)	12.1 (3)	10.5 (3)	1.64 (5)	0.76 (4)	0.04 (1)	96.7	
		Opx	*18*	50.4 (5)	0.18 (4)	3.85 (55)	22.9 (6)	0.93 (6)	19.4 (4)	1.76 (27)	0.03 (3)	0.01 (2)	0.01 (2)	99.5	$En_{58}Fs_{38}Wo_4$
		Ap	*5*	1.28 (29)	0.001 (2)	0.31 (11)	0.93 (4)	0.16 (1)	0.26 (4)	53.2 (3)	0.06 (1)	0.09 (2)	40.4 (8)	96.7	
400 MPa															
FM137	1110	Melt	*8*	49.3 (2)	0.85 (3)	18.8 (1)	8.75 (19)	0.27 (2)	7.79 (11)	11.3 (1)	1.81 (8)	0.99 (3)	0.17 (3)	94.2	
		Ol	*6*	40.0 (3)	0.01 (2)	0.05 (3)	15.7 (5)	0.35 (2)	43.3 (4)	0.29 (5)	0.01 (1)	0.01 (1)	0.01 (1)	99.8	Fo_{83}
FM133	1080	Melt	*12*	48.8 (3)	0.96 (3)	19.4 (1)	8.71 (11)	0.28 (3)	7.05 (6)	11.6 (1)	1.99 (9)	1.01 (2)	0.19 (3)	93.2	
		Ol	*19*	39.5 (3)	0.01 (1)	0.04 (1)	16.9 (3)	0.38 (1)	42.5 (4)	0.25 (3)	0.01 (1)	0.005 (6)	0.01 (1)	99.6	Fo_{82}
FM130	1050	Melt	*16*	49.3 (2)	1.06 (3)	19.9 (1)	9.26 (12)	0.29 (2)	5.86 (10)	10.6 (1)	2.32 (12)	1.21 (4)	0.21 (3)	92.4	
		Ol	*17*	38.7 (1)	0.01 (1)	0.03 (1)	20.7 (2)	0.44 (2)	39.1 (2)	0.27 (2)	0.01 (1)	0.01 (0)	0.01 (1)	99.3	Fo_{77}
		Cpx high Al	*15*	49.1 (7)	0.81 (14)	8.67 (77)	6.85 (31)	0.27 (2)	14.0 (4)	20.1 (6)	0.25 (3)	0.01 (1)	0.01 (1)	100.1	$En_{43}Fs_{12}Wo_{45}$
		Cpx low Al	*2*	51.1 (4)	0.55 (2)	6.16 (35)	6.25 (3)	0.26 (1)	15.0 (2)	20.7 (5)	0.25 (3)	0.02 (0)	0.01 (0)	100.3	$En_{45}Fs_{11}Wo_{45}$
		Plag	*19*	45.4 (5)	0.09 (2)	35.0 (4)	0.59 (5)	0.02 (2)	0.12 (2)	17.7 (4)	1.25 (24)	0.09 (2)	0.01 (1)	100.4	$An_{88}Ab_{11}Or_1$
FM201	1050	Melt	*33*	50.3 (2)	1.10 (3)	19.0 (2)	9.24 (16)	0.27 (2)	5.56 (6)	10.9 (1)	2.22 (4)	1.20 (3)	0.19 (4)	93.6	
		Ol	*35*	38.2 (2)	0.03 (1)	0.05 (2)	21.7 (3)	0.52 (4)	39.6 (3)	0.31 (4)	0.002 (4)	0.01 (1)	n.a.[f]	100.1	Fo_{77}
		Cpx high Al	*19*	50.9 (8)	0.56 (12)	4.52 (92)	7.00 (61)	0.29 (5)	14.8 (4)	21.7 (5)	0.23 (3)	0.04 (2)	n.a.[f]	100.0	$En_{43}Fs_{11}Wo_{45}$
		Cpx low Al	*11*	51.1 (4)	0.31 (7)	2.39 (3)	7.85 (77)	0.34 (7)	15.5 (6)	21.1 (7)	0.22 (5)	0.03 (1)	n.a.[f]	99.9	$En_{44}Fs_{13}Wo_{43}$
		Plag	*27*	45.3 (4)	0.04 (1)	35.0 (4)	0.74 (9)	0.02 (1)	0.11 (2)	18.6 (3)	0.94 (18)	0.06 (2)	n.a.[f]	100.7	$An_{91}Ab_8Or_0$
FM155	1020	Melt	*15*	51.2 (3)	1.08 (7)	20.0 (2)	9.17 (18)	0.29 (5)	5.08 (17)	9.61 (11)	2.05 (7)	1.29 (9)	0.25 (3)	92.6	
		Ol	*27*	38.2 (2)	0.01 (1)	0.03 (1)	23.4 (4)	0.49 (2)	37.2 (4)	0.25 (2)	0.003 (6)	0.01 (1)	0.01 (1)	99.6	Fo_{74}
		Cpx	*23*	49.5 (4)	0.91 (8)	7.55 (35)	7.39 (21)	0.28 (2)	13.7 (2)	20.8 (3)	0.27 (3)	0.02 (1)	0.01 (1)	100.4	$En_{42}Fs_{13}Wo_{46}$
		Plag	*23*	46.1 (4)	0.03 (2)	34.8 (3)	0.55 (5)	0.02 (1)	0.08 (2)	17.9 (3)	1.23 (15)	0.08 (2)	0.01 (1)	100.8	$An_{89}Ab_{11}Or_0$
FM158	990	Melt	*2*	53.2 (3)	1.00 (10)	19.9 (4)	9.02 (45)	0.34 (7)	4.05 (13)	8.48 (31)	2.43 (12)	1.25 (2)	0.34 (2)	90.4	
		Ol	*30*	37.8 (2)	0.01 (1)	0.02 (1)	26.8 (2)	0.59 (2)	34.2 (3)	0.25 (2)	0.004 (8)	0.004 (4)	0.01 (1)	99.7	Fo_{69}
		Cpx	*23*	48.7 (4)	1.10 (10)	7.05 (32)	8.17 (22)	0.30 (5)	13.1 (2)	20.8 (3)	0.28 (2)	0.02 (1)	0.01 (1)	99.5	$En_{40}Fs_{14}Wo_{46}$
		Plag	*24*	46.4 (5)	0.02 (2)	34.9 (4)	0.59 (6)	0.02 (2)	0.07 (3)	17.7 (5)	1.26 (22)	0.08 (2)	0.01 (1)	101.1	$An_{88}Ab_{11}Or_0$
		Amph	*23*	40.9 (3)	2.51 (9)	15.3 (2)	9.98 (14)	0.21 (2)	13.7 (1)	11.3 (1)	2.12 (5)	0.97 (4)	0.01 (1)	97.0	
FM161	960	Melt	*13*	56.1 (4)	0.63 (7)	19.1 (3)	8.78 (19)	0.31 (5)	3.14 (16)	7.64 (14)	2.20 (14)	1.62 (11)	0.41 (5)	91.1	

Table 3 (continued)

Run	T (°C)	Phase[a]	#[b]	SiO_2	TiO_2	Al_2O_3	FeO	MnO	MgO	CaO	Na_2O	K_2O	P_2O_5	Total[c]	Endmembers[d]
		Ol	*30*	37.0 (1)	0.01 (1)	0.02 (1)	30.4 (2)	0.72 (2)	31.0 (2)	0.24 (2)	0.005 (8)	0.01 (0)	0.02 (1)	99.5	Fo_{65}
		Cpx	*23*	50.7 (5)	0.62 (10)	4.96 (62)	9.30 (33)	0.39 (4)	13.5 (5)	20.1 (4)	0.27 (7)	0.03 (1)	0.01 (1)	100.0	$En_{41}Fs_{16}Wo_{44}$
		Plag	*26*	46.7 (4)	0.02 (2)	34.6 (4)	0.59 (8)	0.02 (1)	0.07 (3)	17.6 (4)	1.34 (19)	0.08 (2)	0.01 (1)	101.0	$An_{87}Ab_{12}Or_0$
		Amph	*29*	41.7 (3)	2.25 (13)	14.1 (3)	11.6 (3)	0.25 (2)	13.0 (3)	11.2 (2)	2.02 (5)	0.91 (4)	0.02 (1)	97.1	
FM202	960	Melt	*3*	57.1 (2)	0.60 (3)	18.5 (1)	8.18 (22)	0.29 (2)	2.86 (9)	7.33 (5)	2.77 (3)	1.95 (3)	0.37 (3)	91.5	
		Ol	*32*	36.1 (2)	0.03 (1)	0.04 (2)	32.6 (4)	0.89 (4)	30.4 (3)	0.27 (3)	0.002 (4)	0.01 (1)	n.a.[f]	100.4	Fo_{62}
		Cpx high Al	*12*	50.4 (5)	0.54 (11)	3.83 (6)	10.6 (7)	0.45 (8)	13.5 (7)	20.2 (8)	0.25 (2)	0.04 (2)	n.a.[f]	99.8	$En_{40}Fs_{17}Wo_{43}$
		Cpx low Al	*13*	52.1 (5)	0.25 (9)	1.35 (54)	11.5 (16)	0.48 (14)	13.9 (6)	20.0 (13)	0.24 (4)	0.03 (1)	n.a.[f]	99.9	$En_{40}Fs_{19}Wo_{41}$
		Plag	*26*	46.0 (5)	0.02 (1)	34.5 (4)	0.71 (7)	0.02 (2)	0.06 (2)	17.9 (3)	1.29 (16)	0.07 (1)	n.a.[f]	100.6	$An_{88}Ab_{11}Or_0$
		Amph	*34*	41.6 (4)	2.07 (14)	13.5 (4)	13.0 (4)	0.29 (4)	13.0 (2)	11.3 (2)	2.15 (5)	0.81 (4)	n.a.[f]	97.8	
FM162	930	Melt	*8*	58.9 (3)	0.30 (6)	19.0 (2)	7.68 (24)	0.32 (3)	1.90 (26)	6.89 (22)	2.28 (11)	2.10 (6)	0.57 (4)	91.1	
		Cpx	*18*	51.5 (3)	0.35 (8)	3.91 (30)	10.9 (3)	0.50 (5)	13.3 (6)	19.5 (9)	0.22 (3)	0.05 (2)	0.02 (1)	100.3	$En_{40}Fs_{18}Wo_{42}$
		Plag	*30*	47.2 (7)	0.02 (2)	34.2 (4)	0.61 (7)	0.02 (1)	0.05 (3)	17.0 (5)	1.68 (24)	0.11 (2)	0.01 (1)	100.9	$An_{84}Ab_{15}Or_1$
		Amph high Ti	*17*	42.1 (3)	2.16 (17)	13.3 (3)	13.1 (2)	0.29 (2)	12.6 (2)	11.0 (2)	1.98 (5)	0.84 (4)	0.03 (2)	97.3	
		Amph low Ti	*14*	42.5 (2)	1.56 (13)	13.3 (2)	13.3 (3)	0.31 (1)	12.7 (2)	10.9 (1)	1.92 (4)	0.83 (4)	0.03 (1)	97.3	
		Opx	*26*	51.2 (6)	0.11 (2)	3.84 (80)	21.3 (5)	0.79 (2)	20.6 (5)	1.67 (21)	0.02 (1)	0.01 (1)	0.01 (1)	99.5	$En_{61}Fs_{35}Wo_4$
FM159	900	Melt	*4*	64.2 (3)	0.17 (12)	19.1 (6)	4.30 (37)	0.18 (8)	0.83 (23)	5.60 (15)	2.53 (18)	2.67 (13)	0.44 (5)	90.3	
		Plag	*24*	48.1 (6)	0.01 (2)	33.2 (5)	0.62 (7)	0.03 (1)	0.05 (3)	16.2 (5)	2.05 (26)	0.14 (3)	0.02 (1)	100.5	$An_{81}Ab_{18}Or_1$
		Amph high Ti	*20*	42.9 (4)	2.00 (24)	12.3 (7)	13.7 (4)	0.32 (3)	12.5 (2)	10.5 (3)	1.82 (8)	0.80 (8)	0.03 (1)	96.9	
		Amph low Ti	*9*	43.1 (2)	1.38 (11)	12.2 (4)	14.1 (2)	0.33 (3)	12.3 (2)	10.6 (2)	1.75 (5)	0.86 (7)	0.04 (1)	96.8	
		Opx	*25*	51.6 (3)	0.15 (4)	2.54 (47)	22.1 (5)	0.88 (5)	20.0 (3)	1.81 (25)	0.02 (1)	0.01 (1)	0.01 (1)	99.1	$En_{59}Fs_{37}Wo_4$
		Ap	*5*	0.48 (6)	b.d.[e]	0.04 (1)	0.92 (3)	0.14 (3)	0.25 (2)	53.2 (4)	0.02 (2)	0.04 (1)	42.2 (5)	97.3	
200 MPa															
FM117	1110	Melt	*15*	48.4 (3)	0.91 (3)	18.9 (2)	9.88 (13)	0.27 (3)	7.44 (11)	11.2 (1)	1.78 (5)	0.97 (3)	0.18 (5)	94.5	
		Ol	*23*	40.3 (2)	0.07 (1)	0.03 (2)	14.6 (5)	0.37 (2)	45.5 (4)	0.30 (2)	0.01 (2)	0.005 (5)	0.01 (1)	101.1	Fo_{85}
FM109	1080	Melt	*18*	48.5 (2)	1.03 (3)	18.7 (2)	10.3 (1)	0.29 (3)	7.00 (9)	11.1 (1)	1.89 (8)	1.04 (5)	0.18 (5)	94.4	
		Ol	*29*	40.0 (1)	0.07 (1)	0.04 (3)	15.6 (3)	0.39 (2)	44.7 (2)	0.29 (2)	0.01 (2)	0.00 (1)	0.01 (1)	101.1	Fo_{84}
		Plag	*13*	45.3 (3)	0.08 (2)	34.5 (1)	0.77 (10)	0.01 (1)	0.12 (3)	18.1 (2)	0.95 (4)	0.05 (1)	0.02 (3)	99.9	$An_{91}Ab_9Or_0$
FM110	1080	Melt	*17*	49.7 (2)	1.14 (3)	18.0 (1)	10.5 (1)	0.30 (2)	5.97 (6)	10.8 (1)	2.15 (7)	1.19 (3)	0.21 (5)	94.1	
		Ol	*28*	39.5 (1)	0.08 (1)	0.03 (2)	18.7 (4)	0.48 (2)	42.1 (4)	0.33 (3)	0.02 (2)	0.004 (7)	0.02 (1)	101.3	Fo_{80}
		Plag	*16*	45.4 (4)	0.09 (2)	34.4 (3)	0.78 (6)	0.02 (1)	0.11 (3)	17.8 (3)	1.10 (16)	0.08 (2)	0.01 (2)	99.8	$An_{90}Ab_{10}Or_0$
FM120	1020	Melt	*10*	59.1 (3)	1.24 (5)	18.0 (2)	4.50 (18)	0.24 (5)	4.04 (14)	6.94 (25)	3.29 (15)	2.24 (9)	0.40 (11)	92.3	
		Ol rims	*26*	40.3 (3)	0.09 (1)	0.03 (1)	13.6 (12)	0.69 (2)	44.5 (10)	0.31 (2)	0.01 (1)	0.01 (1)	0.01 (1)	99.6	Fo_{85}
		Ol cores	*3*	39.9 (2)	0.09 (2)	0.02 (1)	16.5 (4)	0.69 (2)	42.1 (4)	0.33 (1)	0.01 (0)	0.01 (1)	0.01 (1)	99.6	Fo_{82}
		Plag	*22*	46.3 (7)	0.10 (2)	34.2 (5)	0.71 (8)	0.02 (1)	0.08 (1)	17.1 (6)	1.58 (30)	0.09 (2)	0.01 (1)	100.2	$An_{85}Ab_{14}Or_1$
		Cpx	*26*	51.4 (7)	0.77 (14)	3.92 (71)	7.87 (58)	0.30 (5)	14.1 (6)	21.7 (3)	0.24 (6)	0.03 (1)	0.01 (1)	100.3	$En_{41}Fs_{13}Wo_{46}$

Table 3 (continued)

Run	T (°C)	Phase[a]	#[b]	SiO_2	TiO_2	Al_2O_3	FeO	MnO	MgO	CaO	Na_2O	K_2O	P_2O_5	Total[c]	Endmembers[d]
		Mt	*29*	0.09 (2)	2.80 (21)	6.13 (15)	73.4 (4)	0.85 (2)	9.29 (37)	0.16 (3)	0.01 (1)	0.004 (5)	0.005 (6)	92.7	
FM122	990	Melt	*6*	62.0 (4)	0.97 (4)	17.7 (3)	3.37 (13)	0.20 (2)	2.93 (12)	5.38 (20)	4.14 (31)	2.79 (10)	0.48 (11)	92.8	
		Ol rims	*22*	40.7 (2)	0.09 (1)	0.04 (6)	11.3 (10)	0.76 (2)	46.2 (9)	0.29 (4)	0.01 (1)	0.01 (1)	0.02 (1)	99.4	Fo_{88}
		Ol cores	*2*	40.1 (1)	0.11 (1)	0.02 (0)	14.0 (1)	0.78 (1)	44.1 (0)	0.30 (1)	0.01 (1)	0.01 (1)	0.02 (1)	99.4	Fo_{85}
		Plag	*27*	47.7 (7)	0.10 (2)	33.4 (5)	0.60 (6)	0.02 (1)	0.07 (3)	16.2 (5)	2.09 (27)	0.13 (4)	0.01 (1)	100.3	$An_{81}Ab_{19}Or_1$
		Cpx	*21*	51.3 (5)	0.97 (16)	3.50 (59)	8.31 (41)	0.34 (3)	13.8 (3)	21.5 (3)	0.24 (4)	0.02 (1)	0.01 (1)	99.9	$En_{41}Fs_{14}Wo_{46}$
		Mt	*26*	0.09 (2)	2.67 (31)	5.58 (19)	73.2 (3)	0.97 (3)	9.04 (47)	0.20 (4)	0.005 (10)	0.01 (1)	0.004 (6)	91.8	
		Opx	*17*	54.1 (5)	0.36 (6)	4.22 (67)	7.27 (34)	0.70 (3)	31.6 (4)	1.51 (22)	0.03 (2)	0.01 (1)	0.02 (1)	99.9	$En_{86}Fs_{11}Wo_3$
FM114	960	Melt	*4*	63.4 (3)	0.81 (14)	17.9 (4)	3.15 (16)	0.16 (3)	2.32 (4)	4.41 (16)	3.82 (27)	3.38 (21)	0.58 (8)	92.6	
		Ol rims	*17*	40.5 (3)	0.10 (1)	0.04 (2)	12.6 (11)	0.81 (2)	45.4 (9)	0.27 (2)	0.002 (5)	0.01 (1)	0.03 (1)	99.8	Fo_{86}
		Ol cores	*2*	40.2 (1)	0.09 (3)	0.03 (1)	14.9 (1)	0.85 (2)	43.5 (0)	0.27 (1)	0.01 (0)	0.01 (0)	0.03 (1)	99.8	Fo_{84}
		Plag	*17*	48.2 (12)	0.12 (3)	33.0 (9)	0.78 (14)	0.03 (1)	0.13 (9)	15.8 (9)	2.17 (46)	0.20 (11)	0.03 (2)	100.4	$An_{79}Ab_{20}Or_1$
		Cpx	*12*	51.3 (5)	0.80 (19)	3.00 (68)	8.91 (75)	0.40 (4)	13.8 (6)	21.0 (5)	0.34 (13)	0.04 (3)	0.02 (1)	99.6	$En_{41}Fs_{15}Wo_{45}$
		Mt low Ti	*30*	0.10 (4)	2.36 (35)	5.03 (9)	75.8 (4)	0.92 (4)	8.10 (40)	0.24 (5)	0.01 (1)	0.01 (1)	0.01 (1)	92.6	
		Mt high Ti	*3*	0.08 (2)	18.8 (6)	1.21 (2)	67.1 (12)	0.29 (1)	3.82 (13)	0.32 (1)	b.d.[e]	0.01 (1)	0.01 (0)	91.7	
		Opx	*20*	53.6 (4)	0.44 (5)	4.16 (40)	8.41 (45)	0.77 (4)	31.0 (6)	1.38 (28)	0.03 (3)	0.01 (3)	0.05 (3)	99.8	
		Amph rims	*5*	42.7 (6)	2.95 (10)	12.1 (11)	8.23 (22)	0.30 (2)	15.8 (6)	11.8 (6)	2.10 (8)	0.69 (6)	0.09 (3)	96.7	$En_{84}Fs_{13}Wo_3$
		Amph cores	*5*	40.9 (7)	4.01 (24)	12.7 (3)	11.8 (4)	0.25 (1)	12.7 (4)	11.5 (1)	2.15 (2)	0.94 (7)	0.04 (2)	97.1	
FM118	930	Melt	*2*	66.4 (1)	0.14 (7)	17.8 (4)	2.03 (5)	0.14 (1)	1.22 (4)	3.33 (15)	3.94 (12)	4.66 (15)	0.30 (17)	92.0	
		Plag	*3*	51.0 (3)	0.11 (2)	31.1 (1)	0.65 (9)	0.01 (1)	0.07 (4)	13.4 (2)	3.61 (20)	0.25 (3)	0.004 (6)	100.2	$An_{66}Ab_{32}Or_1$
		Cpx	*12*	51.9 (4)	0.56 (8)	3.15 (72)	9.61 (88)	0.43 (6)	13.4 (5)	20.5 (4)	0.38 (13)	0.05 (3)	0.02 (1)	100.0	$En_{40}Fs_{16}Wo_{44}$
		Mt high Ti	*1*	0.09	17.3	1.01	67.2	0.41	4.62	0.21	0.02	0.02	0.01	90.9	
		Mt mid Ti	*18*	0.08 (2)	10.7 (19)	1.17 (7)	74.8 (24)	0.28 (5)	2.80 (60)	0.25 (6)	0.01 (1)	0.01 (1)	0.01 (1)	90.2	
		Mt low Ti	*1*	0.10	4.73	1.53	81.0	0.19	1.45	0.18	b.d.[e]	0.01	b.d.[e]	89.2	
		Opx high Fe	*24*	53.9 (5)	0.28 (4)	2.69 (45)	13.3 (6)	0.87 (4)	27.1 (6)	1.41 (17)	0.03 (2)	0.02 (3)	0.01 (1)	99.6	$En_{76}Fs_{21}Wo_3$
		Opx low Fe	*8*	54.7 (6)	0.26 (5)	2.92 (67)	10.9 (7)	0.84 (4)	28.7 (8)	1.55 (31)	0.05 (3)	0.03 (4)	0.02 (2)	100.0	$En_{80}Fs_{17}Wo_3$
		Amph rims	*26*	43.6 (4)	2.38 (21)	11.2 (3)	8.95 (63)	0.29 (2)	16.1 (5)	11.4 (2)	2.17 (6)	0.80 (3)	0.06 (2)	97.0	
		Amph cores	*30*	43.0 (4)	2.86 (23)	11.4 (3)	11.0 (7)	0.31 (2)	14.3 (7)	11.1 (1)	2.13 (7)	0.82 (4)	0.06 (2)	97.0	
		Bt	*7*	38.9 (6)	4.59 (37)	15.8 (2)	6.94 (16)	0.13 (3)	19.8 (2)	0.34 (17)	0.89 (5)	9.18 (8)	0.01 (1)	96.6	
		Ap	*2*	1.01 (17)	b.d.[e]	0.15 (7)	0.47 (12)	0.15 (1)	0.56 (0)	53.0 (3)	0.07 (2)	0.07 (2)	40.3 (2)	95.8	

Abbreviations for mineral phases: *Ol* olivine, *Cpx* clinopyroxene, *Plag* plagioclase, *Sp* hercynitic spinel, *Amph* amphibole, *Mt* magnetite, *Opx* orthopyroxene, *Ap* apatite, *Bt* biotite

[a]In some runs, chemical zonation was identified for various mineral phases (clinopyroxene, orthopyroxene, amphibole, and olivine) and separate compositional averages for different zones are reported herein. For more details, see text

[b]Number of individual analyses averaged for reported phase composition

[c]For residual melts, non-renormalised EPMA totals are reported

[d]For pyroxenes, calculated endmembers are: enstatite (En), ferrosilite (Fs), and wollastonite (Wo), for plagioclase: anorthite (An), albite (Ab), and orthoclase (Or), and for olivine: forsterite (Fo)

[e]Element was below the EPMA detection limit (b.d.)

[f]Element was not analysed (n.a.)

and more cooling-controlled ascent paths (corresponding to 45 °C/100 MPa) are illustrated by the "cold" series. For the "RRO" series, fO_2 was buffered close to the Re-ReO_2 equilibrium (RRO), while the other paths were buffered at NNO, i.e. at identical conditions as the isobaric equilibrium crystallisation experiments presented in this study.

TiO_2 contents of residual liquids are strongly related to the crystallisation of amphibole and/or Fe-Ti-oxides where the saturation of these phases results in a depletion of residual liquids in TiO_2 (Fig. 6a). Closer inspection of the experimental data reveals that individual LLDs exhibit similar evolution trends but differ in maximum enrichment levels and SiO_2 contents at the onset of the decreasing trend, where equilibrium crystallisation generally results in a more pronounced depletion of TiO_2, while polybaric fractional crystallisation LLDs (Marxer et al. 2022) fit better the natural data. In detail, high-pressure EC LLDs (400–800 MPa) only show a minor initial enrichment and generally underestimate the TiO_2 contents of the natural rocks due to extensive amphibole crystallisation. On the contrary, the 200 MPa EC series initially overestimates natural titanium levels and only exhibits a late-stage depletion at SiO_2 contents above 60 wt.% (caused by magnetite saturation) resulting in a steeper decrease with respect to the Cascades. In contrast, the polybaric fractionation experiments principally reach higher maximum TiO_2 contents compared to the equilibrium crystallisation series due to limited amphibole formation because of the suppression of peritectic reactions. However, differentiated residual liquids are comparable to the isobaric EC data where the more decompression-dominated ascent trajectories (FC hot and FC interm) approach the high-pressure EC data while the cooling-dominated path (FC cold) exhibits a pronounced depletion similar to the 200 MPa EC data.

Al_2O_3 contents of the Cascades volcanics exhibit a broad bell-shaped pattern characterised by a weak initial increase or stagnation at values around 16–19 wt.% followed by a continuous depletion for SiO_2 contents exceeding 65 wt.% (Fig. 6b). As discussed earlier, our equilibrium crystallisation LLDs display a distinct effect of pressure on alumina characteristics. At low SiO_2 (50–55 wt.%), high-pressure EC trajectories (400–800 MPa) overestimate natural Al_2O_3 contents. Upon progressive differentiation (SiO_2 contents of 55–65 wt.%) the mid-crustal 400 and 600 MPa EC trends approach the latter, while the 800 MPa series evolves along the upper compositional range of the Cascades rocks. On the contrary, the 200 MPa EC series closely reproduces the Cascades volcanics from 50 to 65 wt.% SiO_2 but evolve towards higher Al_2O_3 contents with progressive differentiation. The polybaric fractional crystallisation series (Marxer et al. 2022) exhibit evolution trajectories very similar to the EC experiments. The decompression-dominated trends (FC hot, FC RRO, and FC interm) agree best with the natural rock record and closely overlap with the 400–600 MPa EC LLDs. In contrast, similar to the 800 MPa EC trend, the cooling-dominated polybaric fractionation path overestimates Al_2O_3 contents with progressive differentiation (especially between 60 and 65 wt.%) due to extensive initial high-pressure (cpx-dominated) fractionation (see also Blatter et al. 2013; Nandedkar et al. 2014; Ulmer et al. 2018).

FeO concentrations of experimental liquids exhibit some spread but generally follow decreasing trajectories similar to the natural data (Fig. 6c). At intermediate SiO_2 (50–60 wt.%), the high-pressure EC series (400–800 MPa) plot at higher FeO contents than the Cascades but approach the upper compositional field of the latter upon progressive differentiation (60–65 wt.% SiO_2). In contrast, the 200 MPa EC series (as well as the polybaric FC RRO path) exhibits a strong depletion in iron resulting in distinctly lower FeO concentrations relative to the natural rock record. This discrepancy can be related to differences in fO_2 between our experiments and the natural system. Most of the explored experimental series (400–800 MPa EC and FC hot, FC interm, FC cold) had oxygen fugacity buffered at moderately oxidising conditions close to NNO (effective fO_2 varying between NNO-1 to NNO) delaying the saturation of Fe-Ti-oxides and, thus, the depletion of residual liquids in iron. In contrast, the fO_2 conditions of the 200 MPa EC and the FC RRO series were more oxidising (NNO + 1 to RRO) causing early and extensive Fe-Ti-oxide saturation depleting residual liquids efficiently in FeO. As the natural data are plotting between these two groups of experimental trajectories, we infer that the Cascades magmas most probably differentiated at fO_2 conditions around NNO to NNO + 1, in accordance with estimates of typical arc magma redox conditions (e.g. Carmichael 1991; Cottrell et al. 2021). This conclusion is further supported by TiO_2 characteristics, where natural data likewise plot between these two groups of experimental trajectories (Fig. 6a), as well as FeO_{tot}/MgO evolution trends (Fig. 7a).

With the exception of the 200 MPa EC series, the high-pressure equilibrium crystallisation LLDs (400–800 MPa EC) underestimate MgO contents compared to the natural rock record (Fig. 6d). For the polybaric fractionation series (Marxer et al. 2022), the underestimation is even more pronounced (e.g. FC interm and FC cold) which can be explained by the continuous removal of mafic, MgO-rich minerals. However, during equilibrium crystallisation in a closed system this effect is less distinct, but the enhanced formation of mafic minerals (olivine, pyroxene, and amphibole) potentially caused a significant depletion of residual liquids in MgO compared to the Cascades volcanics. The higher MgO contents observed for the 200 MPa EC series are the result of extensive plagioclase and suppressed mafic mineral crystallisation. This crucial effect of low-pressure phase relations on MgO is further illustrated by the shift of the decompression-driven polybaric FC trajectories (FC

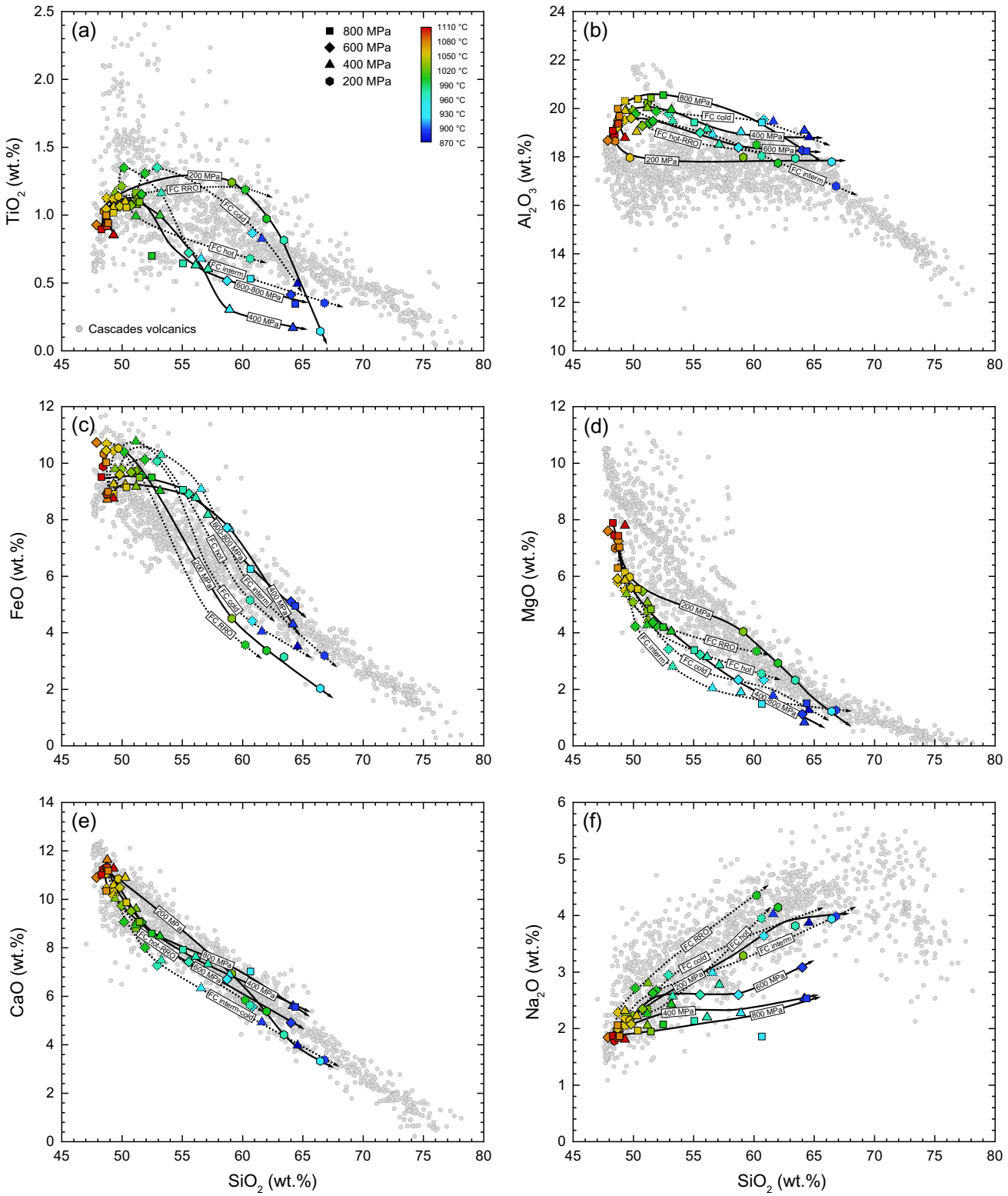

Fig. 6 Oxide vs SiO_2 diagrams (in wt.%) comparing the equilibrium crystallisation (EC) LLDs of this study with the polybaric fractionation (FC) experiments by Marxer et al. (2022) as well as a bulk rock compilation for the Cascades volcanics (Western U.S.) compiled by J. Blundy (for detailed references, see ESM4). Polybaric fractionation experiments are indicated with stippled symbol strokes and trajectories and individual P–T paths are labelled after Marxer et al. (2022). Equilibrium crystallisation experiments are labelled according to pressure (200–800 MPa). Note that for some oxide compounds, overlapping evolution trends of individual series have been merged (e.g. 400–800 MPa for MgO)

hot, FC RRO, FC interm) towards the natural compositional field upon the last fractionation step (corresponding to a final decompression to 200 MPa, see Marxer et al. (2022) for details).

CaO contents of equilibrium crystallisation residual liquids follow the natural rock record and exhibit a near-linear decrease with differentiation matching the continuous crystallisation of clinopyroxene and plagioclase (Fig. 6e). The 200 MPa EC series exhibits the best match with the Cascades between 50 and 60 wt.% SiO_2 but tends to underestimate CaO contents at more evolved compositions, likely the result of extensive plagioclase and clinopyroxene crystallisation at low pressures. Although evolving initially along the lower spectrum of natural CaO concentrations (50 to 55 wt.% SiO_2), the 400–800 MPa EC LLDs reproduce best the latter at $SiO_2 > 55$ wt.%. The polybaric fractionation LLDs (Marxer et al. 2022) exhibit a slightly higher degree of CaO depletion with respect to the EC series because of the continuous removal of Ca-bearing phases (clinopyroxene and An-rich plagioclase).

Similar to the natural data, equilibrium crystallisation LLDs reveal some spread in terms of Na_2O evolution with generally increasing contents upon differentiation (Fig. 6f). However, while the 200 MPa EC series reproduces the lower range of natural Na_2O contents, the high-pressure EC trajectories (400–800 MPa) significantly underestimate the latter. The degree of sodium enrichment decreases with increasing pressure. This is due to increasing proportions of Na-bearing amphibole crystallisation at high pressures inhibiting a strong enrichment of residual liquids in sodium. In addition, primitive magmas from the Cascades have generally slightly higher Na_2O contents than our starting material (Ulmer et al. 2018) further explaining why our EC experiments tend to underestimate the Cascades Na_2O trend. The polybaric fractionation series (Marxer et al. 2022) generally reach higher Na_2O contents than the isobaric equilibrium crystallisation series providing a better fit to the Cascades trend.

The evolution of the FeO_{tot}/MgO ratio versus SiO_2 is illustrated in Fig. 7a. High-pressure EC series (400–800 MPa) fail to reproduce the Cascades trend and rather define an arc tholeiitic differentiation trend. Interestingly, the 800 MPa EC series reveals a shift towards calc-alkaline compositions at low temperatures what is not observed for the mid-pressure EC trajectories (400–600 MPa). In contrast, the 200 MPa EC LLD enters the calc-alkaline field relatively early but underestimate the FeO_{tot}/MgO contents of the natural rocks. Similarly, the polybaric FC experiments of Marxer et al. (2022) also show an initial arc tholeiitic differentiation trend and a subsequent shift into the calc-alkaline field. This distinct mismatch between natural data and experimental liquids is related to the strong effect of fO_2 on the stability field of Fe-Ti-oxides (e.g. Sisson and Grove 1993; Sisson et al. 2005), where Fe-Ti oxide saturation causes a deflection of differentiation trends from the tholeiitic into the calc-alkaline field. Our data clearly support this conclusion; the 400–800 MPa EC series do not saturate in Fe-Ti-oxides and indeed define arc tholeiitic differentiation trends. As the equilibrium and polybaric fractional crystallisation LLDs, where fO_2 was buffered between NNO-1 and NNO (400–800 MPa EC, FC hot, FC interm, FC cold), remain tholeiitic upon differentiation and the LLDs at more oxidising conditions (NNO + 1 to RRO) (200 MPa EC and FC RRO) reveal a too strong

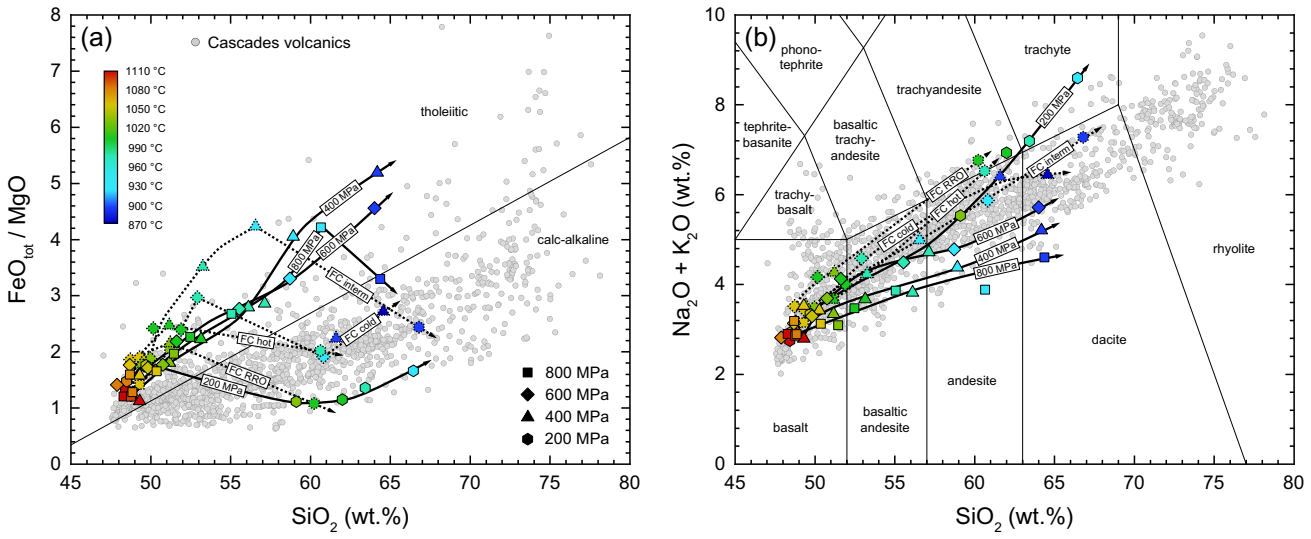

Fig. 7 FeO_{tot}/MgO (**a**) and total alkalis ($Na_2O + K_2O$) (**b**) plotted against SiO_2 (in wt.%) comparing EC and FC liquid lines of descent with bulk rock data from the Cascades. The discrimination line between tholeiitic and calc-alkaline compositions on the left panel is based on Miyashiro (1974), while compositional fields in the TAS diagram are drawn after Le Bas et al. (1986)

depletion in FeO_{tot}/MgO, we conclude that the Cascades volcanics must have differentiated at fO_2 between NNO and NNO + 1 (as further supported by FeO and TiO_2 characteristics in Figs. 6a and c), consistent with the established range of typical arc magmatic fO_2 conditions (e.g. Carmichael 1991; Cottrell et al. 2021).

Total alkali contents ($Na_2O + K_2O$) of experimental liquids increase with increasing SiO_2, consistent with the natural evolution trend (Fig. 7b). The high-pressure EC series (400–800 MPa) define differentiation trajectories evolving along the lower limit of the natural data, while the 200 MPa EC LLD exhibits a more pronounced enrichment in alkalis reproducing natural rocks, but even evolves towards weakly alkaline compositions entering the trachyandesitic or trachytic field. The polybaric fractional crystallisation LLDs (Marxer et al. 2022) define more pronounced enrichments in alkalis compared to the equilibrium crystallisation series and reproduce the Cascades compositional spread. However, strongly decompression-controlled paths (FC hot and FC RRO) evolve to slightly alkaline trachyandesitic compositions plotting at the upper limit for the natural rocks.

In summary, equilibrium isobaric (this study) and polybaric fractional crystallisation (Marxer et al. 2022) LLDs reveal rather similar trajectories, where the latter tend to reproduce slightly better the natural compositional spread of arc magmas exemplified by the Cascades volcanics. However, the polybaric fractionation experiments display a more pronounced enrichment or depletion for several compounds (e.g. alkalis, CaO, or MgO) highlighting the higher efficiency of crystal fractionation during differentiation. Therefore, we conclude that crystallisation regimes in natural trans-crustal arc magmatic system represent a mixture between these two endmember processes. An additional process contributing to the compositional spread of natural volcanic arc rocks would be mixing of magmas of contrasting compositions resulting in near-linear compositional trajectories as illustrated, for example, by the flat Al_2O_3 pattern between 50 to 60 wt.% SiO_2 of the Cascades volcanics. In fact, as shown recently by Reubi and Müntener (2022), significant proportions of intermediate (60–65 wt.% SiO_2) arc volcanic rocks most likely represent the product of lower-crustal multistage mixing and/or mingling between mafic and derivative silicic liquids formed via high-pressure fractionation of the former. However, after mixing/mingling, resultant hybrid magmas must directly experience near-adiabatic decompression to shallow levels to maintain their chemical characteristics. Stalling at high pressures would result in a rapid back-shift to high-pressure LLDs due to phase equilibria control. Consequently, the chemical variability of natural arc magmas, as exemplified by the Cascades bulk rock compilation, does not represent one single differentiation trajectory but is rather the result of different polybaric differentiation trajectories characterised by various degrees of lower crustal fractionation accompanied by mingling and/or mixing and subsequent decompression-driven crystallisation of extracted residual liquids during near-adiabatic ascent.

Liquid lines of descent in pseudoternary projection

We illustrate the effect of pressure on arc magma differentiation and phase equilibria, in the olivine (Ol)—clinopyroxene (Cpx)—quartz plus orthoclase (Qtz + Or) normative pseudoternary diagram (Fig. 8). Residual liquids of the equilibrium crystallisation experiments exhibit a continuous decrease of normative clinopyroxene contents and an enrichment in quartz and orthoclase upon differentiation. LLDs are characterised by an initial, high temperature phase where normative clinopyroxene shows only limited variation but olivine decreases followed by clinopyroxene saturation driving residual liquids towards the Ol-(Qtz + Or) side-line. For the high-pressure EC series (400–800 MPa), a weak flattening upon crossing the metaluminous-peraluminous boundary (≈ Ol-Qtz + Or baseline) is related to the saturation of amphibole and orthopyroxene preventing a further strong

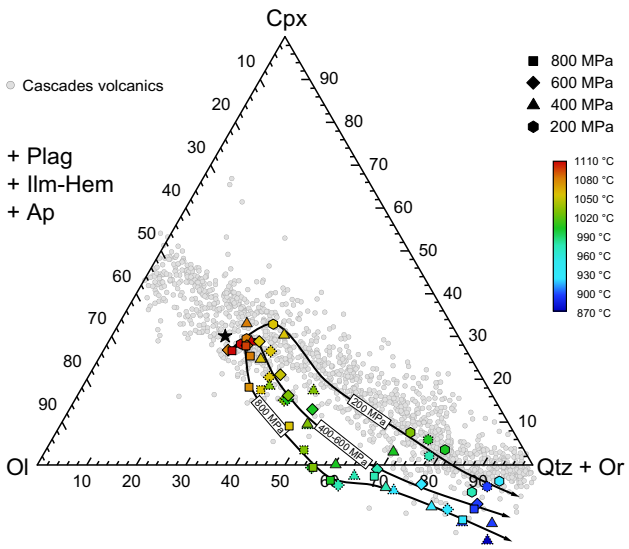

Fig. 8 Liquid lines of descent of fractional (FC) and equilibrium crystallisation (EC) series plotted in the normative olivine (Ol)—clinopyroxene (Cpx)—quartz plus orthoclase (Qtz + Or) pseudoternary diagram together with natural bulk rock compilations from the Cascades. Normative mineral endmembers were calculated following the approach of Grove et al. (1992). For recalculations, an Fe^{3+}/Fe_{tot} ratio of 0.20 was used for the experiments nominally buffered at NNO and 0.35 for RRO-buffered runs. For simplicity, if not provided otherwise, natural rock compositions from the Cascades were recalculated employing a ferric to total iron ratio of 0.20. In this ternary diagram, the clinopyroxene baseline (Ol-Qtz + Or) equals the boundary between peraluminous (ASI > 1) and metaluminous (ASI < 1) compositions, where negative normative clinopyroxene corresponds to peraluminous compositions. The black star corresponds to the starting material composition (rk54) used for this study

depletion of residual melts in normative clinopyroxene and causing a deflection towards the Qtz + Or corner.

The effect of pressure on phase equilibria is expressed as a progressive shift of EC LLDs towards higher normative clinopyroxene contents with decreasing pressure. This is consistent with a shift of the olivine-clinopyroxene cotectic curve upon decompression as suggested previously (e.g. Grove et al. 1992; Hamada and Fujii 2008; Stamper et al. 2014; Marxer et al. 2022). However, the 400 and 600 MPa EC differentiation trends overlap, likely a consequence of phase equilibria not being significantly affected by pressure changes in this intermediate mid-crustal pressure interval. The polybaric fractional crystallisation experiments of Marxer et al. (2022) exhibit a distinct overlap with the equilibrium crystallisation data of this study, with the fractionation experiments generally plotting on the isobaric equilibrium LLDs of their respective pressure. For example, the last decompression step experiments of the cold, interm, and RRO FC paths overlap perfectly with the 200 MPa EC differentiation trends (Fig. 8).

Comparing the experimental results with the compiled rock record from the Cascades reveals that the latter show a more linear evolution trajectory than the curved experimental ones. The natural data are generally well reproduced by the 200 MPa experiments, while the high-pressure liquids (400–800 MPa) plot at lower normative clinopyroxene except for evolved compositions close to the Qtz + Or corner. However, the 200 MPa EC experiments show a distinct jump in melt composition from 1050 to 1020 °C, thus, suppressing the voluminous formation of metaluminous basaltic-andesitic and andesitic natural rock compositions via low-pressure differentiation.

Cumulate lines of descent (CLD)

Experimental cumulate compositions were calculated for the equilibrium crystallisation series of this study as well as the polybaric fractional crystallisation experiments of Marxer et al. (2022) employing mineral phase proportions established via mass balance (Table 2) and chemical compositions of individual phases (Table 3). For the EC experiments, these correspond to the total solid compositions (TSC), while for the polybaric FC series, the instantaneous solid compositions (ISC), i.e. the cumulates crystallising during each fractionation step, were established. However, we infer that cumulates in arc systems are predominantly not pure adcumulates but rather meso- to orthocumulates (with up to 30 wt.% of retained interstitial liquid (e.g. Müntener and Ulmer 2018)) that formed by partial residual melt extraction from a cumulate/mush pile. Therefore, we additionally calculated bulk compositions of orthocumulates containing 30 wt.% of retained residual melt employing compositions of the liquid measured in the individual experiments for the EC experiments with sufficiently high residual melt fractions (i.e. > 30 wt.%) and the polybaric FC trajectories (Marxer et al. 2022). Calculated experimental cumulate compositions are reported in the Electronic Supplementary Material ESM7 and illustrated in Fig. 9. The results show a shift of cumulate compositions towards higher SiO_2 contents from adcumulates to orthocumulates while xMg, Al_2O_3, and CaO are less affected. Calculated experimental cumulate compositions are compared with plutonic rocks from the Adamello Batholith (Italy) and the Sierra Nevada (U.S.). To facilitate this comparison, compiled natural rocks from both settings are grouped in "liquid-like" and "cumulate-like" based on mineralogy and different geochemical criteria (e.g. alkali, MgO, Al_2O_3, or CaO contents): In detail, samples with reported mineralogy and rock names, have been assigned "cumulate-like" in case these match typical cumulate characteristics (e.g. anorthosite, troctolite, wherlite, pyroxenite, or hornblendite). Samples with less-characteristic mineralogy were classified as "cumulate-like" in case at least one of the following criteria was met: CaO > 12 wt.%, Al_2O_3 > 20 wt.%, MgO > 15 wt.%, SiO_2 < 46 wt.%, K_2O < 0.5 wt.%.

Calculated adcumulates of the isobaric equilibrium crystallisation series range from ultramafic dunites and wherlites to amphibole- or two-pyroxene gabbros. Cumulates formed during polybaric fractional crystallisation (Marxer et al. 2022) are broadly similar but show a larger variability and less regular trends than the EC CLDs due to the progressive change of phase equilibria during decompression (Fig. 9) and distinct differences between equilibrium and fractional crystallisation regimes with respect to the CLD.

For xMg (= MgO/(FeO_{tot} + MgO), molar ratio), z-shaped cumulate lines of descent can be identified for the EC and the polybaric FC experiments (Marxer et al. 2022), in accordance with Müntener and Ulmer (2018) (Fig. 9a). Since initial crystallisation is dominated by forsterite-rich olivine and increasing proportions of clinopyroxene causing an enrichment in cumulate SiO_2 contents at relatively constant xMg, early forming cumulates are dunites and wherlites. Upon saturation of anorthite-rich plagioclase, amphibole, and Fe-Ti-oxides, cumulates exhibit distinct decreases in xMg and SiO_2. The late-stage re-increase in SiO_2 is related to increasing proportions of more evolved mineral phases (e.g. plagioclase with higher albite contents). For the adcumulates formed during EC, CLDs can be distinguished in a high-pressure (high-P EC, 400–800 MPa) and a low-pressure (low-P EC, 200 MPa) trajectory. Consistent with the earlier onset of plagioclase crystallisation and delayed formation of clinopyroxene at low pressures, the low-P series exhibits an earlier decrease in xMg (at lower SiO_2) compared to the high-P trend due to the early saturation of Fe-Ti-oxides. The polybaric fractional crystallisation experiments (Marxer et al. 2022) exhibit a higher variability in xMg (and reach lower values) than the EC cumulates,

while both crystallisation regimes reveal a similar evolution in terms of SiO_2 contents. Low-temperature polybaric FC cumulates plot at lower xMg than the EC ones (between 0.3 and 0.4) and outside the field covered by natural rocks. With 30 wt.% of trapped residual melt, the difference between high-P and low-P equilibrium crystallisation CLDs vanishes resulting in a single EC CLD. Furthermore, the experimental CLDs (isobaric EC and polybaric FC) approach the natural rock record (i.e. are shifted to higher SiO_2 contents) and overlap with the most primitive cumulate rocks (Fig. 9b). The general mismatch between experimental adcumulates and natural rocks indicates that significant portions of residual liquid are trapped during cumulate solidification in nature inferring that complete extraction of residual liquid is not a likely scenario.

For Al_2O_3, isobaric equilibrium crystallisation CLDs exhibit an s-shaped pattern in accordance with findings of Müntener and Ulmer (2018) (Fig. 9c). However, cumulates formed during polybaric fractional crystallisation (Marxer et al. 2022) exhibit a larger compositional spread than the equilibrium crystallisation ones. The polybaric FC CLD is characterised by a counter-clockwise loop resulting from the early saturation of anorthite-rich plagioclase (increase of Al_2O_3 and decrease of SiO_2) and suppressed clinopyroxene crystallisation (decrease of SiO_2) due to progressive decompression. For both crystallisation regimes, initial high-T cumulates represent dunites which do not contain any alumina. Upon differentiation, the saturation of clinopyroxene and especially plagioclase result in a rapid enrichment in Al_2O_3 reaching maximum contents of 20 to 25 wt.%, broadly covering the entire range of Al_2O_3 contents of natural rocks. Adding up to 30 wt.% of trapped residual liquid shifts the experimental CLDs towards the natural rock record (Fig. 9d).

In SiO_2 vs CaO space (Fig. 9e), two different CLD patterns can be distinguished, namely a counter-clockwise evolution exhibited by the high-pressure (high-P EC, 400–800 MPa) equilibrium crystallisation series as well as the polybaric fractionation paths (polybaric FC, Marxer et al. 2022) and a s-shaped pattern shown by the low-pressure EC series (low-P EC, 200 MPa). Early cumulates represent dunites and are almost CaO free. At higher pressures (high-P EC, polybaric FC), the saturation of clinopyroxene causes an increase of CaO; a trend that is further enhanced by plagioclase saturation. However, with progressive differentiation, amphibole replaces clinopyroxene and plagioclase proportions increase, resulting in a weak decrease of CaO. With further crystallisation of more sodic plagioclase, CLD evolve towards lower CaO and higher SiO_2. Thereby, the polybaric FC cumulates from Marxer et al. (2022) exhibit a general larger compositional variability than the EC CLDs. The low-pressure EC trajectory is shifted to lower SiO_2 and CaO contents compared to the others (high-P EC and polybaric FC) due to early saturation of anorthite-rich plagioclase and magnetite and delayed clinopyroxene crystallisation. In either case, upon progressive differentiation both trajectories converge.

Effect of crystal fractionation on liquid lines of descent

Comparing the phase equilibria of this study with those from the polybaric fractional crystallisation experiments of Marxer et al. (2022), we identified two major differences: (1) Fractional crystallisation experiments are characterised by the absence of orthopyroxene and clinopyroxene in the presence of amphibole, while these three mineral phases coexist over significant temperature ranges in the equilibrium crystallisation series. The absence of pyroxenes in the presence of amphibole in the polybaric fractionation experiments (Marxer et al. 2022) is attributed to the suppression of the amphibole peritectic reaction during fractional crystallisation. Consequently, LLDs are not constrained to move along the branching peritectic reactions (i.e. cpx + liq = amph or opx + liq = amph) but instead directly evolve into the amphibole liquidus field resulting in amphibole-only parageneses. (2) Fe-Ti-oxides (magnetite and ilmenite) are prevalent in the polybaric fractionation series at temperatures below 1000 °C while Fe-Ti-oxide crystallisation was scarce during equilibrium crystallisation. The absence of Fe-Ti-oxides in the high-pressure EC runs is likely a consequence of amphibole-forming peritectic reactions. In addition, the EC series exhibit significantly higher proportions of amphibole and less clinopyroxene compared to the FC experiments again controlled by the progression of the amphibole peritectic reaction. Consequently, as discussed above, cumulates from fractional crystallisation exhibit a higher chemical diversity than those of equilibrium crystallisation (Fig. 9).

Despite these fundamental differences in phase equilibria and cumulate compositions, LLDs of isobaric equilibrium (this study) and polybaric fractional (Marxer et al. 2022) crystallisation exhibit very similar trajectories (compare Figs. 6, 7, 8). This indicates that chemical trends of residual melts in calc-alkaline magmatic system are strongly controlled by phase equilibria and the effects of suppressed peritectic reactions during fractional crystallisation on LLDs is limited.

Isothermal decompression-driven differentiation

Natural calc-alkaline rock compositions exhibit a distinct overlap with the 200 MPa experimental liquids for several chemical compounds (e.g. Al_2O_3, CaO, or Na_2O, Figs. 6, 7, 8) indicating that low-pressure crystallisation may be fundamental for arc magma differentiation. However, exposed lower crustal arc sections are dominated by voluminous

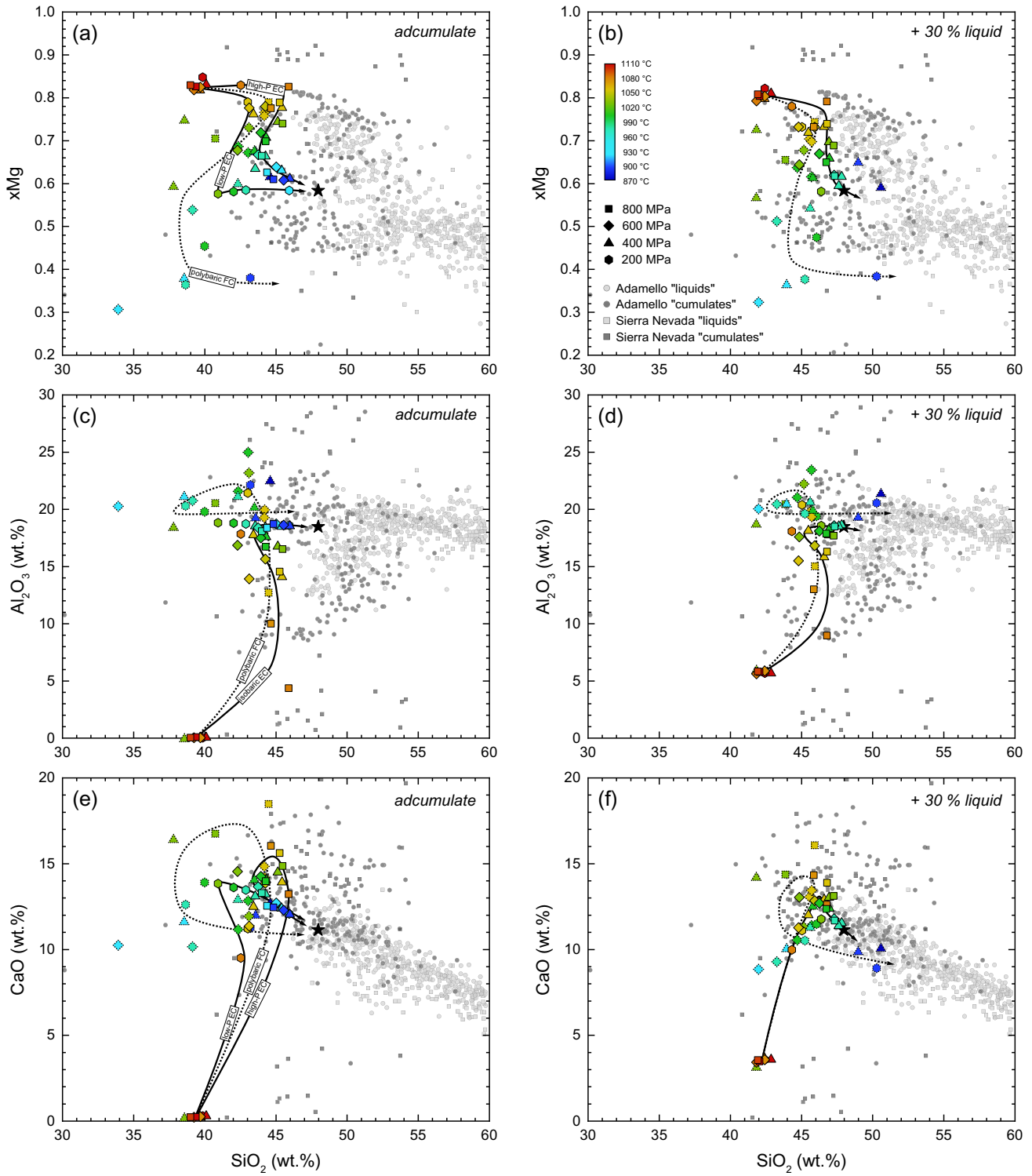

Fig. 9 Cumulate lines of descent (CLD) of EC and FC series compared with the natural rock record of the Adamello (Bianchi et al. 1970; Del Moro et al. 1983; Macera et al. 1983; Ulmer et al. 1983; Blundy and Sparks 1992; Verberne 2013; Hurlimann et al. 2016; P. Ulmer, unpublished data) and Sierra Nevada batholiths (data extracted from the GEOROC and EarthChem databases and filtered (Reubi and Müntener 2022)). Note that natural data are grouped in "cumulates" and "liquids" based on their compositions and mineralogy and that CLD trajectories of individual isobaric equilibrium (EC) and polybaric fractional crystallisation (FC) series are in most cases not distinguishable and have been summarised if appropriate. The black star corresponds to the starting material composition (rk54). **a** xMg (=molar ratio of MgO / (MgO+FeO) with all iron considered being ferrous) vs SiO_2; **c** evolution trends of Al_2O_3 with respect to silica; **e** CaO contents plotted against SiO_2; **b**,**d**,**f** orthocumulate CLDs for 30 wt.% of entrapped melt. For details on cumulate bulk composition calculations, see text

cumulates (e.g. Bard 1983; Greene et al. 2006; Jagoutz 2014) and geochemical data point to an important role of high-pressure amphibole fractionation (e.g. Romick et al. 1992; Davidson et al. 2007; Larocque and Canil 2010). Polybaric crystallisation-differentiation (e.g. Lewis et al. 2021; Marxer et al. 2022) or mixing between dry and wet melts (Rezeau et al. 2021) have recently been proposed to solve this issue. Here we further exploit the role of isothermal decompression on arc magma differentiation. Isothermal ascent trajectories represent a close approximation of crustal near-adiabatic (isentropic) ascent as the extent of cooling is minor for hydrous silicate liquids (15–50 °C/GPa) (e.g. Mastin and Ghiorso 2001; Carmichael 2002). Furthermore, latent heat release during decompression induced crystallisation (Blundy et al. 2006) could further promote near-isothermal magmatic rise. However, as damp to hydrous basalts (2–5 wt.% H_2O) only reach water-saturation at shallow/upper crustal levels, we infer that additional cooling due to volatile exsolution and expansion of existing vapour bubbles (e.g. Mastin and Ghiorso 2001; Glazner 2019) is only relevant for the late-stage magmatic rise to the surface but less so for a polybaric lower- to mid-crustal magmatic system.

Figure 10a illustrates decompression trajectories in a pressure (MPa) vs residual melt fraction (F, in wt.%) phase diagram. It is evident that melt fractions increase upon isothermal decompression from 800 to 600 MPa followed by a slight decrease to 400 MPa to initial levels. At high temperatures (> 1050 °C), decompression to 200 MPa does not change crystallinity, while at lower temperatures (< 1020 °C) melt fractions decrease significantly due to water-saturation triggering crystallisation. Furthermore, at temperatures > 1020 °C the upper limit of clinopyroxene stability is crossed upon decompression to 200 MPa inferring dissolution during near-adiabatic ascent. Liquid lines of descent of isothermal decompression paths are illustrated in Figs. 10b-d. CaO contents of residual melts exhibit a pronounced decrease over a narrow range in MgO upon isothermal decompression (Fig. 10b). In Al_2O_3 vs SiO_2 space, isotherms closely follow the compositional spread revealed by natural magmas, where the 1020 and 990 °C decompression paths best reproduce the Al_2O_3 contents of intermediate natural rocks (SiO_2 of 50 to 60 wt.%). In pseudoternary coordinates (Fig. 10d), isothermal decompression trajectories result in a distinct increase of normative clinopyroxene components, best visible at intermediate temperatures (1050–990 °C). Isothermal decompression, thus, exerts a strong control on alumina saturation with the consequence that decompressing arc magmas remain metaluminous and closely reproduce the compositional spread of natural calc-alkaline rocks.

In summary, isothermal decompression, representing an endmember process of crystallisation-driven differentiation, results in the formation of metaluminous intermediate magmas where the effect of pressure on phase equilibria (i.e. the destabilisation of clinopyroxene and stabilisation of plagioclase upon ascent) affects CaO and Al_2O_3 contents of residual liquids and, thus, alumina saturation. However, depending on the initial temperature, some low-pressure crystallisation is required after isothermal decompression to generate metaluminous liquids of intermediate composition. For example, at 1050 °C, around 30–40% of further crystallisation is necessary at 200 MPa to generate a liquid with SiO_2 contents > 60 wt.%. In contrast, at 1020 °C, residual melts are already of an intermediate composition (ca. 58 wt.% SiO_2) following isothermal decompression, thus limiting the extent of low-pressure cumulate formation. High temperature decompression trajectories may be traced by reworked cumulates, or mafic enclaves commonly found in intermediate plutonic rocks (e.g. Blundy and Sparks 1992). The volumetric proportions of mafic enclaves in such granitoids can extend up to several vol.% (e.g. Blundy and Sparks 1992) and, thus, account at least in parts for the amount of cumulates required to explain the low-pressure generation of intermediate and more evolved lithologies after isothermal decompression at higher temperatures. Nevertheless, the scarcity of significant proportions of mafic enclaves and mafic cumulates in exposed upper-crustal plutonic rocks favours isothermal decompression trajectories at lower temperatures (< 1050 °C).

The role of clinopyroxene dissolution during decompression

In the previous section we have shown that isothermal decompression represents a possible process to keep arc magmas metaluminous during polybaric differentiation. However, decompression-dominated polybaric fractionation trajectories (~ 20 °C/100 MPa) explored by Marxer et al. (2022) are insufficient to produce metaluminous residual liquids typically observed for many natural arc rocks. Therefore, it was proposed that processes such as magma mixing or incomplete fractionation (i.e. crystal entrainment upon magma ascent) are additionally involved. Arc basalts and basaltic andesites frequently carry crystals or crystal clots (e.g. Costa and Dungan 2005; Melekhova et al. 2015). Here we emphasise that the entrainment of early formed clinopyroxene-bearing cumulate lithologies in near-adiabatically rising residual liquids extracted from lower to mid-crustal levels could exert an important role on the chemistry of shallow crustal plutonic rocks. As illustrated in Fig. 10a, clinopyroxene crystals become unstable and start dissolving upon magma ascent due to the strong dependence of clinopyroxene stability on pressure. The decompression induced shift of the olivine-clinopyroxene cotectic results in a distinct increase of the normative Cpx-component (and decrease

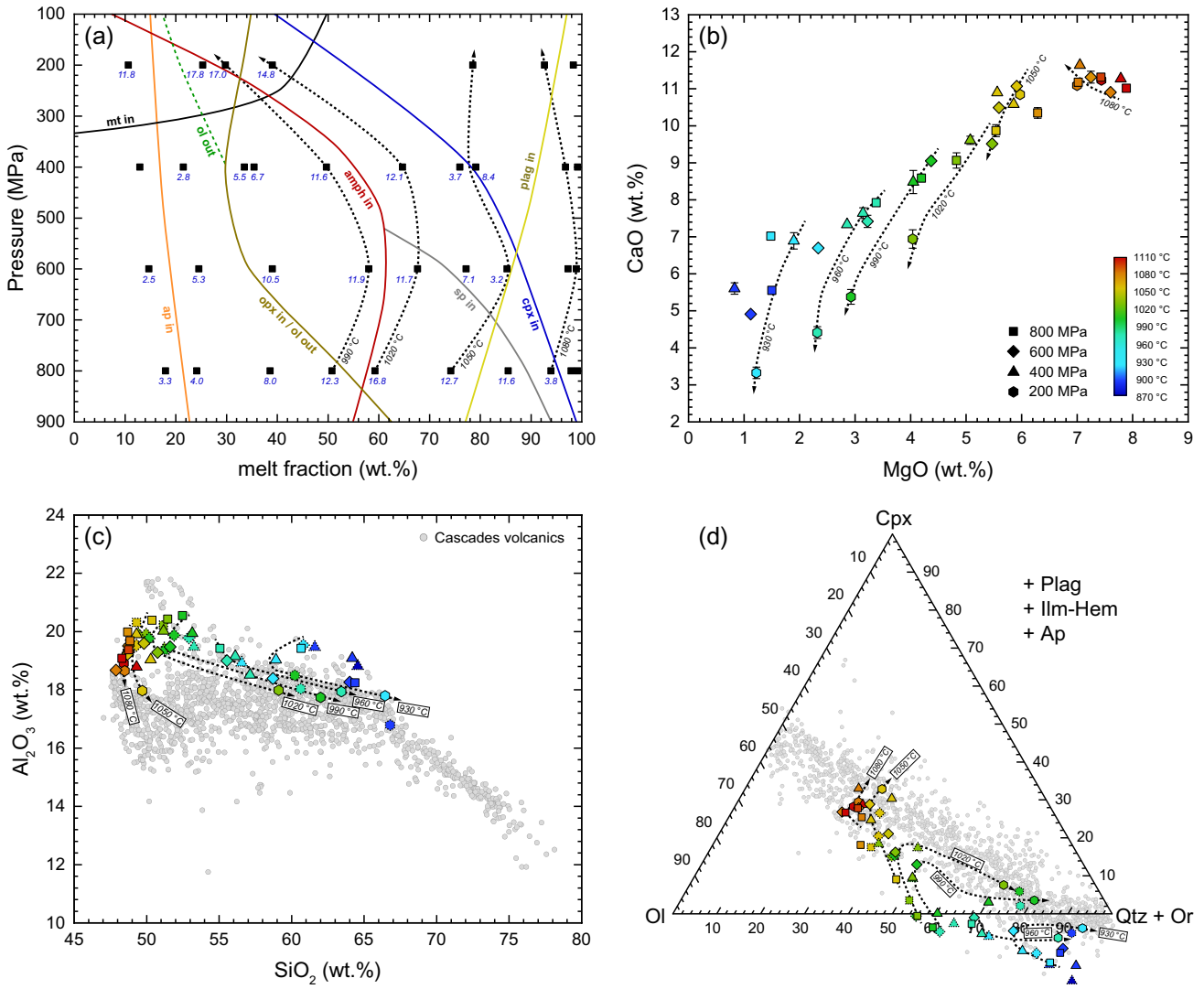

Fig. 10 Phase equilibria and differentiation trajectories during isothermal decompression of arc magmas. **a** Pressure (MPa) vs melt fraction (wt.%) phase diagram reconstructed from the equilibrium crystallisation experiments of this study. Mineral stability curves are drawn based on experimental phase assemblages. Black squares correspond to individual experiments and blue italic numbers next to symbols indicate the proportions of clinopyroxene crystallised (in wt.%). Stippled trends illustrate isothermal decompression paths. **b** CaO vs MgO (in wt.%) of residual liquids of the EC experiments with stippled arrows highlighting isothermal decompression trajectories. **c** Isothermal decompression paths in Al_2O_3 vs SiO_2 (wt.%) space based on EC and FC experiments in comparison with the natural calc-alkaline rock record (Cascades). **d** Isothermal decompression trajectories in the Ol-Cpx-Qtz + Or pseudoternary diagram based on isobaric EC and polybaric FC LLDs

of ASI) of the liquid phase. In contrast, other co-entrained phases, such as olivine and plagioclase remain stable (due to the expansion of their stability fields), and may serve as seeds for continuous crystallisation and fractionation, as long as ascent velocity exceeds gravitational settling. As shown by several previous experimental studies (e.g. Blatter et al. 2013; Nandedkar et al. 2014; Ulmer et al. 2018), high-temperature (ultra-)mafic cumulates formed at lower-crustal conditions via the crystallisation of primitive arc basalts contain significant amounts of clinopyroxene allowing substantial proportions of clinopyroxene entrainment during residual melt extraction.

The effect of clinopyroxene dissolution on residual melt compositions is illustrated in Fig. 11. Either 5 or 10 wt.% of experimental clinopyroxenes were added to the coexisting liquids for 400–800 MPa experiments at temperatures above 990 °C (i.e. melt fractions higher than 50 wt.%). According to the equilibrium crystallisation experiments (Fig. 10a) clinopyroxene proportions decrease by 5–10 wt.% upon isothermal decompression from 800 to 400 MPa inferring that dissolution of such amounts of clinopyroxene is consistent

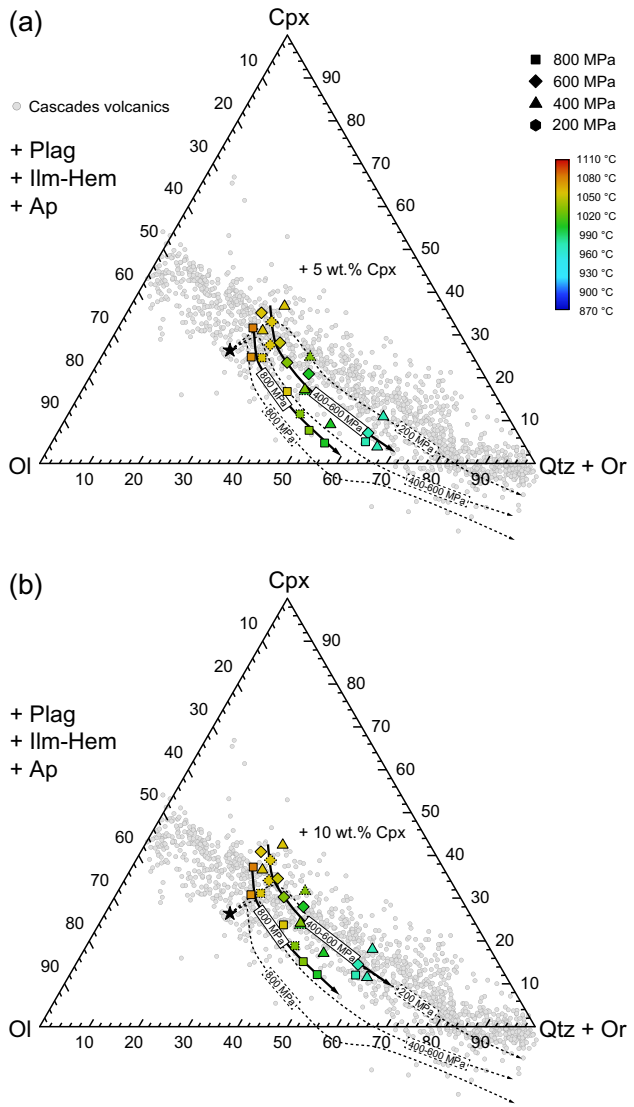

Fig. 11 Ol-Cpx-Qtz + Or pseudoternary diagram showing the effect of 5 (**a**) and 10 wt.% (**b**) of clinopyroxene dissolution on residual liquid compositions of the isobaric equilibrium (this study) and polybaric fractional crystallisation (Marxer et al. 2022) data (black solid trends) in comparison with the bulk rock compilations from the Cascades. Dotted trajectories illustrate the liquid lines of descent of isobaric equilibrium crystallisation (compare Fig. 8)

with phase equilibria constraints. Experiments at lower temperatures were not considered as (1) clinopyroxene is progressively replaced by amphibole at these conditions, (2) elevated crystallinities make efficent residual melt extraction together with crystal entrainment as phenocrysts less likely, and (3) lower temperatures strongly decrease clinopyroxene dissolution rates (Chen and Zhang 2009).

Remarkably, compositions of resultant liquids exhibit an almost perfect overlap with strongly metaluminous evolved basaltic and basaltic andesitic natural volcanic rocks from the Cascades. While this might be a coincidence, clinopyroxene entrainment and dissolution makes a compelling case for near-adiabatic decompression-controlled arc magma differentiation. We infer that minerals formed during high-pressure crystallisation of arc magmas (e.g. ol, cpx, ± plag) are physically rather easy to entrain in residual liquids as the viscous forces are sufficiently high to drag them along during magma ascent. Furthermore, entraining minor amounts of phenocrysts (e.g. 5–10 wt.%) is unlikely to significantly change the magma viscosity (< 10%) and density (< 4%), the main parameters controlling ascent velocity and magma rheology.

In addition, previous work has shown that the dissolution rate of clinopyroxene in basaltic magmas increases during magma ascent due to the decrease of clinopyroxene liquidus temperature with decreasing pressure (Brearley and Scarfe 1986; Zhang et al. 1989; Chen and Zhang 2009; Bonechi et al. 2021). Consequently, we speculate that dissolution of entrained clinopyroxene crystals is sufficiently fast during polybaric differentiation to allow for efficient re-equilibration with the coexisting liquid making clinopyroxene dissolution coupled with decompression-driven crystallisation an efficient mechanism for (i) keeping fractionating arc magmas metaluminous, and (ii) possibly generating significant amounts of intermediate residual liquids without requiring extensive fractionation at low pressures. It overcomes the high viscosity contrast issues of chemically different magmas (e.g. basaltic vs rhyolitic) for mixing (e.g. Hildreth and Moorbath 1988; Reubi and Blundy 2009; Reubi and Müntener 2022), and does not require the involvement of basaltic magmas with contrasting H_2O contents (Rezeau et al. 2021). However, additional research is required to refine this model for its applicability to natural arc systems.

Clinopyroxene dissolution during magma ascent has some crucial implications on the applicability of clinopyroxene geothermobarometers (e.g. Nimis 1995; Nimis and Ulmer 1998; Putirka 2008; Wang et al. 2021) to calc-alkaline rocks. The underlying assumption that the depths of magma reservoirs can be reconstructed using equilibrium compositions of clinopyroxene phenocrysts in natural volcanic rocks is highly dependent on the kinetics of clinopyroxene crystallisation and dissolution during ascent. A range of pressure estimates established via clinopyroxene-barometry could be the result of slow clinopyroxene dissolution rates and/or disequilibrium growth during ascent and does not a priori imply a polybaric differentiation scenario. In contrast, the absence of high-pressure clinopyroxene for a specific magmatic suite does not rule out lower-crustal differentiation processes, but may just be the result of complete clinopyroxene dissolution during ascent. Consequently, the kinetics of dissolution processes should be considered when interpreting results from clinopyroxene thermobarometry (Brearley and Scarfe 1986; Chen and Zhang 2009).

A general polybaric ascent-driven arc magma differentiation model

Phase equilibria characteristics identified in this study provide a basis for a generalised model on decompression-driven arc magma differentiation that is able to explain the predominantly metaluminous compositions of intermediate calc-alkaline rocks. Likely magma ascent trajectories are shown in Fig. 12 and discussed below. This phase diagram for fractional crystallisation of a near-primary high-Mg basalt was reconstructed from literature data (Alonso-Perez 2006; Nandedkar et al. 2014; Ulmer et al. 2018; Marxer et al. 2022), where low-pressure phase relations were complemented with the equilibrium crystallisation data of this study. Consequently, this diagram illustrates mineral saturation curves for a chemically-open magmatic system continuously evolving via fractional crystallisation.

We start with the premise that most mantle-derived primitive hydrous magmas reach the lower crust or crust-mantle boundary, where they start to crystallise (and differentiate) at lower crustal pressures thereby following high-pressure LLDs. After cooling to roughly 1050–1100 °C, residual liquids become buoyant due to increasing density contrasts with the surrounding cumulates ($\Delta\rho \sim 400$–600 kg/m^3) and start rising to mid-crustal levels (400–600 MPa). Decompressing magmas follow different trajectories including near-adiabatic polybaric differentiation accompanied by crystal entrainment (i.e. imperfect fractional crystallisation) and clinopyroxene dissolution (e.g. Fig. 10a). At mid-crustal levels, magma ascent likely is slowed down due to the combined effects of plagioclase crystallisation and the entering in a more felsic and, hence, less dense, crustal environment diminishing the density contrast between magma and wall-rock ($\Delta\rho \sim 200$–400 kg/m^3). Albeit speculative, cooling could be significant and metaluminous magmas will eventually reach compositions saturated with amphibole. Due to the strong compositional effect of amphibole crystallisation on the residual liquid (e.g. Fig. 5) and the concomitant decrease of melt density, the buoyancy of residual liquids re-increases and extracted melts experience near-adiabatic decompression to upper crustal levels (100–200 MPa) where eventual fluid saturation will promote final crystallisation towards silica-rich compositions and solidification to plutonic rocks. Such a model differentiation path (compare black arrow in Fig. 12) could account for (1) the predominant occurrence of cumulates in the lower and mid crust, (2) the (cryptic) amphibole fractionation signature identified for many arc magmas (e.g. Davidson et al. 2007), and (3) the predominance of metaluminous intermediate arc rocks. However, fractionated residual liquids could follow different trajectories, for example (i) decompression at high temperatures without passing through the amphibole stability field (as documented by melt inclusions (e.g. Reubi and Müntener 2022)) or (ii) just continue to fractionate and cool at high-pressures to temperatures of 950–1000 °C and only then experience near-adiabatic decompression towards upper crustal levels corresponding to natural rocks with a more-prominent peraluminous affinity. These alternative P–T evolution trends are illustrated with the stippled arrows in Fig. 12. These examples illustrate the potential consequences of arc magma ascent trajectories on the resultant liquid lines of descent. A natural consequence of such variable decompression paths are open system processes, such as mixing/mingling during ascent (Reubi and Müntener 2022) or mixing of highly evolved melt into replenishing magmas (e.g. Sakuyama 1981; Grove et al. 1982) explaining the wide compositional spread observed for natural arc rocks (Figs. 6–8).

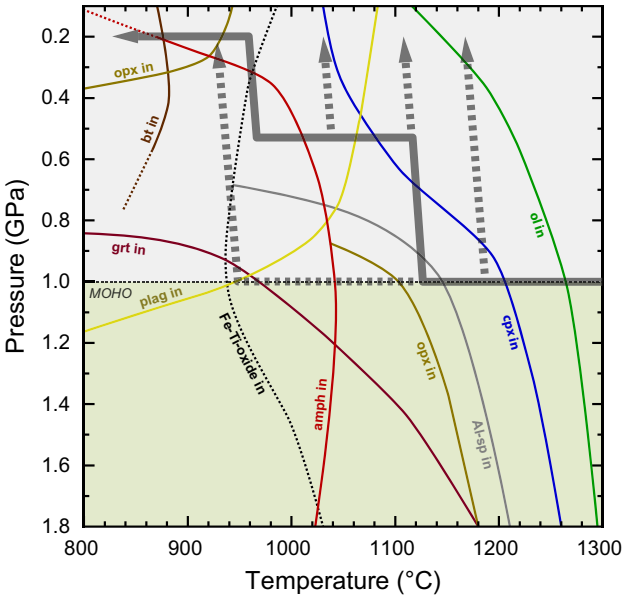

Fig. 12 P–T phase diagram for the fractional crystallisation of a hydrous primitive arc basalt reconstructed from literature data (Alonso-Perez 2006; Nandedkar et al. 2014; Ulmer et al. 2018; Marxer et al. 2022) illustrating a general polybaric decompression-driven arc magma differentiation model. Our postulated major P–T magma ascent trajectory is highlighted with the bold arrow while the stippled ones correspond to additional pathways resulting in the wide compositional variability observed for calc-alkaline rocks

Conclusions

In this study, the role of decompression on phase equilibria and arc magma differentiation trajectories was investigated conducting four isobaric experimental crystallisation series at 200, 400, 600, and 800 MPa on a high-alumina basalt. Combining the new data with the polybaric fractional crystallisation study of Marxer et al. (2022), the following conclusions can be drawn:

- The experiments demonstrate that phase equilibria of hydrous arc basalts is strongly affected by pressure. With decreasing pressure, the olivine stability field expands due to a shift of the olivine-out reaction curve towards lower temperatures. In addition, clinopyroxene saturation temperatures decrease with decreasing pressure, consistent with a shift of the olivine-clinopyroxene cotectic towards compositions with a higher normative clinopyroxene component. Plagioclase stability moderately increases with decreasing pressure, while amphibole exhibits a contrasting behaviour stabilising at slightly lower temperatures at low pressures, consistent with previous phase equilibria studies.
- Liquid lines of descent of the four equilibrium crystallisation series follow arc-tholeiitic (400–800 MPa) to calc-alkaline (200 MPa) differentiation trends and exhibit some distinct variability that can be related to the effects of pressure and oxygen fugacity on phase equilibria. This is mainly controlled by the relative stabilities of clinopyroxene, plagioclase, amphibole, and Fe-Ti oxides. In detail, the evolution of alumina saturation is strongly related to the effect of pressure on the position of the olivine-clinopyroxene cotectic curve and plagioclase saturation.
- A comparison of the presented data with the polybaric fractional crystallisation experiments of Marxer et al. (2022) reveals that crystal fractionation exerts a crucial control on crystallising mineral assemblages and proportions, mainly affecting amphibole and pyroxenes. Distinctly lower proportions of amphibole were identified for the polybaric fractionation experiments. This observation is related to the suppression of peritectic mineral reactions during crystal fractionation and the concomitant change in magma bulk composition. Coexistence of amphibole and pyroxenes could only be observed for the equilibrium crystallisation series. However, resultant liquid lines of descent of the equilibrium and fractional crystallisation series are similar. This indicates that crystal fractionation only exerts a minor control on the major element evolution trends of arc magmas. In contrast, cumulate lines of descent of equilibrium and fractional crystallisation differ significantly, where cumulates from fractional crystallisation exhibit a much larger chemical variability.
- The experiments indicate that isothermal decompression of evolved basaltic magmas from the lower to upper crust (representing a close approximation of near-adiabatic magma ascent) does not significantly change crystallinity. However, changes in phase equilibria during decompression, such as destabilisation of clinopyroxene and crystallisation of plagioclase, keep residual liquids metaluminous, as observed for most natural arc magma compositions. Isothermal/near-adiabatic decompression, therefore, represents an important process for arc magma differentiation.
- Entrainment of clinopyroxene-bearing mineral assemblages during residual melt extraction from the lower crust (i.e. imperfect fractional crystallisation) and subsequent clinopyroxene dissolution during near-adiabatic decompression further promotes the formation of metaluminous intermediate melt compositions. Decompression, thus, represents an attractive and efficient mechanism for crystallisation-driven arc magma differentiation. Simple calculations revealed that 5–10 wt.% of clinopyroxene dissolution are sufficient to keep residual experimental liquids close to the natural rock record.
- Depending on the thermal and compositional structure of arc crust, different combinations of near-isobaric cooling, near-adiabatic ascent, phenocryst entrainment and clinopyroxene dissolution, and/or plagioclase fractionation, combined with mingling and mixing keeps residual liquids mostly at metaluminous compositions. The observed compositional spread of natural calc-alkaline rocks can ultimately be viewed as a consequence of phase equilibria control at all crustal levels.

Supplementary Information The online version contains supplementary material available at https://doi.org/10.1007/s00410-023-02035-7.

Acknowledgements We thank Lukas Martin, Eric Reusser, and Julien Allaz for assistance during SEM-EDS and EPMA analyses and Andy Huber, Andreas Jallas, Thomas Good, Uli Kroll, Andreas Reimer, and Julian Feige for technical support in the experimental labs and thorough sample preparation. Thomas van Gerve and Olivier Namur are gratefully acknowledged for assistance during Raman measurements at KU Leuven. We are grateful to Tom Sisson, Manuel Pimenta Silva, François Holtz, Olivier Bachmann, and Max Schmidt for discussions. Thoughtful and constructive reviews from Madeleine Humphreys and Dawnika L. Blatter as well as the efficient editorial handling by Dante Canil are gratefully acknowledged. This work was supported by the ETH research grant ETH-14 16-1 and the DFG project HO1337/47 (part of the Forschungsgruppe FOR 2881 "Diffusion chronometry of magmatic systems") covering F.M.

Funding Open Access funding enabled and organized by Projekt DEAL. This work was supported by the ETH research grant ETH-14 16–1 and the DFG project HO1337/47 covering F.M.

Availability of data and material Data established in the scope of this project are available as electronic supplementary material to this manuscript.

Code availability Not applicable.

Declarations

Conflict of interest We declare no conflicts of interests.

References

Almeev RR, Holtz F, Koepke J, Parat F (2012) Experimental calibration of the effect of H_2O on plagioclase crystallization in basaltic melt at 200 MPa. Am Miner 97:1234–1240. https://doi.org/10.2138/am.2012.4100

Alonso-Perez R, Müntener O, Ulmer P (2009) Igneous garnet and amphibole fractionation in the roots of island arcs: experimental constraints on andesitic liquids. Contrib Miner Petrol 157:541–558. https://doi.org/10.1007/s00410-008-0351-8

Alonso-Perez R (2006) The role of garnet in the evolution of hydrous, calc-alkaline magmas: an experimental study at 0.8–1.5 GPa. Zürich: Doctoral Thesis, ETH Zürich

Anderson AT (1973) The before-eruption water content of some high-alumina magmas. Bulletin Volcanologique 37:530–552. https://doi.org/10.1007/BF02596890

Bard JP (1983) Metamorphism of an obducted island arc: example of the Kohistan sequence (Pakistan) in the Himalayan collided range. Earth Planet Sci Lett 65:133–144. https://doi.org/10.1016/0012-821x(83)90195-4

Barr JA, Grove TL (2010) AuPdFe ternary solution model and applications to understanding the fO_2 of hydrous, high-pressure experiments. Contrib Miner Petrol 160:631–643. https://doi.org/10.1007/s00410-010-0497-z

Berndt J, Liebske C, Holtz F, Freise M, Nowak M, Ziegenbein D, Hurkuck W, Koepke J (2002) A combined rapid-quench and H_2-membrane setup for internally heated pressure vessels: description and application for water solubility in basaltic melts. Am Miner 87:1717–1726. https://doi.org/10.2138/am-2002-11-1222

Bianchi A, Callegari E, Jobstraibizer PG (1970) I tipi fondamentali petrogenetici del Plutone dell'Adamello. Tonaliti-quarzodioriti-granodioriti e loro varietà leucocratiche. Mem Ist Geol Mineral Univ Padova 27:1–148

Blatter DL, Sisson TW, Hankins WB (2013) Crystallization of oxidized, moderately hydrous arc basalt at mid- to lower-crustal pressures: implications for andesite genesis. Contrib Miner Petrol 166:861–886. https://doi.org/10.1007/s00410-013-0920-3

Blatter DL, Sisson TW, Hankins WB (2017) Voluminous arc dacites as amphibole reaction-boundary liquids. Contrib Miner Petrol 172:27. https://doi.org/10.1007/s00410-017-1340-6

Blundy J, Cashman K (2008) Petrologic reconstruction of magmatic system variables and processes. Rev Miner Geochem 69:179–239. https://doi.org/10.2138/rmg.2008.69.6

Blundy JD, Sparks RSJ (1992) Petrogenesis of mafic inclusions in granitoids of the Adamello Massif, Italy. J Petrol 33:1039–1104. https://doi.org/10.1093/petrology/33.5.1039

Blundy J, Cashman K, Humphreys M (2006) Magma heating by decompression-driven crystallization beneath andesite volcanoes. Nature 443:76–80. https://doi.org/10.1038/nature05100

Blundy J, Melekhova E, Ziberna L, Humphreys MCS, Cerantolo V, Brooker RA, McCammon C, Pichavant M, Ulmer P (2020) Effect of redox on Fe-Mg-Mn exchange between olivine and melt and an oxybarometer for basalts. Contrib Miner Petrol 175:103. https://doi.org/10.1007/s00410-020-01736-7

Bonechi B, Perinelli C, Gaeta M, Stagno V, Fabbrizio A, Mollo S, Hrubiak R (2021) High pressure experimental investigation of clinopyroxene dissolution in a K-basaltic melt. Chem Geol. https://doi.org/10.1016/j.chemgeo.2021.120533

Bowen NL (1928) The evoution of the igneous rocks. Princton University Press, Princton

Brearley M, Scarfe CM (1986) Dissolution rates of upper mantle minerals in an alkali basalt melt at high pressure: an experimental study and implications for ultramafic xenolith survival. J Petrol 27:1157–1182. https://doi.org/10.1093/petrology/27.5.1157

Bucholz CE, Kelemen PB (2019) Oxygen fugacity at the base of the Talkeetna arc, Alaska. Contrib Mineral Petrol 174:79. https://doi.org/10.1007/s00410-019-1609-z

Burnham CW (1994) Development of the Burnham model for prediction of H_2O solubility in magmas. Rev Miner Geochem 30:123–130. https://doi.org/10.1515/9781501509674-009

Burnham CW, Davis NF (1974) The role of H_2O in silicate melts: II. Thermodynamic and phase relations in the system $NaAlSi_3O_8$-H_2O to 10 kilobars, 700 °C to 1100 °C. Am J Sci 274:902–940. https://doi.org/10.2475/ajs.274.8.902

Carmichael ISE (1991) The redox states of basic and silicic magmas: a reflection of their source regions? Contrib Miner Petrol 106:129–141. https://doi.org/10.1007/BF00306429

Carmichael ISE (2002) The andesite aqueduct: perspectives on the evolution of intermediate magmatism in west-central (105–99°W) Mexico. Contrib Miner Petrol 143:641–663. https://doi.org/10.1007/s00410-002-0370-9

Chen Y, Zhang YX (2009) Clinopyroxene dissolution in basaltic melt. Geochim Cosmochim Acta 73:5730–5747. https://doi.org/10.1016/j.gca.2009.06.016

Costa F, Dungan M (2005) Short time scales of magmatic assimilation from diffusion modeling of multiple elements in olivine. Geology 33:837–840. https://doi.org/10.1130/G21675.1

Cottrell E, Birner SK, Brounce M, Davis FA, Waters LE, Kelley KA (2021) Oxygen fugacity across tectonic settings. In: Moretti R, Neuville DR (eds) Magma redox geochemistry, pp 33–61. https://doi.org/10.1002/9781119473206.ch3

Davidson J, Turner S, Handley H, Macpherson C, Dosseto A (2007) Amphibole "sponge" in arc crust? Geology 35:787–790. https://doi.org/10.1130/g23637a.1

Del Moro A, Ferrara G, Tonarini S, Callegari E (1983) Rb-Sr systematics on rocks from the Adamello batholith (Southern Alps). Memoria Della Società Geologica Italiana 26:261–284

Dessimoz M, Müntener O, Ulmer P (2012) A case for hornblende dominated fractionation of arc magmas: the Chelan Complex (Washington Cascades). Contrib Miner Petrol 163:567–589. https://doi.org/10.1007/s00410-011-0685-5

Ducea MN, Otamendi JE, Bergantz GW, Jianu D, Petrescu L (2015) The origin and petrologic evolution of the Ordovician Famatinian-Puna arc. Geodyn Cordilleran Orogenic Syst Central Andes Argent Northern Chile 212:125–138. https://doi.org/10.1130/2015.1212(07)

Erdmann M, Koepke J (2016) Experimental temperature cycling as a powerful tool to enlarge melt pools and crystals at magma storage conditions. Am Miner 101:960–969. https://doi.org/10.2138/am-2016-5398

Feig ST, Koepke J, Snow JE (2010) Effect of oxygen fugacity and water on phase equilibria of a hydrous tholeiitic basalt. Contrib Miner Petrol 160:551–568. https://doi.org/10.1007/s00410-010-0493-3

van Gerve T, Namur O (2023) SilicH_2O: a graphical user interface for processing silicate glass Raman spectra and quantifying H_2O. EarthArXiv. https://doi.org/10.31223/X5XH33

Glazner AF (2019) The ascent of water-rich magma and decompression heating: a thermodynamic analysis. Am Miner 104:890–896. https://doi.org/10.2138/am-2019-6925

Goltz AE, Krawczynski MJ, Gavrilenko M, Gorbach NV, Ruprecht P (2020) Evidence for superhydrous primitive arc magmas from mafic enclaves at Shiveluch volcano Kamchatka. Contrib Mineral Petrol. https://doi.org/10.1007/s00410-020-01746-5

Greene AR, DeBari SM, Kelemen PB, Blusztajn J, Clift PD (2006) A detailed geochemical study of island arc crust: the Talkeetna Arc Section, South-Central Alaska. J Petrol 47:1051–1093. https://doi.org/10.1093/petrology/egl002

Grove TL, Baker MB (1984) Phase-equilibrium controls on the tholeiitic versus calc-alkaline differentiation trends. J Geophys Res 89:3253–3274. https://doi.org/10.1029/JB089iB05p03253

Grove TL, Gerlach DC, Sando TW (1982) Origin of calc-alkaline series lavas at Medicine Lake Volcano by fractionation, assimilation and mixing. Contrib Miner Petrol 80:160–182. https://doi.org/10.1007/Bf00374893

Grove TL, Kinzler RJ, Bryan WB (1992) Fractionation of mid-ocean ridge basalt (MORB). Geophys Monogr Ser 71:281–310. https://doi.org/10.1029/GM071p0281

Hamada M, Fujii T (2008) Experimental constraints on the effects of pressure and H_2O on the fractional crystallization of high-Mg island arc basalt. Contrib Miner Petrol 155:767–790. https://doi.org/10.1007/s00410-007-0269-6

Hernlund J, Leinenweber K, Locke D, Tyburczy JA (2006) A numerical model for steady-state temperature distributions in solid-medium high-pressure cell assemblies. Am Miner 91:295–305. https://doi.org/10.2138/am.2006.1938

Hildreth W, Moorbath S (1988) Crustal contributions to arc magmatism in the Andes of Central Chile. Contrib Miner Petrol 98:455–489. https://doi.org/10.1007/Bf00372365

Holland T, Blundy J (1994) Non-ideal interactions in calcic amphiboles and their bearing on amphibole-plagioclase thermometry. Contrib Miner Petrol 116:433–447. https://doi.org/10.1007/BF00310910

Hughes EC, Buse B, Kearns SL, Blundy JD, Kilgour G, Mader HM (2019) Low analytical totals in EPMA of hydrous silicate glass due to sub-surface charging: Obtaining accurate volatiles by difference. Chem Geol 505:48–56. https://doi.org/10.1016/j.chemgeo.2018.11.015

Hurlimann N, Müntener O, Ulmer P, Nandedkar R, Chiaradia M, Ovtcharova M (2016) Primary magmas in continental arcs and their differentiated products: Petrology of a post-plutonic dyke suite in the Tertiary Adamello Batholith (Alps). J Petrol 57:495–533. https://doi.org/10.1093/petrology/egw016

Jagoutz O (2014) Arc crustal differentiation mechanisms. Earth Planet Sci Lett 396:267–277. https://doi.org/10.1016/j.epsl.2014.03.060

Kaegi R, Muentener O, Ulmer P, Ottolini L (2005) Piston-cylinder experiments on H_2O undersaturated Fe-bearing systems: An experimental setup approaching fO_2 conditions of natural calc-alkaline magmas. Am Miner 90:708–717. https://doi.org/10.2138/am.2005.1663

Kawamoto T (1996) Experimental constraints on differentiation and H_2O abundance of calc-alkaline magmas. Earth Planet Sci Lett 144:577–589. https://doi.org/10.1016/S0012-821x(96)00182-3

Knipping JL, Webster JD, Simon AC, Holtz F (2019) Accumulation of magnetite by flotation on bubbles during decompression of silicate magma. Sci Rep. https://doi.org/10.1038/s41598-019-40376-1

Lange RA, Carmichael ISE (1987) Densities of Na_2O-K_2O-CaO-MgO-FeO-Fe_2O_3-Al_2O_3-TiO_2-SiO_2 liquids: New measurements and derived partial molar properties. Geochim Cosmochim Acta 51:2931–2946. https://doi.org/10.1016/0016-7037(87)90368-1

Larocque J, Canil D (2010) The role of amphibole in the evolution of arc magmas and crust: the case from the Jurassic Bonanza arc section, Vancouver Island, Canada. Contrib Miner Petrol 159:475–492. https://doi.org/10.1007/s00410-009-0436-z

Laumonier M, Scaillet B, Pichavant M, Champallier R, Andujar J, Arbaret L (2014) On the conditions of magma mixing and its bearing on andesite production in the crust. Nat Commun. https://doi.org/10.1038/ncomms6607

Le Bas MJ, Le Maitre RW, Streckeisen A, Zanettin B (1986) A chemical classification of volcanic rocks vased on the total alkali-silica diagram. J Petrol 27:745–750. https://doi.org/10.1093/petrology/27.3.745

Le Losq C, Neuville DR, Moretti R, Roux J (2012) Amorphous materials: Determination of water content in silicate glasses using Raman spectrometry: Implications for the study of explosive volcanism. Am Miner 97:779–790. https://doi.org/10.2138/am.2012.3831

Lewis MJ, Bucholz CE, Jagoutz OE (2021) Evidence for polybaric fractional crystallization in a continental arc: hidden Lakes mafic complex, Sierra Nevada batholith, California. Contrib Mineral Petrol. https://doi.org/10.1007/s00410-021-01844-y

Macera P, Ferrara G, Pescia A, Callegari E (1983) A geochemical study on the acid and basic rocks of the Adamello Batholith. Memoria Della Società Geologica Italiana 26:223–259

Macpherson CG, Dreher ST, Thirlwall MF (2006) Adakites without slab melting: High pressure differentiation of island arc magma, Mindanao, the Philippines. Earth Planet Sci Lett 243:581–593. https://doi.org/10.1016/j.epsl.2005.12.034

Marxer F, Ulmer P (2019) Crystallisation and zircon saturation of calc-alkaline tonalite from the Adamello Batholith at upper crustal conditions: an experimental study. Contrib Miner Petrol 174:84. https://doi.org/10.1007/s00410-019-1619-x

Marxer F, Ulmer P, Müntener O (2022) Polybaric fractional crystallisation of arc magmas: an experimental study simulating transcrustal magmatic systems. Contrib Mineral Petrol 177:3. https://doi.org/10.1007/s00410-021-01856-8

Mastin LG, Ghiorso MS (2001) Adiabatic temperature changes of magma-gas mixtures during ascent and eruption. Contrib Miner Petrol 141:307–321. https://doi.org/10.1007/s004100000210

Matjuschkin V, Brooker RA, Tattitch B, Blundy JD, Stamper CC (2015) Control and monitoring of oxygen fugacity in piston cylinder experiments. Contrib Miner Petrol 169:9. https://doi.org/10.1007/s00410-015-1105-z

Melekhova E, Blundy J, Robertson R, Humphreys MCS (2015) Experimental evidence for polybaric differentiation of primitive arc basalt beneath St. Vincent, Lesser Antilles. J Petrol 56:161–192. https://doi.org/10.1093/petrology/egu074

Mills RD, Glazner AF (2013) Experimental study on the effects of temperature cycling on coarsening of plagioclase and olivine in an alkali basalt. Contrib Miner Petrol 166:97–111. https://doi.org/10.1007/s00410-013-0867-4

Miyashiro A (1974) Volcanic rock series in island arcs and active continental margins. Am J Sci 274:321–355. https://doi.org/10.2475/ajs.274.4.321

Müntener O, Ulmer P (2018) Arc crust formation and differentiation constrained by experimental petrology. Am J Sci 318:64–89. https://doi.org/10.2475/01.2018.04

Müntener O, Kelemen PB, Grove TL (2001) The role of H_2O during crystallization of primitive arc magmas under uppermost mantle conditions and genesis of igneous pyroxenites: an experimental study. Contrib Miner Petrol 141:643–658. https://doi.org/10.1007/s004100100266

Müntener O, Ulmer P, Blundy JD (2021) Superhydrous arc magmas in the alpine context. Elements 17:35–40. https://doi.org/10.2138/gselements.17.1.35

Nandedkar RH, Ulmer P, Müntener O (2014) Fractional crystallization of primitive, hydrous arc magmas: an experimental study at 0.7 GPa. Contrib Mineral Petrol 167:1015. https://doi.org/10.1007/s00410-014-1015-5

Nimis P (1995) A clinopyroxene geobarometer for basaltic systems based on crystal-structure modeling. Contrib Miner Petrol 121:115–125. https://doi.org/10.1007/s004100050093

Nimis P, Ulmer P (1998) Clinopyroxene geobarometry of magmatic rocks Part 1: An expanded structural geobarometer for anhydrous and hydrous, basic and ultrabasic systems. Contrib Miner Petrol 133:122–135. https://doi.org/10.1007/s004100050442

Putirka KD (2008) Thermometers and barometers for volcanic systems. Rev Miner Geochem 69:61–120. https://doi.org/10.2138/rmg.2008.69.3

Rapela CW, Pankhurst RJ, Casquet C, Dahlquist JA, Fanning CM, Baldo EG, Galindo C, Alasino PH, Ramacciotti CD, Verdecchia SO, Murra JA, Basei MAS (2018) A review of the Famatinian Ordovician magmatism in southern South America: evidence of lithosphere reworking and continental subduction in the early proto-Andean margin of Gondwana. Earth Sci Rev 187:259–285. https://doi.org/10.1016/j.earscirev.2018.10.006

Reubi O, Blundy J (2009) A dearth of intermediate melts at subduction zone volcanoes and the petrogenesis of arc andesites. Nature 461:1269–1273. https://doi.org/10.1038/nature08510

Reubi O, Müntener O (2022) Making andesites and the continental crust: Mind the step when wet. J Petrol. https://doi.org/10.1093/petrology/egac044

Rezeau H, Klein BZ, Jagoutz O (2021) Mixing dry and wet magmas in the lower crust of a continental arc: new petrological insights from the Bear Valley Intrusive Suite, southern Sierra Nevada, California. Contrib Mineral Petrol. https://doi.org/10.1007/s00410-021-01832-2

Romick JD, Kay SM, Kay RW (1992) The Influence of amphibole fractionation on the evolution of calc-alkaline andesite and cacite tephra from the Central Aleutians, Alaska. Contrib Miner Petrol 112:101–118. https://doi.org/10.1007/Bf00310958

Sakuyama M (1981) Petrological study of the Myoko and Kurohime Volcanos, Japan—crystallization sequence and evidence for magma mixing. J Petrol 22:553–583. https://doi.org/10.1093/petrology/22.4.553

Sisson TW, Grove TL (1993) Experimental investigations of the role of H_2O in calc-alkaline differentiation and subduction zone magmatism. Contrib Miner Petrol 113:143–166. https://doi.org/10.1007/BF00283225

Sisson TW, Ratajeski K, Hankins WB, Glazner AF (2005) Voluminous granitic magmas from common basaltic sources. Contrib Miner Petrol 148:635–661. https://doi.org/10.1007/s00410-004-0632-9

Sparks RSJ, Marshall LA (1986) Thermal and mechanical constraints on mixing between mafic and silicic magmas. J Volcanol Geoth Res 29:99–124. https://doi.org/10.1016/0377-0273(86)90041-7

Stamper CC, Melekhova E, Blundy JD, Arculus RJ, Humphreys MCS, Brooker RA (2014) Oxidised phase relations of a primitive basalt from Grenada, Lesser Antilles. Contrib Miner Petrol 167:954. https://doi.org/10.1007/s00410-013-0954-6

Turner SJ, Langmuir CH (2015) The global chemical systematics of arc front stratovolcanoes: evaluating the role of crustal processes. Earth Planet Sci Lett 422:182–193. https://doi.org/10.1016/j.epsl.2015.03.056

Ulmer P, Callegari E, Sonderegger U (1983) Genesis of the mafic and ultramafic rocks and their genetical relations to the tonalitic-trondhjemitic granitoids of the southern part of the Adamello batholith (Northern Italy). Memorie Della Società Geologica Italiana 26:171–222

Ulmer P, Kaegi R, Müntener O (2018) Experimentally derived intermediate to silica-rich arc magmas by fractional and equilibrium crystallization at 1.0 GPa: An evaluation of phase relationships, compositions, liquid lines of descent and oxygen fugacity. J Petrol 59:11–58. https://doi.org/10.1093/petrology/egy017

Urann BM, Le Roux V, Jagoutz O, Müntener O, Behn MD, Chin EJ (2022) High water content of arc magmas recorded in cumulates from subduction zone lower crust. Nat Geosci 15:501. https://doi.org/10.1038/s41561-022-00947-w

Verberne R (2013) The role of magma rheology during emplacement of the Listino Suite, Adamello Massif, Italy. Lausanne: Doctoral Thesis, University of Lausanne

Vigneresse JL, Barbey P, Cuney M (1996) Rheological transitions during partial melting and crystallization with application to felsic magma segregation and transfer. J Petrol 37:1579–1600. https://doi.org/10.1093/petrology/37.6.1579

Villiger S, Ulmer P, Müntener O, Thompson AB (2004) The liquid line of descent of anhydrous, mantle-derived, tholeiitic liquids by fractional and equilibrium crystallization—an experimental study at 1.0 GPa. J Petrol 45:2369–2388. https://doi.org/10.1093/petrology/egh042

Walker BA, Bergantz GW, Otamendi JE, Ducea MN, Cristofolini EA (2015) A MASH zone revealed: the mafic complex of the Sierra Valle Fertil. J Petrol 56:1863–1896. https://doi.org/10.1093/petrology/egv057

Wang X, Hou T, Wang M, Zhang C, Zhang Z, Pan R, Marxer F, Zhang H (2021) A new clinopyroxene thermobarometer for mafic to intermediate magmatic systems. Eur J Mineral 33:621–637. https://doi.org/10.5194/ejm-33-621-2021

Waters LE, Lange RA (2015) An updated calibration of the plagioclase-liquid hygrometer-thermometer applicable to basalts through rhyolites. Am Miner 100:2172–2184. https://doi.org/10.2138/am-2015-5232

Zhang Y, Walker D, Lesher CE (1989) Diffusive crystal dissolution. Contrib Miner Petrol 102:492–513. https://doi.org/10.1007/BF00371090